



NTNU – Trondheim
Norwegian University of
Science and Technology

Numerical Investigation of 3D Flow Around Two Tandem Cylinders

Ragnhild Birgitte Hidle
Kalvig

Marine Technology

Submission date: June 2015

Supervisor: Bjørnar Pettersen, IMT

Co-supervisor: Mia Prsic, IMT

Norwegian University of Science and Technology
Department of Marine Technology



MASTER THESIS IN MARINE HYDRODYNAMICS

SPRING 2015

FOR

Stud.techn. Ragnhild H. Kalvig

NUMERICAL INVESTIGATION OF 3D FLOW AROUND TWO TANDEM CYLINDERS

(Numerisk undersøkelse av strømning omkring to tandem sylindere.)

The candidate shall investigate the three-dimensional wake flow behind two circular cylinders in a tandem configuration in infinite fluid. Numerical simulation tool to be used is OpenFOAM at moderate Reynolds number ($Re=13100$) with proper turbulence modeling. Focus of the study shall be on the physical flow field details, especially in the flow zone between the two cylinders.

If time permit, different boundary conditions shall be investigated (i.e. fixed wall(s) close to the cylinders), and results compared.

In the thesis the candidate shall present her personal contribution to the resolution of the problem within the scope of the thesis work. Theories and conclusions should be based on mathematical derivation and logic reasoning identifying the various steps in the deduction. The original contribution of the candidate and material taken from other sources shall be clearly defined. Work from other sources shall be properly referenced. The candidate should utilize the existing possibilities for obtaining relevant literature.

The thesis should be organized in a rational manner to give a clear exposition of results, assessments and conclusions. The text should be brief and to the point, with a clear language.

The thesis shall contain the following elements: A text defining the scope, preface, list of contents, summary, main body of thesis, conclusions with recommendations for further work, list of symbols and acronyms, references and appendices. All figures, tables and equations shall be numerated.

It is supposed that Department of Marine Technology, NTNU, can use the results freely in its research work by referring to the student's thesis.

The thesis shall be submitted June 10, 2015, in two copies.

Bjørnar Pettersen
Professor/supervisor

Co-supervisor: PhD-student Mia Abrahamsen-Prsic

Abstract

Circular cylinders in tandem arrangement are used in many marine applications like dual pipelines and dual risers. Turbulent flow in 3D around two tandem cylinders is simulated numerically using Large Eddy Simulation (LES) with a Smagorinsky subgrid scale model. The Reynolds number based on the cylinder diameter of 1 meter and free stream velocity of $U = 1.31$ m/s is 13100, which is in the subcritical flow regime. The center-to-center spacing between the cylinders is $S/D = 5$. The software used for the numerical simulation is the open source code OpenFOAM.

The physics of the flow around the cylinders has been investigated by studying velocity- and pressure fields, especially in the gap region between the two cylinders. The results are presented as following: Vorticity distribution in the gap showing vortex formation and impingement onto the downstream cylinder. Velocity distributions in the wake and gap showing wake flow. Mean and Root Mean Square (RMS) pressure distributions over the cylinder surfaces. Drag- and lift coefficients for the two cylinders. Strouhal number at different locations in the domain and surface streamlines showing separation.

The flow picture for this spacing and Reynolds number proved to be jump flow, where vortices are formed and shed behind the upstream cylinder, travel over the gap and impinge the downstream cylinder. This causes large pressure fluctuations and forces on the downstream cylinder. This was reflected in the pressure distributions and force coefficients. The Strouhal number was the same behind both cylinders which indicates synchronized shedding of vortices. The downstream cylinder sees a chaotic inflow due to vortices shed from upstream cylinder. This was reflected in the velocity streamlines. There was indications that the results for the downstream cylinder did not converge for the simulation duration in this work. In general the LES turbulence model gave good results that were in agreement with previous work.

Sammendrag

Sirkulære sylindere arrangert i tandem er mye brukt i den marine offshore industrien, for eksempel doble rørledninger eller doble stigerør. Turbulent strømning i 3D rundt to tandem sylindere har blitt numerisk modellert ved bruk av Large Eddy Simulation (LES) med en Smagorinsky subgrid skala modell. Reynoldsnummeret var 13100 basert på sylinderdiameteren på 1 meter og fristrømhastigheten på $U = 1.31$ m/s. Dette er i det subkritiske strømningsregimet. Avstanden mellom sylindrene, senter-til-senter er $S/D = 5$. Programvaren som er brukt til simuleringene er open source koden OpenFOAM.

Fysikken av strømmingen rundt sylindrene har blitt undersøkt ved å studere hastighets- og trykkfelt, spesielt i regionen mellom sylindrene. Resultatene er presentert på følgende måte: virvling i gapet mellom sylindrene som viser virvelformasjon og -kollisjon med nedstrømsylinder. Hastighetsprofiler i kjølevannet av sylindrene som viser strømning i kjølevannet. Gjennomsnittelig og fluktuerende trykkfordeling over sylinderoverflatene. Drag- og løftkoeffisienter for de to sylindrene. Strouhaltall i forskjellige posisjoner i domenet og strømningslinjer på overflaten av sylindrene som viser separasjon.

Strømningsbildet for denne avstanden mellom sylindrene og Reynoldsnummer viste seg å være 'jump flow', hvor virvler formes og avløses bak oppstrømsylinderen, transporteres over mellomrommet og kræsjer i nedstrømsylinderen. Dette fører til store trykkfluktueringer og krefter på nedstrømsylinderen. Dette ble reflektert i trykkfordelingen og kraftkoeffisientene. Strouhaltallet var likt bak begge sylindrene, noe som indikerer synkronisert virvelavløsning. Nedstrømsylinderen har en kaotisk instrømning på grunn av virvelavløsningen fra oppstrømsylinder. Dette var reflektert i strømningslinjene for hastighet. Det var indikasjoner på at resultatene for nedstrømsylinderen ikke var konverget for simuleringsvarigheten i dette arbeidet. Generelt ga LES tubulensmodellen gode resultater som var i samsvar med tidligere arbeid.

Preface

This thesis is a result of my final semester of my Master's degree in Marine Technology. It is written at the Institute of Marine Technology at the Norwegian University of Science and Technology in the spring of 2015. The thesis describes the work done with a 3D numerical simulation in OpenFOAM of tandem cylinders in the subcritical flow regime.

The topic of the thesis was inspired by my supervisor Bjørnar Pettersen who organized a cooperation with PhD-student Mia Abrahamsen-Prsic. This made the work very motivating. Ever since the autumn of 2014 Bjørnar Pettersen has inspired my interest for Computational Fluid Dynamics (CFD). In coherence with the interest I already had for marine risers and other subsea constructions, this has been the basis for a very large learning output on my part.

Given that I had never worked with CFD prior to this final year of studying, I have realized that it is an amazing tool with many possibilities and prospects for the future. The learning curve has been steep ever since the project work in the fall semester and up to the final phase of my Master's degree. In this thesis the focus has been on pre- and post processing and understanding the data outputs from the simulations, and of course to get a feeling of the complexity of the flow around tandem cylinders.

I would like to give a big thank you to the following persons for their great help on my work with this thesis. Without them, I would not be able to deliver this result.

Firstly, I would like to thank my supervisor, professor Bjørnar Pettersen. He has been very motivating and helpful during the work with this Thesis. His own dedication and passion for the topic has been very inspirational.

Next I would like to thank my co-supervisor Mia Abrahamsen-Prsic for all her help regarding questions I have had about the work. Her expertise in the field and her previous experience with similar cases have been a very good guidance for me.

I would also like to thank PhD-student Håkon Strandenes. He has been a great help regarding all questions I have had about OpenFOAM and the post processing tool ParaFoam.

Lastly, I would like to thank the HPC group at NTNU for the possibility to use the super-computer Vilje. Without this opportunity, this work would not be possible.

Ragnhild Kalvig
Trondheim, June 6. 2015

Contents

1	Introduction	1
1.1	State of the art	1
1.2	Motivation	4
1.3	Structure of the Thesis	5
2	Background theory	7
2.1	Flow around one circular cylinder	7
2.1.1	Boundary layer	8
2.1.2	Flow separation	9
2.1.3	Modeling the fluid motions correctly - Navier Stokes equations	15
2.2	Flow around tandem circular cylinders	16
2.2.1	Interference regions	16
2.2.2	Flow patterns	18
2.2.3	Pressure distributions and fluctations	20
2.2.4	Strouhal number	22
2.2.5	Three-dimensionality	23
2.3	OpenFOAM	24
3	Numerical solver methods in OpenFOAM	27
3.1	Governing equations of fluid flow	27
3.1.1	Mass conservation - the continuity equation	27
3.1.2	Momentum conservation	28
3.2	The Finite Volume Method	29
3.3	Linear interpolation	30
3.4	Solution algorithm PISO for pressure-velocity coupling	31
3.5	Turbulence modeling and LES	32
4	Numerical setup	35
4.1	Computational domain and grid	35
4.1.1	Domain	36
4.1.2	Grid	36
4.2	Boundary and initial conditions	38
4.3	Grid verification	39
4.4	Solver settings	41
4.5	Visualization	42
4.5.1	Vortex identification	42
4.5.2	Streamlines	44
5	Results	45

5.1	Vorticity distribution	45
5.2	Wake flow	48
5.3	Mean and RMS pressure distributions	50
5.4	Drag and lift coefficients	55
5.5	Strouhal number	57
5.6	Separation	59
6	Conclusion	63
6.1	Conclusion	63
6.2	Practical relevance	64
6.3	Recommentadions for further work	65
	Bibliography	69
A	Visualization and results	I
A.1	Drag- and lift time history of coarse mesh	V
B	OpenFOAM scripts	VII
B.1	controlDict	VII
B.2	wallBoundedStreamLines	X
B.3	fvSchemes	XII
B.4	fvSolution	XIII
B.5	LESProperties	XV

Nomenclature

δ	Boundary layer thickness
ρ	Density of fluid
θ	Position in degrees over cylinder surface
ν	Kinematic viscosity
μ	Dynamic viscosity
τ	Shear stress
$\frac{\partial u}{\partial i}$	Horizontal velocity gradient in i-direction, $i = x, y, z$.
C_D	Drag coefficient
\bar{C}_D	Mean drag coefficient
C_{Di}	Interference drag coefficient
C_L	Lift coefficient
C_p	Pressure coefficient
\bar{C}_p	Mean pressure coefficient
C'_i	R.M.S, or fluctating coefficient
C_{pbi}	Base pressure coefficient for cylinder i where $i=1,2$.
C_{pgi}	Gap pressure coefficient for cylinder i where $i=1,2$.
D	Diameter
F_D	Drag force
F_L	Lift force
f_v	Vortex shedding frequency
g	Gravitational acceleration
p	Pressure
Re	Reynolds number
S/D	Ratio of space between two cylinder centers and their diameter
St	Strouhal number

T_v	Vortex shedding period
U_c	Free stream velocity/Far field velocity
u	Velocity in x-direction
v	Velocity in y-direction
w	Velocity in z-direction

Abbreviations

2D - Two-dimensional

3D - Three-dimensional

CFD - Computational Fluid Dynamics

FEM - Finite Element Method

LES - Large Eddy Simulation

PDE - Partial Differential Equation

PIV - Particle Image Velocimetry

RANS - Reynolds Averaged Navier-Stokes

RMS - Root Mean Square

VIV - Vortex Induced Vibrations

WIV - Wake Induced Vibrations

Chapter 1

Introduction

Circular cylinders are frequently encountered in the marine offshore industry. Examples are risers used for drilling and bringing hydrocarbons to the surface, the hull of a SPAR-platform, pipelines on the seabed, fish nets in fish farms, suction piles and the columns of a semi submersible. All of these examples represent different configurations of circular cylinders. Examples of applications with two or more circular cylinders are multiple risers expanded from the side of a rig, the legs of an offshore platform and dual pipelines. The tandem cylinders arrangement as the basis of the multiple cylinder case.

All of these different configurations of circular cylinders will induce flows behind them that will be different to each other. It is very interesting to investigate how fluid flow is affected by the change in arrangement of the cylinders. Any type of blockage or change in geometry will lead to changes on the flow which can result in unexpected response of the constructions. It is not only in the offshore industry we encounter circular cylinders in a variety of configurations. Most of the research done on the topic is based on the aviation industry where air flow over components on air planes were investigated. Chimneys, TV towers, wind turbines, nuclear power plants as well as heat exchangers are some other examples of circular cylinder application in engineering technology. It is interesting to understand the flow around tandem cylinders to be able to optimize designs and avoiding large movements of the downstream cylinder.

1.1 State of the art

It is obviously of huge practical importance to understand as much as possible about flow around circular cylinders. Due to the extensive use of them in numerous engineering designs, the topic has already received a large amount of attention. There exist numerous reviews of the state of the art of flow around circular cylinders, see for example [Berger and Wille \(1972\)](#), [Bearman \(1984\)](#) and [Sarpkaya \(2004\)](#). These papers sum up the theoretical background and what has been done regarding experiments in addition to the results of these. M. M. Zdravkovich has written books regarding this topic, and the first volume, [Zdravkovich \(1997\)](#), focuses on the fundamentals. Previous research are revised in the book. Circular cylinders is here and in other literature called bluff bodies because they generate a separated flow over a large part of the surface, ([Bearman, 1984](#)).

In recent years, the focus has mainly been to find good numerical and mathematical models for analyzing the flow around a circular cylinder. [Gabbai and Benaroya \(2005\)](#) reviewed the mathematical and numerical methods for investigating the flow.

As previously mentioned, most of the research done on fluid flow around circular cylinders originates from aerodynamics. The first known research done on tandem cylinders (to the knowledge of this author) dates back to 1915 and 1933 when cylinders and streamlined struts were used to support wings on aeroplanes, ([Pannell et al., 1915](#)) and ([Biermann and Herstein Jr, 1933](#)). The latter defined the interference drag, C_{Di} which is the difference between the drag coefficients of tandem struts and the struts tested separately. This was done for a Reynolds number of $Re=0.65 \cdot 10^5 - 1.63 \cdot 10^5$, which is in the subcritical flow regime. It was found that the drag of the downstream cylinder was decreased in the proximity of the upstream cylinder. The lowest C_{Di} was for the minimum spacing of $S/D=1$, where S is the center-to-center distance between the cylinders and D is the cylinder diameter, and increased with increasing spacing. For spacings of more than 4 diameters, the magnitude of interference did not change much. The upstream cylinder had a C_{Di} of approximately zero with the exception for a spacing of 3.5 diameters. Here, the cylinder got a negative C_{Di} . At this location, a rapid decrease in the downstream cylinder C_{Di} occurred. Since this first paper was published, numerous people have done research on tandem cylinders, and extensive reviews have also been published, for example [Sumner \(2010\)](#).

The minimum in C_{Di} was assumed to be due to a change of flow pattern in the gap between the cylinders ([Zdravkovich and Pridden, 1977](#)). [Zdravkovich and Pridden \(1977\)](#) refer to an article written by Zdravkovich and Stanhope, ([Zdravkovich and Stanhope, 1972](#)), where experiments with the gap flow as well as the wake flow was traversed with a hot-wire. The Reynolds number region was the same as for the experiments by [Biermann and Herstein Jr \(1933\)](#). In this way the velocity profiles could be found. It was revealed that for a spacing of 3.5 diameters the flow regime in the gap changed suddenly, represented by a discontinuity in the pressure coefficient profile. This spacing was called *critical spacing*. At this spacing, vortices form behind the upstream cylinder and impinges the downstream cylinder, ([Zdravkovich, 2003](#)), chapter 26.2.3.

[Igarashi \(1981\)](#) measured mean and rms pressures, C_p and C'_p , respectively, and used the results to classify the flow in five different categories for different spacings and Reynolds numbers. The experiments were conducted for a Reynolds number range of $8.7 \cdot 10^3 \leq Re \leq 5.2 \cdot 10^4$ and spacings of $1.03 \leq S/D \leq 5$. He also pointed out some Reynolds number dependencies of the flow. Especially in the range of $1.03 \leq L/D \leq 2$ it was found a large Re-dependency on the flow pattern. In Re-regions where the flow pattern did not change for a certain spacing, it was found that the profiles of C'_p had the same shape, but different magnitude. Igarashi also pointed out that unstable and bistable flows occur in the transition between two flow patterns. In these types of flows, different flow pictures are present for the same Re and it switches between them. The reattachment points for reattachment flow regime were also discussed, and discrepancies in different research were pointed out. Igarashi concluded that the reattachment point depends on Reynolds number and spacing.

Later, [Ljungkrona and Sundén \(1993\)](#) also stated that the flow between and around two cylinders in tandem depended on Reynolds number and spacing. They did flow visualization of flow around tandem cylinders for $3.3 \cdot 10^3 < Re < 12 \cdot 10^3$ and spacings of $1.25 < L/D < 4$ by application of smoke-wire technique. Pressure measurements were done for $3 \cdot 10^3 < Re < 4 \cdot 10^4$ and for spacings of $S/D = 1.25, 2.0, \text{ and } 4.0$. They found the change of flow pattern to be

reflected in the mean and rms pressure distributions and the Strouhal number, St . They also connected the change in critical spacings for different Reynolds numbers to the change in vortex formation length for the same Re and used this to explain the changes in flow patterns with changing spacing and Re . [Alam et al. \(2003\)](#) also reported the importance of spacing on different parameters, but focused on the fluctuating forces. They also commented on the influence of separation point on the forces.

Recently, better methods have been developed for flow visualization and numerical methods have been applied to simulate flows. Particle Image Velocimetry (PIV) was used by [Lin et al. \(2002\)](#) to in more detail see the flow structure in the gap between two cylinders in tandem and in the near wake of the downstream cylinder. [Alam \(2014\)](#) used surface oil-flow visualization to investigate the connection between fluctuating lift- and drag coefficient and St , and the dependency of Re and spacing. Flow patterns were also further investigated and the 'kink' in C_D distribution, commented by [Zdravkovich and Pridden \(1977\)](#), was explained as when the shear layer from the upstream cylinder reattaches onto the front surface of the downstream cylinder and sweeps to the other side of that cylinder.

CFD has as mentioned been given a lot of attention in recent years. But there has been significant discrepancies in the results for the different research done, independently of different solver models. This was reported by [Eça et al.](#) This article describes the scatter of results for numerical simulation of flow around a single cylinder, so it is logical to assume that this also is the case for tandem cylinders.

Because of the highly complex flow picture around two tandem cylinders, a significant amount of data power is required to do numerical simulations of the flow. This was not available in the beginning, and the first numerical research were thus conducted for two-dimensional flow at low Reynolds numbers. [Meneghini et al. \(2001\)](#), for example, modeled 2D flow around tandem cylinders for Reynolds numbers of 100 and 200 using the fractional step Finite Element Method (FEM). Due to the development of new technology and the use of supercomputers, it is now possible to simulations for more complex flows of higher Re and in 3D. [Papaioannou et al. \(2006\)](#) reported that a 2D simulation under-predicts the critical spacing which leads to error in results for forces and Strouhal numbers for a range of spacings with different flows. Later, [Afgan et al. \(2011\)](#) did Large Eddy Simulations (LES) on two side-by-side circular cylinders in subcritical Reynolds numbers and found that the solution is not influenced for a spanwise length of 4 diameters.

More recent tandem cylinder simulations where LES-models are used includes [Kitagawa and Ohta \(2008\)](#). They did LES simulations with Smagorinsky subgrid-scale model for tandem cylinders with spacings in the range of $2 \leq S/D \leq 5$ and with Reynolds number $Re = 2.2 \cdot 10^4$. The model will be explained in section 3.5. The focus of the research was to study the behavior of the vortices shed from the upstream cylinder and the effect these have on the downstream cylinder. [Uzun and Hussaini \(2012\)](#) used delayed detached eddy simulations for cylinders with spacings $S/D = 3.7$ and Reynolds number $Re = 166,000$. The scope was to evaluate the sensitivity to grid resolution and used up to 133 million grid points. [Sainte-Rose et al.](#) used variational multi-scale LES and classic LES methods to simulate flow around tandem cylinders. The scope of this research was to demonstrate the suitability of the variational multi-scale method.

Tandem cylinders have also been investigated in other configurations. [Springer et al.](#) modeled two tandem circular cylinders that were subjected to vibrations. A combination of a FEM model and detached eddy simulation was used. [Assi and Bearman](#) did experiments on

Vortex Induced Vibrations (VIV) and Wake Induced Vibrations (WIV) of two tandem cylinders with fairings. Recently, [Abrahamsen-Prsic \(2015\)](#) did LES simulations to model tandem cylinders in the vicinity of a wall. This is the research that inspired the scope of this thesis.

1.2 Motivation

CFD is a useful tool for analyzing flows, both disturbed and undisturbed. When we analyze flow around bodies with CFD, we can get information which we cannot get from experiments. We can see how the flow actually will behave around the body. Velocities and pressure can be measured in all points of the simulated domain and the actual forces inflicted on the body can be obtained. CFD simulation is also cheaper than doing experiments, and at the present time CFD can replace or compliment many experiments. This author believes that CFD will play a huge role in flow analysis in the future, even more than it does today. It is desired to further develop CFD as a tool for doing different types of simulations to make this happen.

The flow around tandem cylinders at high Reynolds numbers can be described as very complex and large variations in the flow picture can be seen when changing parameters such as spacing between the cylinders and Reynolds number. This arrangement of circular cylinders is also very relevant for practical use. The Reynolds number of 13100 is a Reynolds number that is often obtained in full scale applications of tandem cylinders. Tandem arrangements are frequently encountered in the offshore industry and accidents have happened due to for example large motions of risers. It is thus need for research on the topic. Understanding the flow around tandem cylinders is also fundamental for understanding the flow around multiple cylinders. With the possibility to use the super-computer Vilje at NTNU, it is possible to model the flow around tandem cylinders in a way that would be impossible with a normal computer.

As of now, the forces inflicted on a body from the fluid flow, and the response this body have to be modeled in separate ways. This is due to the use of different models for the fluid and the structure of the body. In a CFD simulation we can give the body forced oscillations or keep it fixed. However, by further development of the CFD programs, and by use of new technology and more powerful computers, it might be possible in the future to combine the structural and hydrodynamical models. Then the response of the body can be modeled directly from the forces the fluid flow is inflicting on it. CFD is thus a tool that is very relevant for future use and exciting to learn about. The author finds it very important to be able to use the program correctly, such that the flow is modeled in the best way.

A program that is widely used for CFD simulations is OpenFOAM. This is the program used in this study. OpenFOAM is an open source which means that you can easily modify the software to use for different applications. It is easy to access the program files and inspect them or change them, which makes it possible to understand what the program is actually doing. OpenFOAM has some disadvantages that follows from the wide spectra of schemes and solvers. There is no default settings in the program, and with the numerous available schemes it is easy to make a mistake while setting up the computation. For an OpenFOAM user it is thus important to understand the schemes and boundary conditions implemented on the simulation to get results that are reliable.

1.3 Structure of the Thesis

The rest of the thesis is organized as follows:

Chapter 2 gives an overview of the theory behind flow over circular cylinders and further literature review as well as an overview of numerical simulation.

Chapter 3 gives an introduction to the numerical schemes in OpenFOAM which is applied in this work.

Chapter 4 describes the numerical setup in this thesis. Boundary conditions, grid verification and post processing tools and methods will be assessed.

The results of the work are presented in **chapter 5** by vorticity distribution, wake flow, pressure distributions, drag- and lift coefficients, Strouhal number and flow separation.

A conclusion is provided in **chapter 6**.

Chapter 2

Background theory

The flow around circular cylinders is characterized by numerous complex physical phenomena. Even more so is the flow over two circular cylinders in tandem arrangement. To be able to understand the flow around tandem cylinders it is important to know the basics of flow around one circular cylinder. Each cylinder in tandem arrangement will see the same aspects of flow as a single cylinder, but due to the presence of another cylinder, there will be some disturbances.

In this chapter, the theory behind these physical phenomena will be explained. The different aspects of flow characteristics will be explained individually such as to make it as simple and lucid as possible. The flow around tandem cylinders will also be assessed in this chapter.

2.1 Flow around one circular cylinder

[Zdravkovich \(1997\)](#) defines four regions of disturbed flow around a bluff body:

- One narrow region of retarded flow in front of the cylinder where the flow "hits" the body in the stagnation point.
- Boundary layer close to the surface of the body. Both on the top and bottom.
- Regions of disturbed flow over and under the body.
- The wake behind the body.

The extent of these regions is dependent on the size, shape and orientation of the body as well as the viscosity and the velocity of the fluid. The characterization of disturbed flow is that the local velocity varies in direction, magnitude and time.

The fluid dynamics research is said to have started with Archimedes and his formulation of the buoyancy principle around 200 BC. After this many individuals contributed to the development of the fluid dynamics theory ([Cengel and Cimbala, 2010](#)). In the beginning, *potential flow theory* was developed to describe the flow around bluff bodies. In this theory it is assumed that the flow is incompressible, irrotational and inviscid. The two latter is not the case for a water flow, especially close to the body. In reality the fluid particles closest to the body will move with the same velocity as the body. This means that for a body with zero velocity, the fluid particles at the body surface will too have zero velocity. In addition, there

is a requirement that there can not be any sudden changes in the velocity. Due to this, a boundary layer is present close to the cylinder (Pettersen, 2007).

Generally, for non-separated flow at high Reynolds number, the viscous effects are small and can be neglected. For a circular cylinder this is in the angle interval before flow separation and outside the boundary layer. In this region potential flow theory is considered valid.

To be able to model complex flows around different kinds of geometries and configurations, we need to take into account that the flow can be rotational and viscous. This will have a major impact on the flow structure.

2.1.1 Boundary layer

The boundary layer makes us unable to use potential theory equations like the simplified Euler and Bernoulli which are only valid for potential theory (Cengel and Cimbala, 2010). It was Prandtl, (Prandtl, 1904), who first acknowledged that the boundary layer existed in his pioneering paper from 1904. Potential theory cannot be used to model the flow in the boundary layer. Here frictional forces are significant and the flow thus becomes viscous. The tangential shear stress is proportional to the velocity gradient, $\tau \sim \frac{\partial u}{\partial y}$.

As mentioned earlier, the velocity cannot make sudden changes. In addition to the fact that the velocity on the cylinder surface is zero, the change in velocity at a distance from the cylinder has to be gradual. The thickness of the boundary layer is defined as the distance from the cylinder surface where the horizontal velocity becomes equal to 0.99 of the outer velocity, $u(y) = 0.99U(x)$, (Schlichting and Gersten, 2000).

The boundary layer thickness is assumed to be $O(\frac{1}{\sqrt{Re}})D$. Roughly, its value is given as:

$$\delta = \frac{D}{\sqrt{Re}} \quad (2.1)$$

The velocity profiles in the boundary layer is not the same all over the cylinder and thus the boundary layer thickness changes over the surface. This can be seen in figure 2.1. The red-dotted lined in figure 2.1 shows the boundary layer thickness. The velocity profiles at certain points is given along the cylinder surface. The velocity gradient $\frac{\partial u}{\partial y}$ is clearly largest close to the surface, and the presence of the velocity gradient implies that the flow in the boundary layer is viscous.

It can be seen that the boundary layer ends where the velocity profiles are fully developed. The y-axis represents the distance from the cylinder surface. At a certain point the flow will separate from the surface. This is called the separation point. At point E, backflow is identified. This will cause a roll-up of the shear layer and lead to vortex formation.

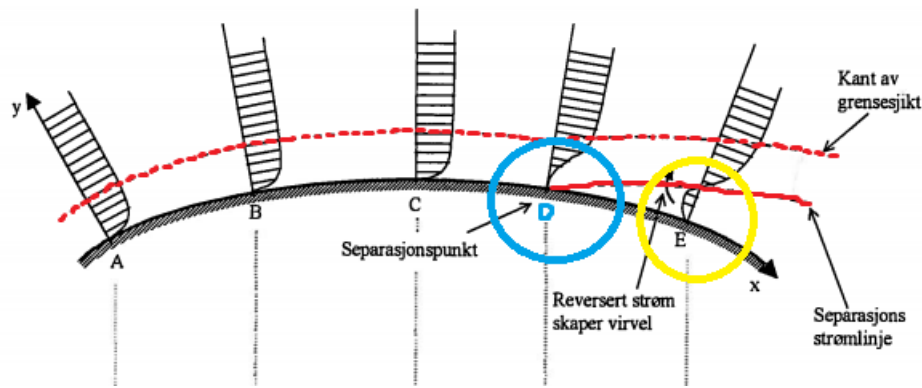


Figure 2.1: Boundary layer aspects on a circular cylinder. Figure taken from [Pettersen \(2007\)](#).

2.1.2 Flow separation

An easy explanation of flow separation is that the flow leaves the surface of the body. After the boundary layer has separated from the body, it moves downstream as a free shear layer. As mentioned in section 2.1.1, the backflow of the fluid particles closest to the body surface at a point after the separation point will result in formation of a vortex here. The vortices created at the surface will separate from the body and move downstream in the wake. This creates a chaotic wake flow, especially for high Reynolds numbers. The wake is the region behind the body with disturbed flow due to the presence of the body itself.

For a bluff body with sharp edges, such as a square or triangular cylinder, the flow will separate at the sharp edges. This is not the case for a circular cylinder. The separation points can move as a result of changes in the flow picture in the region ([Zdravkovich, 1997](#)).

Separation of flow over a circular cylinder is directly connected to the pressure distribution in the boundary layer, ([Schlichting and Gersten, 2000](#)). In potential flow theory, there is no friction in the flow. The pressure distribution over the cylinder surface would thus be symmetric. This can be seen in figure 2.2, where pressure distributions are plotted for potential and real flow for a Reynolds number of 100. θ is given as 0 degrees in front of the cylinder where the incoming flow hits the cylinder.

For potential flow, the pressure gradient is negative over the first half of the cylinder and the pressure is thus decreasing. This is because the fluid accelerates to get past the thicker part of the cylinder. The opposite happens when the fluid passes the first half of the cylinder and it is decelerated and the pressure increases. Because the fluid is frictionless, there is no loss of energy and the pressure distribution is symmetric.

The real fluid accelerates over the first half of the cylinder and we see similarities to the potential pressure distribution. The acceleration causes the breaking effect of the boundary layer to be less significant. Owing to the friction in the boundary layer, particles, especially those close to the body surface, lose large amount of their kinetic energy ([Schlichting and Gersten, 2000](#)). The loss of kinetic energy can be seen in figure 2.2 as the pressure coefficient of the real flow has smaller values than that of the potential flow.

On the other half of the cylinder, the pressure gradient is positive. The fluid has now moved past the thickest point of the cylinder and the velocity is decreasing, causing the pressure to increase again. The kinetic energy of the particles is now too small to overcome the pressure increase the potential flow experience over the second half. The motion of the particles are

thus stopped. This effect is strongest closer to the cylinder surface since the velocity gradient, and thus friction, is largest here. The result is that the particles will start to move in the opposite direction due to the external pressure, (Schlichting and Gersten, 2000), which is the backflow phenomena identified in figure 2.1. The velocity gradient is thus less than zero, and the backflow will cause vortex formations behind the cylinder, (Petterson, 2007).

The separation point, however, is located in front of the backflow point, and can be seen as where the pressure coefficient curve flatten out. This is marked by the blue circle in figure 2.1. The velocity gradient is zero in this point. It is easily seen that there is no separation point or vortex formation in potential flow theory, due to the symmetric pressure distribution. This coincides with the irrotational flow assumption of potential flow theory.

Mathematically, it is stated that at the surface of the cylinder ($y=0$), $u = 0$, $v = 0$, $\tau_0 = \mu \frac{\partial u}{\partial y_0}$. The Navier Stokes equation for the boundary layer is given as:

$$u \frac{\partial u}{\partial x} + v \frac{\partial u}{\partial y} = -\frac{1}{\rho} \frac{\partial p}{\partial x} + \nu \frac{\partial^2 u}{\partial y^2} \quad (2.2)$$

The Navier Stokes equation will be described shortly in section 2.1.3.

Because of the given terms equal to zero, equation 2.2 is reduced to:

$$\frac{\partial p}{\partial x} = \nu \frac{\partial^2 u}{\partial y^2} \quad (2.3)$$

From equation 2.3 it follows that when the pressure gradient, $\frac{\partial p}{\partial x}$, is negative, $\frac{\partial^2 u}{\partial y^2} < 0$ at the wall. This means that the velocity gradient, $\frac{\partial u}{\partial y}$, is maximum at first and then decreases outwards in the boundary layer. The velocity profile associated with this is shown in figure 2.3 as the velocity profile at $\theta = 50$ degrees.

If $\frac{\partial p}{\partial x} > 0$, it means that we have an adverse pressure gradient and the pressure will enforce the breaking of the boundary layer. This can be seen in the velocity profiles. Now, $\frac{\partial^2 u}{\partial y^2} > 0$, and the velocity gradient will thus decrease at first, then increase. This is seen in the velocity profiles at $\theta = 120$ degrees and $\theta = 130$ degrees in figure 2.3. As the adverse velocity gradient becomes larger, this breaking effect will become more prominent and at a point the velocity gradient will become zero and the flow separates. The velocity profile at $\theta = 120$ degrees shows a zero velocity gradient close to the wall. The separation point will be close to this point. At $\theta = 130$ degrees, the velocity gradient is negative close to the wall, and here we will see backflow.

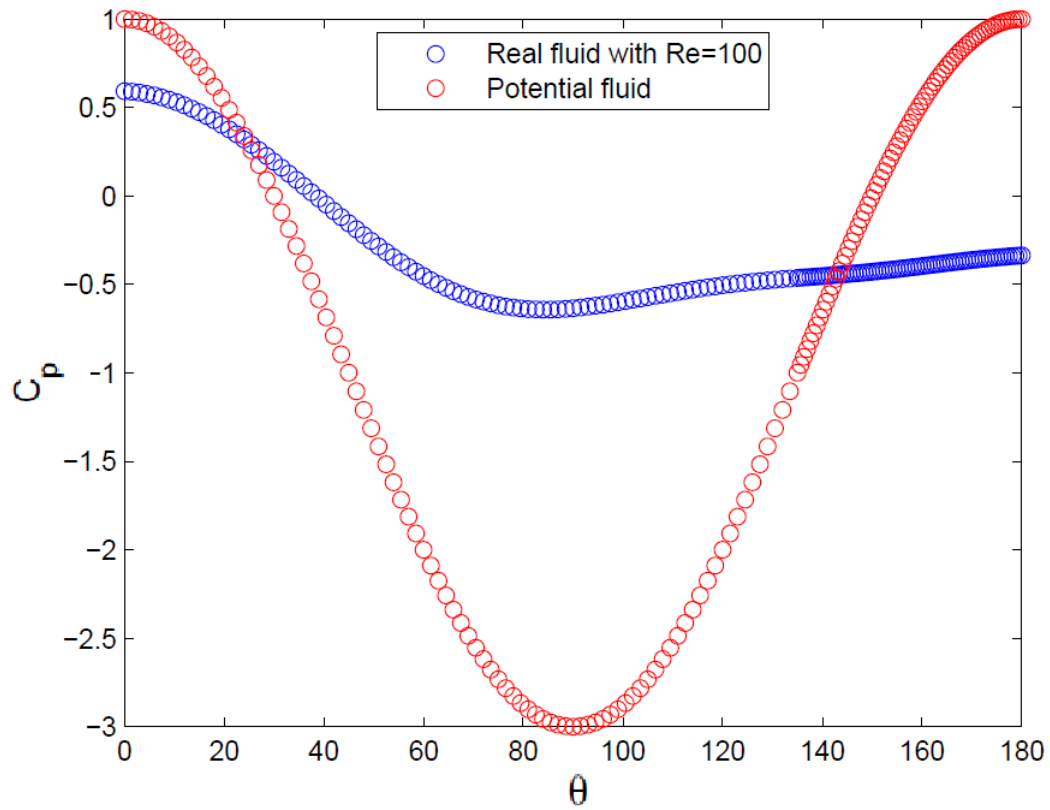


Figure 2.2: Pressure distributions for real fluid and potential fluid plotted over the cylinder surface. Results for real fluid is taken from simulations done in the master project, fall 2014.

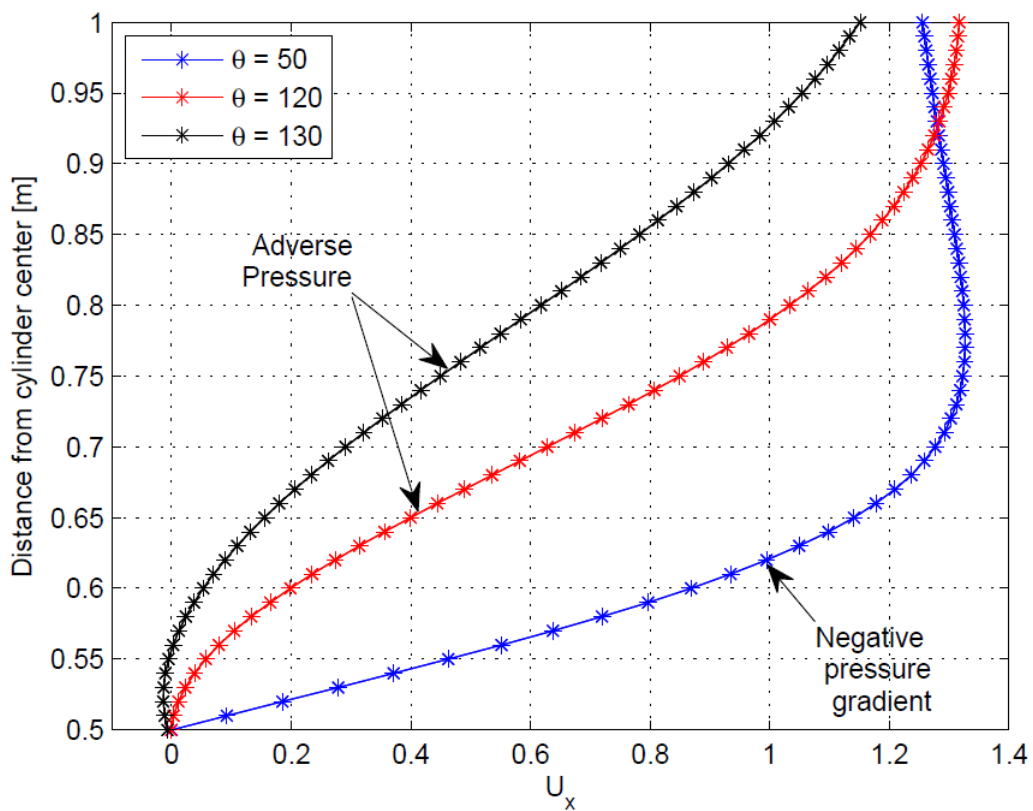


Figure 2.3: Velocity profiles at 3 different locations along the cylinder surface for $Re=100$

The location of the separation point is dependent on the Reynolds number of the flow. When the Reynolds number is high and the flow becomes turbulent the separation point is further back on the cylinder such that the wake gets narrower. This is because turbulent flows can overcome much larger adverse pressure gradients without separating, ([Schlichting and Gersten, 2000](#)).

When the pressure is integrated over the cylinder surface, the pressure-induced drag force can be found. From figure 2.2 it is clear that the net pressure over the cylinder surface is non-zero for the real fluid and the pressure-induced drag force is thus non-zero. For potential fluid, the pressure can be described by Bernoulli's equation. The equation involves one term with $\sin^2(\theta)$. This term is independent on the value of θ and the pressure is thus symmetrical around the cylinder. This results in zero pressure-induced drag force. This is known as d'Alembert's paradox ([Pettersen, 2007](#)). The pressure-induced drag is not the only contribution to the drag force. The viscous fluid will cause a friction force on the cylinder which contributes to the drag force. In the laminar flow regime (at low Reynolds numbers) this contribution is significant, about 20% in the transitional wake region. At higher Reynolds numbers the effect of viscous friction can be neglected ([Zdravkovich, 1997](#)).

Vortex shedding and oscillating forces

This section is based on theory from [Sumer and Fredsøe \(1997\)](#). Vortex shedding happens when Reynolds number is larger than about 40. Before this a pair of vortices forms behind the cylinder and stays there. If the Reynolds number is increased from 40, the wake becomes unstable and vortices will be shed alternately from each side of the cylinder.

When the flow separates from the cylinder surface, a shear layer is formed in which there is vorticity. This vorticity causes the shear layer to curl up into a vortex which eventually will be shed from the cylinder. This happens when one vortex becomes larger than the one on the other side due to small disturbances. The large vortex will draw the smaller one across the wake. The two vortices have opposite signs. This means that they rotate in opposite directions. This will lead to the supply of vorticity to the large vortex will be cut off and thus shed. The smaller vortex will now grow larger and the same thing will happen for this one. The process repeats itself again and again.

We distinguish between two types of forces acting on a circular cylinder in incoming flow; the lift force and the drag force. The lift and drag force coefficients are given as:

$$C_L = \frac{F_L}{\frac{\rho}{2} U^2 S} \quad (2.4)$$

$$C_D = \frac{F_D}{\frac{\rho}{2} U^2 S} \quad (2.5)$$

Where S is a characteristic length. For a circular cylinder, $S=D$. F_L and F_D are the forces obtained by integrating the pressure over the cylinder surface. Looking back to figure 2.2, we see the pressure distribution over the cylinder surface for potential flow and real flow. If the pressure is integrated over the cylinder surface, the force acting on the cylinder will be obtained. Because the pressure force is normal to the cylinder surface, it is decomposed in

a vertical components and horizontal component. The vertical component is the lift force while the horizontal component is the drag force.

It is this vortex shedding that causes the oscillation of the lift- and drag forces on a cylinder. The lift forces oscillate with a mean value of zero because the lift is only induced by the alternating vortex separation while the drag force has a non-zero mean value. This is because the skin friction also gives a drag force in addition to the pressure induced drag which is a result of the vortex shedding. Figure 2.4 shows the vortex shedding process for a single cylinder at Reynolds number of 100.

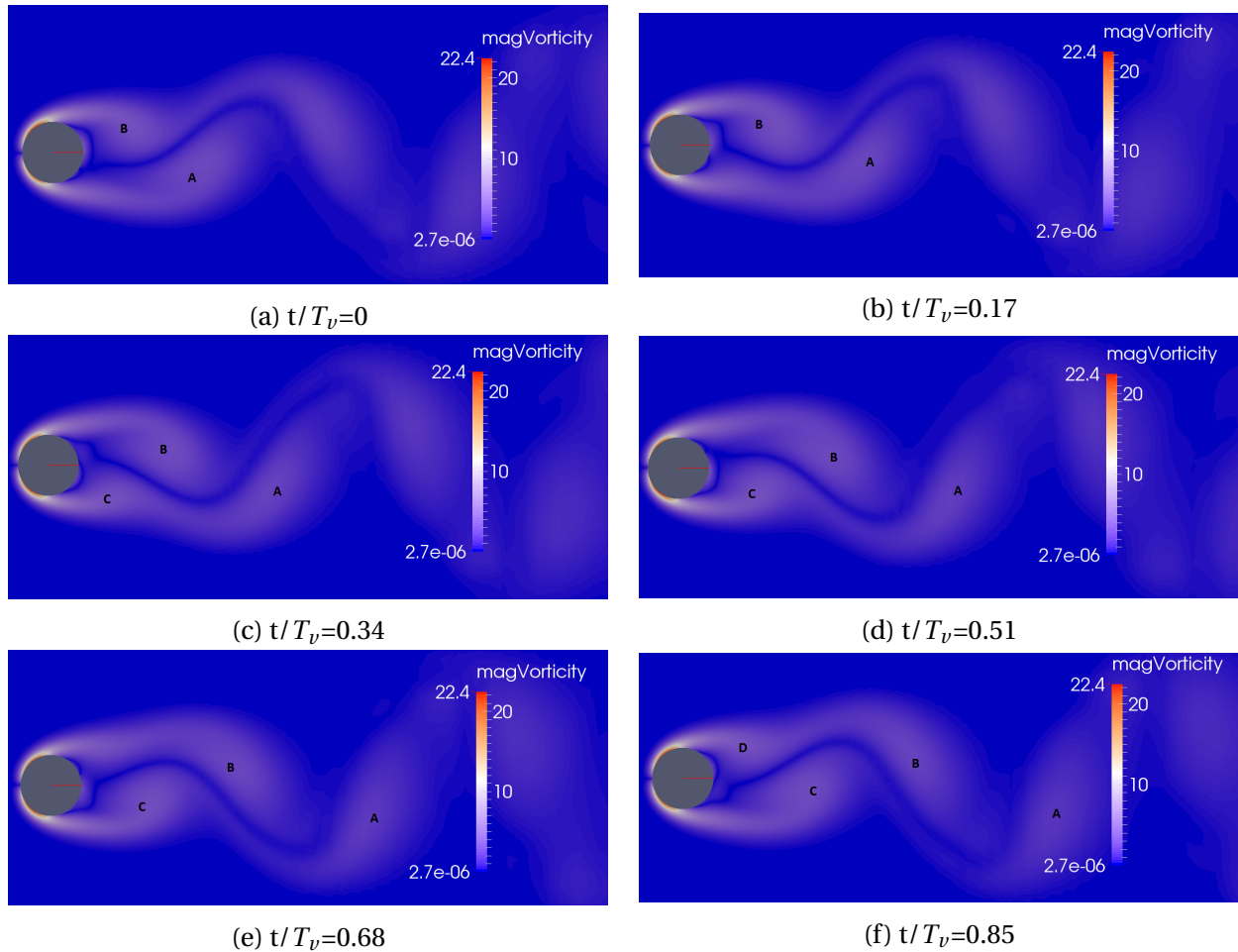


Figure 2.4: Plot of magnitude of vorticity for Reynolds number 100 that shows vortex shedding from a single cylinder. Figures are taken from master project fall 2014.

In figure 2.4 we see that vortex A has just cut another vortex off from the vorticity in the shear layer and a new vortex, B, has developed. B is then dragged across the wake and separates A, and a new vortex, C, is created. Vortex A is transported downstream in the wake. In the last picture, vortex C is about to separate B and a new vortex, D, is developing.

The frequency of the vortex shedding is expressed dimensionless by the Strouhal number. This is given as:

$$St = \frac{f_v D}{U_c} \quad (2.6)$$

Where f_v is the vortex shedding frequency. The lift force oscillates with this frequency. This is because the lift changes direction as the vortex shedding changes side of the cylinder. This is due to sensitivity to variations in the transverse direction. The drag force on the other hand is not, and oscillates with frequency $2f_v$.

If the flow is not steady but oscillating, the vortex shedding is dependent on the oscillation period. If the period is too small the vortices do not have time to develop and shed before the flow changes direction. There will thus be no vortex shedding. This could be the case of a circular cylinder piercing the free surface and the flow is induced by waves (Pettersen, 2007). The Keulegan-Carpenter number is used to classify these cases. The Keulegan-Carpenter number is given as:

$$KC = \frac{U_c T}{D} \quad (2.7)$$

Where U_c is the incoming velocity, T is the flow oscillation period and D is the cylinder diameter. Vortices will shed for a KC-number higher than 7-8.

Reynolds number

The Reynolds number is named after Osborne Reynolds who found out that the flow regime of the fluid mainly depends on the ratio of inertia forces to viscous forces (Cengel and Cimbala, 2010). It is given as:

$$Re = \frac{\text{Inertia forces}}{\text{Viscous forces}} = \frac{V_{avg} D}{\nu} = \frac{\rho V_{avg} D}{\mu} \quad (2.8)$$

If the ratio of the inertia forces and viscous forces is the same for two flows in the same direction, there is a geometrical similarity of the streamlines. This is called *mechanical similarity*, (Schlichting and Gersten, 2000). In the case of a cylinder with incoming uniform flow, V_{avg} will be equal to the incoming flow velocity U_c . D is a characteristic length which in this case is the cylinder diameter. μ is the dynamic viscosity of the fluid.

At high Reynolds numbers the inertia forces will dominate the viscous forces. This can be seen from equation 2.8 since the inertia forces are related to the fluid velocity. This also explains why the viscous friction forces can be neglected at high Reynolds numbers. Another consequence of this is that the viscous forces cannot compensate for the random fluctuations in the fluid, and it thus becomes turbulent. At lower Reynolds numbers this is not the case. Here the viscous forces are significant and they keep the fluid in line, and thus laminar flow.

Depending on what the Reynolds number of the flow is, different flow regimes will occur. An overview of the different flow regimes and for which Reynolds number they occur is given in figure 2.5. The figure is taken from Sumer and Fredsøe (1997).







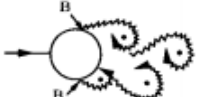


a)		No separation. Creeping flow	$Re < 5$
b)		A fixed pair of symmetric vortices	$5 < Re < 40$
c)		Laminar vortex street	$40 < Re < 200$
d)		Transition to turbulence in the wake	$200 < Re < 300$
e)		Wake completely turbulent. A: Laminar boundary layer separation	$300 < Re < 3 \times 10^5$ Subcritical
f)		A: Laminar boundary layer separation B: Turbulent boundary layer separation; but boundary layer laminar	$3 \times 10^5 < Re < 3.5 \times 10^5$ Critical (Lower transition)
g)		B: Turbulent boundary layer separation; the boundary layer partly laminar partly turbulent	$3.5 \times 10^5 < Re < 1.5 \times 10^6$ Supercritical
h)		C: Boundary layer comple- tely turbulent at one side	$1.5 \times 10^6 < Re < 4 \times 10^6$ Upper transition
l)		C: Boundary layer comple- tely turbulent at two sides	$4 \times 10^6 < Re$ Transcritical

Figure 2.5: Regimes of flow around a circular cylinder in a steady current. Figure taken from [Sumer and Fredsøe \(1997\)](#).

In OpenFOAM the Reynolds number itself is not specified, but it is accounted for when specifying the dynamic viscosity. This is the only parameter that is given to the program. We thus choose a Reynolds number that we want to simulate for in addition to an incoming velocity. The cylinder diameter is known as well as the fluid density, ρ . Equation 2.8 is then solved with respect to μ and the value of it is given to the program.

2.1.3 Modeling the fluid motions correctly - Navier Stokes equations

The boundary layer approximations mentioned earlier is, as the name implies, only an approximation. The equation is an approximation of is the Navier-Stokes equation. This equation is considered to model the fluid motion of viscous fluids satisfyingly. The Navier-Stokes equation will not be derived here, but it will be described shortly. The equation is given as:

$$\frac{\partial \mathbf{U}}{\partial t} + \mathbf{U} \cdot \nabla \mathbf{U} = -\nabla \frac{p}{\rho} + \nu \nabla^2 \mathbf{U} + \mathbf{g} \quad (2.9)$$

Equation 2.9 is a set of unsteady, nonlinear, second order, partial differential equations (Cengel and Cimbala, 2010) and is currently impossible to solve analytically for complex flow fields. It has four unknowns and there is only three equations, one for each dimension. The continuity equation is thus used as the fourth equation. The continuity equation is described in section 3.1.1.

The Navier-Stokes equation can be solved numerically, and that is what OpenFOAM is doing.

2.2 Flow around tandem circular cylinders

When a second cylinder is placed in the vicinity of the first one, considerable changes happen to the flow, vortex shedding and magnitude of forces, (Zdravkovich, 2003) relative to a single cylinder. It was first believed that the presence of the second cylinder would have no effect on the first one, but early experiments showed that this was not the case.

2.2.1 Interference regions

The cylinders can be arranged in infinitely many different ways, but three categories of arrangement are identified; tandem arrangement, side-by-side arrangement and staggered arrangement. In connection with the different arrangement of the cylinders, there are many different kinds of flow interference. Figure shows the different interference regions. The figure is taken from Zdravkovich (2003).

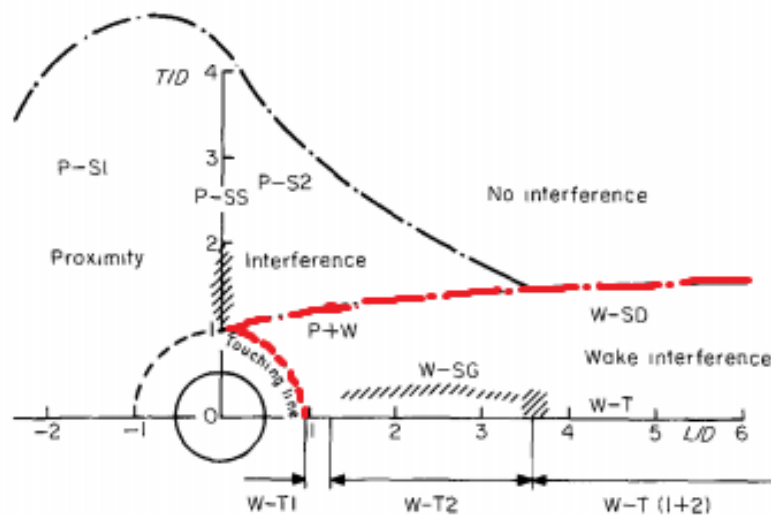


Figure 2.6: Regions of interference around a circular cylinder. Figure taken from Zdravkovich (2003).

In this work, attention is only given to the tandem arrangement, and we see from figure 2.6 that the tandem arrangement is in the wake interference region, which is marked by the red dotted line in figure 2.6. In this region, the downstream cylinder is submerged in the wake of the upstream cylinder and sees a disturbed incoming flow. The tandem cylinders experience

two types of wake interference; with or without vortex shedding from the upstream cylinder, but there are also subdivisions. [Zdravkovich \(2003\)](#) gives the following classification of the interference regimes.

- W-T1. Regime with no reattachment of the separated shear layer from the upstream cylinder onto the downstream cylinder. This happens for spacings $1 < S/D < 1.1 - 1.3$. The eddy street behind the cylinders is formed by the free shear layers from the upstream cylinder. It is often said that the two cylinders act as a single body in this regime.
- W-T2. In this region the free shear layer from the upstream cylinder reattaches onto the downstream cylinder either alternately, permanently or intermittently. Now, the vortex shedding only takes place behind the downstream cylinder. $1.1 - 1.3 < S/D < 3.5 - 3.8$
- W-T (1 or 2). This is a bistable regime. $3.0 < S/D < 4.0$. An intermittent change-over takes place with and without vortex shedding from the upstream cylinder.
- W-T (1+2) is the coupled vortex shedding regime. $3.8 < S/D < 5 - 6$. There are two vortex streets that are synchronized in phase and frequency. The vortices shed from the upstream cylinder pair with the vortices behind the downstream one.
- W-T (1,2). Here we see uncoupled vortex shedding, which happens for spacings $S/D > 5 - 6$.

All spacings are dependent on the Reynolds number. This was pointed out by [Ljungkrona et al. \(1991\)](#). Figure 2.7 shows that the critical spacing between two tandem cylinders vary with changing Re . The profile follows the one of the vortex formation length for one single cylinder. The figure is taken from [Ljungkrona and Sundén \(1993\)](#).

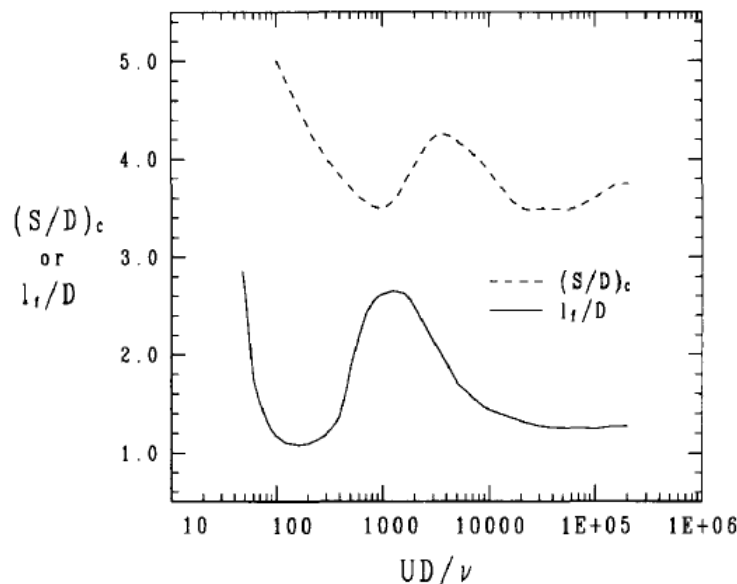


Figure 2.7: Critical spacing between two tandem cylinders and vortex formation length for a single cylinder as a function of Reynolds number. Figure taken from [Ljungkrona and Sundén \(1993\)](#).

The variation in critical spacing causes the interference regimes mentioned above not to be

set for certain spacings, but also to be dependent on Reynolds number.

2.2.2 Flow patterns

The different types of interference will naturally induce different flow patterns around the tandem cylinders. These flow patterns will vary with spacing and Reynolds number, as the interference regions do. Igarashi (1981) classified different flow patterns for different spacings and Reynolds numbers. This classification is shown in figure 2.8 and 2.9. Both figures are taken from Igarashi (1981).

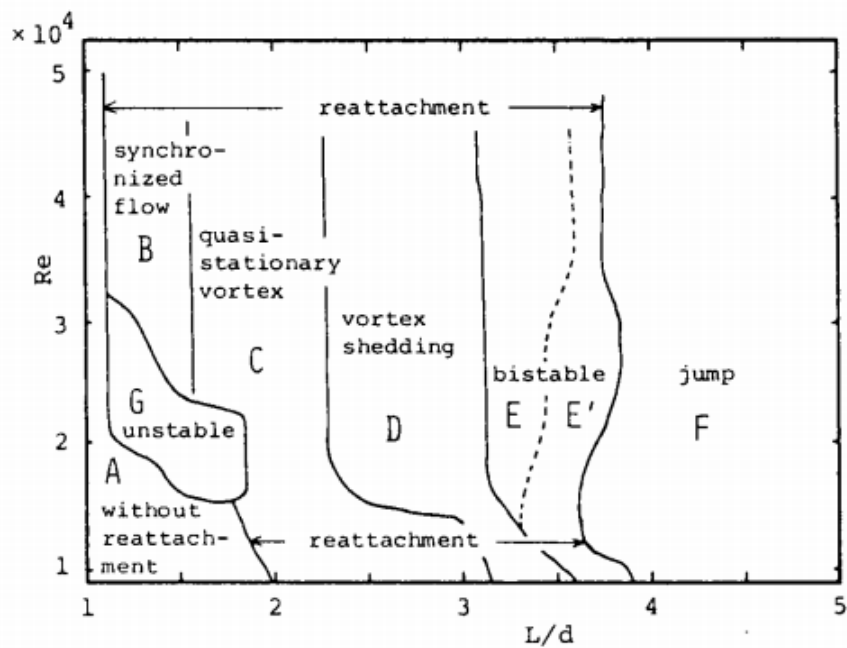


Figure 2.8: Classification of flow patterns for different spacings and Reynolds numbers. Figure taken from Igarashi (1981).

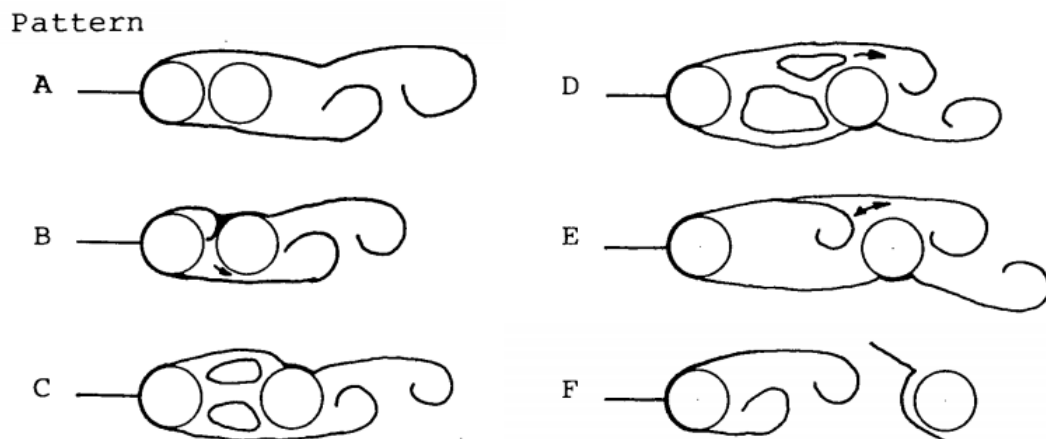


Figure 2.9: Different flow patterns for tandem cylinders. Figure taken from Igarashi (1981).

These patterns are described as follows, (Igarashi, 1981):

- A: The separated shear layer from the upstream cylinder does not reattach onto the downstream cylinder. The two cylinders act like a single body.
- B: Vortex formation of the shear layer and vortex shedding in the near wake of the downstream cylinder and reattachment of the other shear layer onto the downstream cylinder are synchronized. The frequency of the vortex shedding is nearly constant irrespective of the free stream velocity.
- C: Quasi-stationary vortices are formed between the cylinders.
- D: The quasi-stationary vortices become unstable and the vortex shedding is detected intermittently.
- E: The separated shear layer from the upstream cylinder rolls up intermittently for a moment in front of the downstream cylinder. This is a bistable flow between D and F.
- E': A bistable flow whose one pattern continues for a long time is predominant.
- F: The separated shear layer from the upstream cylinder rolls up in front of the downstream cylinder.
- G: Unstable flow in the transition region between patterns A, B and C.

For pattern A, the downstream cylinder is located inside the vortex formation region of the upstream cylinder and the free shear layers wrap around it. The shear layers become elongated compared to the ones of a single cylinder, the wake becomes narrower and vortex shedding happens for a higher Strouhal number, (Sumner, 2010). Ljungkrona and Sundén (1993) reported in their studies that the vortices behind tandem cylinders with flow pattern A is stronger for lower Reynolds numbers ($Re = 3.3 \cdot 10^3$) and the intensity decreases as the Reynolds number increases. This due to the longer formation length for the lower Reynolds numbers (see figure 2.7). The downstream cylinder suppresses the vortex formation more and more as the Reynolds number increases.

The reattachment region comprises patterns B, C, D, E, E' and G, (Sumner, 2010). Here, the shear layer from the upstream cylinder can no longer enclose the downstream cylinder and they start to reattach to it instead. Eddies may form in the gap between the cylinders. The gap flow is very complex and it has not yet been found a complete explanation of what happens in this region. In pattern B, there is a synchronization of reattachment of the upstream shear layer onto the downstream cylinder and a vortex shed from the opposite side of the downstream cylinder. In pattern C, quasi-stationary eddies are formed in the gap and the reattachment is nearly continuous. When the spacing is increased, intermittent vortex shedding from the upstream cylinder can happen in the gap. This is pattern D in the classification of Igarashi (1981).

In pattern F, there is vortex shedding from both cylinders. This happens as the critical spacing between the cylinder is reached. The vortices shed from the upstream cylinder impinge the downstream one and this triggers the vortex shedding of the downstream cylinder. This flow pattern is also called co-shedding because of this phenomena.

The difference between a bistable flow and an unstable flow is that the flow picture of an unstable flow last only for a very short time before it changes, while that of a bistable flow has a certain duration.

2.2.3 Pressure distributions and fluctuations

The pressure distributions around tandem circular cylinders tell us much of what happens regarding the flow picture. Because the pressure is a primary output from numerical simulations, this data gives us the most accurate information since it has not been subjected to manipulation in the software. It is thus important to recognize some of the most prominent characteristics of the pressure distribution profiles to be able to identify flow pictures.

There are obviously many dissimilarities between the pressure distribution of a single circular cylinder (as seen in figure 2.2) and those of tandem cylinders. Because the pressure distributions change with different flow pictures, these will vary with Reynolds number and spacing.

The different types of C_p distributions for the upstream and downstream cylinders are given by Zdravkovich (2003) as:

Upstream cylinder:

- (i) A positive pressure coefficient, C_p , in the stagnation point region
- (ii) Favorable and adverse pressure gradients along the surface
- (iii) Almost constant base pressure coefficient for upstream cylinder, C_{pb1} . Where the base pressure is the pressure at $\theta = 180$ degrees.

Downstream cylinder:

- (i) The base pressure behind the upstream cylinder, C_{pb1} faces the upstream side of the gap and the gap pressure on the downstream cylinder, C_{pg2} is exerted along the front side of the downstream cylinder. $C_{pb1} = C_{pg2}$ indicates that there is a lack of flow in the gap.
- (ii) If $C_{pg2} < C_{pb1}$, C_{D2} is negative and the drag force acts as a thrust
- (iii) There are two symmetric peaks in the pressure at the sides of the downstream cylinder for $S/D \sim 2$. This indicates reattachment of the shear layers from the upstream cylinder onto the downstream cylinder. These peaks are not seen for very small and very large spacings.

These types of pressure distributions were based on the results of experiments done by Hori (1959). These experiments were done for spacings of $S/D = 1.2, 2, 3$. And Reynolds number $Re = 8 \cdot 10^3$.

Later, Igarashi (1981) did extensive research on the pressure distribution around tandem cylinders in the subcritical flow regime. Figure 2.10 is taken from his experiments. They show the pressure distribution around the upstream and downstream cylinder for $Re = 3.5 \cdot 10^4$ and spacings varying from $S/D = 1.03 - 3.97$.

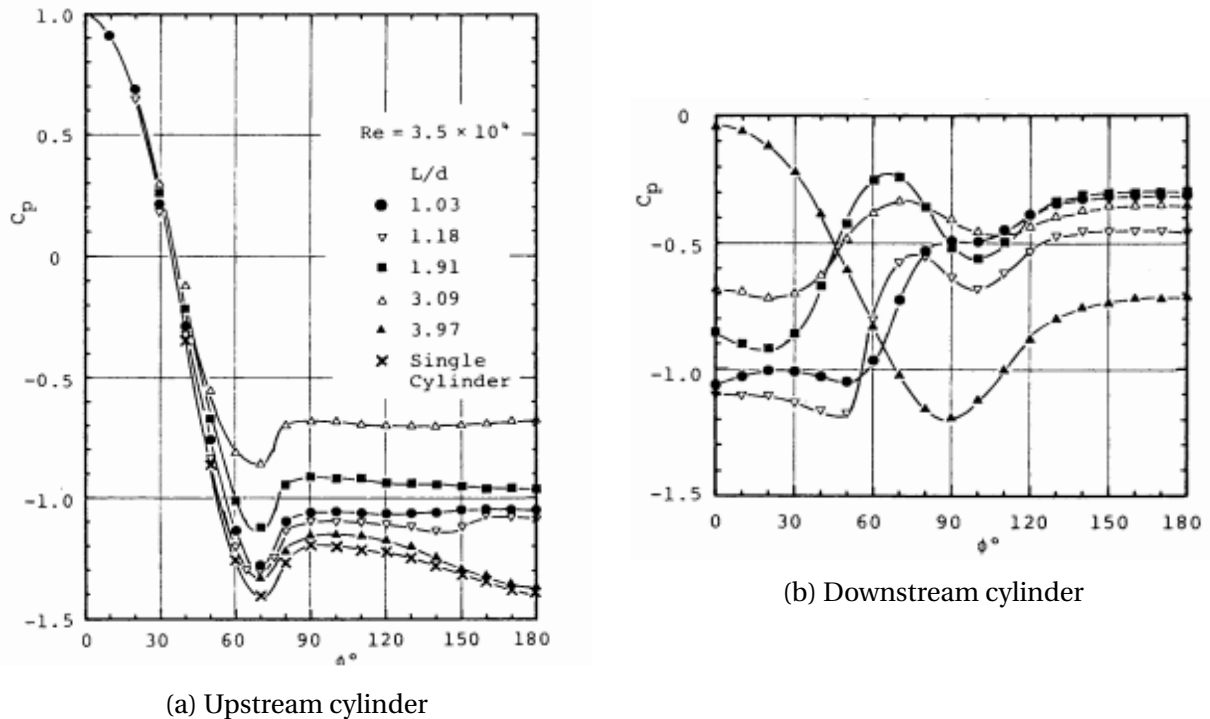


Figure 2.10: Pressure distribution around tandem cylinders. Figures taken from [Igarashi \(1981\)](#).

In figure 2.10a we can clearly see the C_p characteristics listed above. In the stagnation point (at 0 degrees) there is a positive pressure coefficient. After this point we see a favorable pressure gradient. The pressure gradient switches sign at about 70 degrees and we get an adverse pressure gradient. For small spacings the base pressure coefficient for the upstream cylinder shows a rather flat curve. The base pressures are almost the same as the gap pressure coefficients of the downstream cylinder shown in figure 2.10b, which indicates quasi-stationary vortices in the gap region, ([Igarashi, 1981](#)). The spacing $S/D = 3.97$ is larger than the critical spacing for this Reynolds number, and the pressure distribution of the upstream cylinder shows a profile similar to the one of a single cylinder. The separated shear layers now roll up in front of the downstream cylinder.

The C_p characteristics of the downstream cylinder can be recognized in figure 2.10b. For spacings up to the critical spacing, the pressure coefficient has a negative value in the gap and maximas at the reattachment and separation points. For the smallest spacing there is no reattachment peak and the two cylinders thus act as a single body where the shear layers from the upstream cylinder wrap around the downstream one without reattaching. For the largest spacing, the pressure distribution shows a similar profile as for a single cylinder with turbulent separation, ([Igarashi, 1981](#)). This is coherent with vortices shed from the upstream cylinder impinging the downstream cylinder, creating a more turbulent flow.

Figure 2.11 shows the pressure fluctuations around tandem cylinders for the same Reynolds number and spacing range as figure 2.10. The figure is taken from the same research.

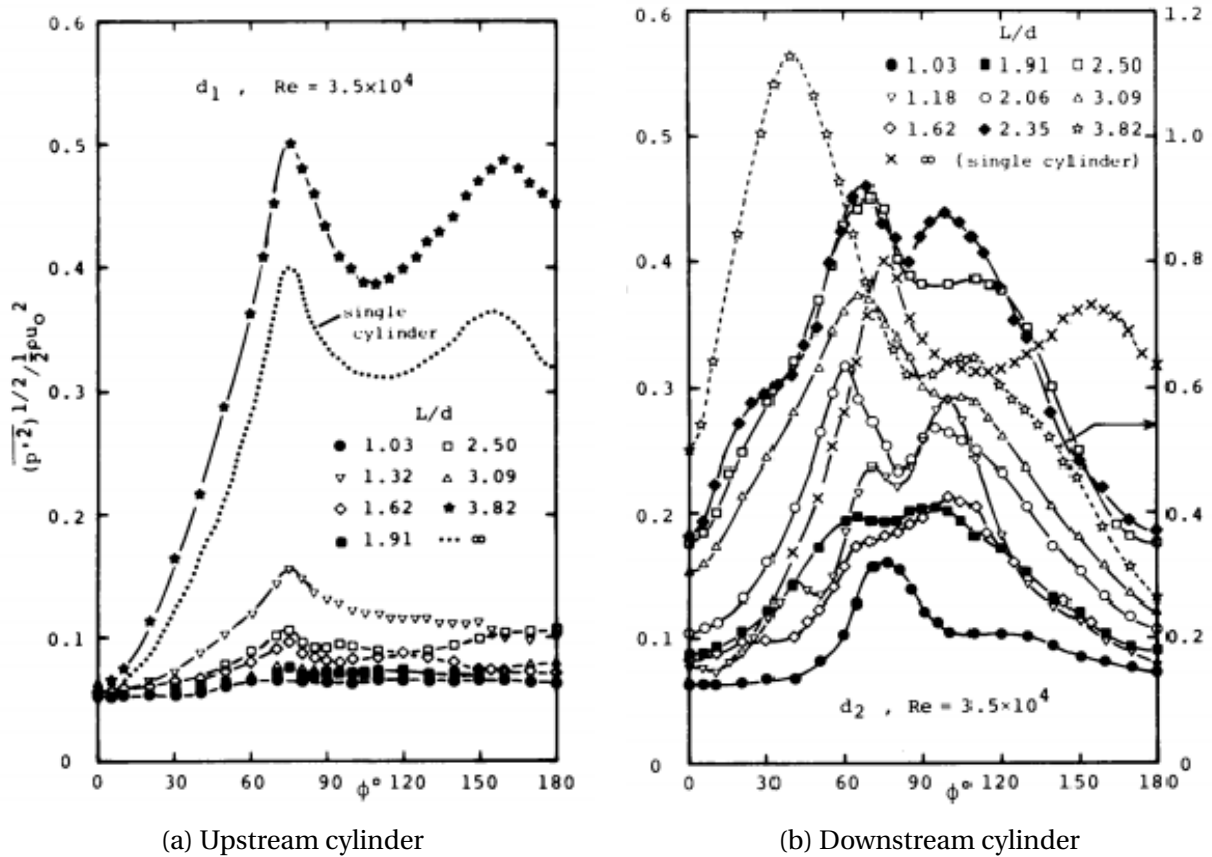


Figure 2.11: Pressure fluctuations around tandem cylinders. Figures taken from [Igarashi \(1981\)](#).

In figure 2.11a, the peaks in the RMS are located at the separation point. For spacings up to the critical spacing, these values are small, ([Igarashi, 1981](#)). Beyond the critical spacing, the profile is similar to the one of a single cylinder but the magnitude of the maximas are larger. The second maxima at this curve is due to the vortex formation which happens after the separation point. The reversed flow of the separated shear layer reattaches onto the rear part of the cylinder and separates again at the position of the second peak in the RMS profile.

The RMS distributions along the downstream cylinder show more chaotic profiles. For spacings up to the critical spacing and larger than the spacings of single body behaviour, there are two peaks in the RMS profiles. One is for the reattachment point and the other is for the separation point. The increase in RMS at the front part of the downstream cylinder with increased spacings shows that the fluid flow is more active in the gap as the spacing increases. The largest value of the RMS is seen for the spacing greater than the critical spacing. Here, the downstream cylinder sees a chaotic inflow. For the smallest spacing there is only one peak in the RMS profile and this is the separation peak, due to the two cylinders acting as a single body.

2.2.4 Strouhal number

[Xu and Zhou \(2004\)](#) did extensive research on Strouhal numbers in the wake of tandem cylinders with spacings of $1 < S/D < 15$ and Reynolds numbers of $800 < Re < 4.2 \cdot 10^4$. Figure

2.12 shows how the Strouhal number vary with spacing and Reynolds number.

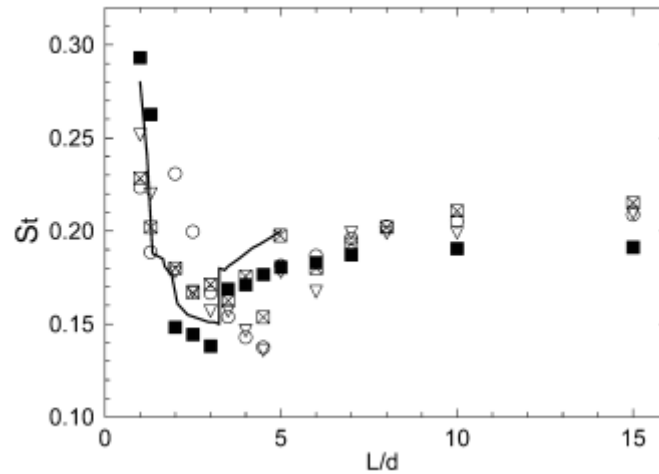


Figure 2.12: Strouhal number data for two tandem circular cylinders in cross-flow as a function of the spacing: ∇ , $Re = 1.2 \cdot 10^3$ (Xu and Zhou, 2004); \boxtimes , $Re = 2.9 \cdot 10^3$ (Xu and Zhou, 2004); \circ , $Re = 7 \cdot 10^3$ (Xu and Zhou, 2004); \blacksquare , $Re = 4.2 \cdot 10^4$ (Xu and Zhou, 2004); solid line, $Re = 2.2 \cdot 10^4$ (Igarashi, 1981). Figure taken from Xu and Zhou (2004).

For small spacings, when the cylinders act like a single body, the Strouhal number is initially larger than that of a single cylinder. It then decreases rapidly with increasing spacing, Sumner (2010). Zdravkovich (2003) explains this with the narrow wake the two cylinders create. At the critical spacing there is a discontinuous jump in the Strouhal number which corresponds to the change in flow pattern when vortices are shed in the gap. Just before the critical spacing is reached, Igarashi (1981) reported that two distinct Strouhal numbers can be identified. This is due to the bistable flow (flow pattern E in figure 2.9).

In the spacing region of $1.18 < S/D < 2.06$ Igarashi (1981) reported a large dependency on Reynolds number. This is clear in figure 2.12 as the discrepancies between the profiles for the different Re is larger.

In the co-shedding region for spacings larger than the critical spacing, the Strouhal number is the same for the upstream and the downstream cylinder, Xu and Zhou (2004).

2.2.5 Three-dimensionality

Three-dimensionality is especially important for turbulent flows, as the flow is more disturbed and rotational. As mentioned in chapter 1.1, the early numerical simulations of flow was done in 2D. This due to the lack of data power and memory. For tandem cylinders, the 2D simulations modeled the flow picture in a satisfying way, but there were large errors in the forces and Strouhal numbers obtained from the simulations, (Papaioannou et al., 2006). It was found by Papaioannou et al. (2006) that 2D simulations over-predicts the C_D of the upstream cylinder while under-predicting that of the downstream cylinder. It was concluded that this was due to the vortices in the 2D simulations were stronger than those of the 3D simulation.

According to [Faltinsen \(1990\)](#), for a 3D cylinder we speak of correlation length. This is a part of the cylinder where the hydrodynamic forces have the same phase, i.e. the lift force has the same phase along a length and the drag force have the same phase along a length. Because the change in phase of the lift-, and drag-force changes along the span of the cylinder, there is a reduction in the total lift-, and drag force on the 3D cylinder compared to a 2D cylinder. This is due to a cancellation effect due to the unsynchronized shedding from the different correlation lengths. The vorticity picture in 3D is very complicated and the effects of the vortices in different directions interacting with each other is reflected in the forces. Figure 2.13 shows the correlation length for a circular cylinder with respect to Reynolds number. The decrease in correlation length for turbulent flows with $Re > 10^5$ is due to the disorganized flow at this Reynolds number. It is thus more difficult to maintain the same phase of the forces over a long span of the cylinder.

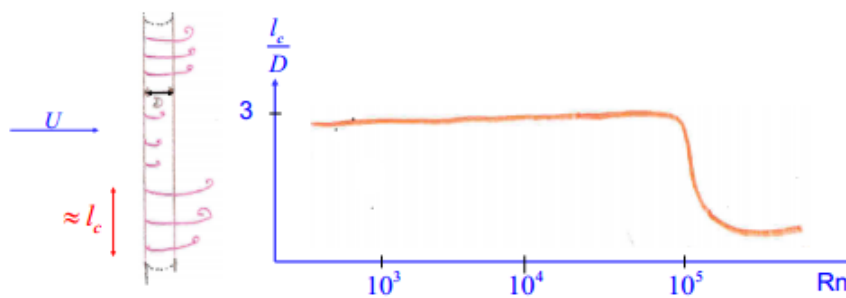


Figure 2.13: Correlation length for a circular cylinder with respect to Reynolds number. Figure taken from [Greco \(2013\)](#).

[Wu et al. \(1994\)](#) examined the flow field in the wake of circular cylinders in tandem arrangement and focused on the spanwise coherence of the velocity field. It was found that in the reattachment regime, the correlation length for the downstream cylinder was longer than that of a single cylinder. In this regime there are no vortices behind the upstream cylinder. In the co-shedding regime the opposite effect was discovered. Now, the correlation length was smaller than that of a single cylinder. It was concluded that the vortex impingement on the downstream cylinder enforced the turbulence in the flow and thus caused the correlation length to be smaller.

It is clear that for a 3D simulation, a cylinder length of $4D$ is enough to capture the 3D effects. This was also stated by [Papaioannou et al. \(2006\)](#).

2.3 OpenFOAM

OpenFOAM is an open source CFD software package that comes with a series of different solvers. It can thus be applied for many different engineering problems, including incompressible flow as used in this work. Since it is an open source program, all codes are available for the user to inspect and manipulate for individual use. Some basic tutorials can be found on the OpenFOAM web site, but there is no detailed description of the program. However, there are places to look for understanding regarding how the program works. The OpenFOAM programmers guide ([Foundation, 2013](#)) found in the program files explains which

methods OpenFOAM uses for solving the equations. In addition to this, there are numerous forums on the internet where the use of the program is discussed.

OpenFOAM uses the finite volume method to solve partial differential equations (PDEs). This method expresses the conservation of one or more quantities by discretization. The elements in the mesh used for the simulations act like many control volumes which the PDEs are integrated over. These integrations result in balance equations which are discretized with respect to some unknowns ([Eymard et al., 2010](#)). The solution is defined in the cell centers. The numerical method of OpenFoam will be described further in chapter 3.

Chapter 3

Numerical solver methods in OpenFOAM

As mentioned earlier, a CFD software relies on numerical modeling. The problem that is going to be solved is often described by partial differential equations (PDEs). When we look at a circular cylinder in a fluid, these equations are the Navier-Stokes equations. To be able to solve these equations the program needs to discretize them. This means that approximate algebraic relations that represent the PDEs are derived. Since the algebraic equations are only approximations, we get a residual, an error. The user can define the residual to be as small as the user finds satisfactory. There are various ways of doing this discretization. OpenFOAM uses the finite volume method. This method is explained in section 3.2. To be able to solve the equations, a mesh has to be generated. The governing equations is then discretized over this mesh. When the flow is turbulent, a turbulence model needs to be applied. The large eddy simulation model used in this work is presented in section 3.5.

OpenFOAM has numerous solvers and algorithms and the user specify in the system case folder which ones that are going to be used. To explain all of these different solvers will be far too extensive for the scope of this work and thus, only the applications used in this work will be presented. The equations and explanations used in this chapter is mainly based on theory from [Versteeg and Malalasekera \(1995\)](#) and [Ferziger and Peric \(2002\)](#).

3.1 Governing equations of fluid flow

In this section the governing equations of fluid motions are described by the conservation laws. These laws include conservation of mass and conservation of momentum, and together they make a basis for the description of fluid flow. The integral form of these equations over a given control volume will be explained.

3.1.1 Mass conservation - the continuity equation

The mass conservation is based on the fact that no mass should disappear or be added inside the element. It is just a way of setting up an equation that explains that the mass that flows into an element should also flow out of it. Terms considered are the rate of increase of mass inside the element and the net rate of flow of mass across the element boundaries. On integral form this becomes:

$$\frac{\partial}{\partial t} \int_{\Omega} \rho d\Omega + \int_S \rho \mathbf{U} \cdot \mathbf{n} dS = 0 \quad (3.1)$$

Here, Ω is the entire fluid domain and S is the surface of the domain.

Since ρ is constant over the entire domain for an incompressible fluid, $\frac{\partial \rho}{\partial t} = 0$ and the mass conservation equation becomes:

$$\int_S \rho \mathbf{U} \cdot \mathbf{n} dS = 0 \quad (3.2)$$

It means that the net flux over the element surface is equal to zero at all times. The mass conservation equation is also called the continuity equation.

3.1.2 Momentum conservation

This law is based on Newton's second law where the energy added to the fluid particle equals the sum of the forces acting on it. There are two types of forces acting on a fluid particle. These are surface forces and body forces. Surface forces are pressure forces and viscous forces while body forces can be gravity force, centrifugal force, Coriolis force and electromagnetic force. Normally the surface forces are given in a separate term in the conservation equation and the body force effects are represented by source terms. The integral form of the conservation equation is:

$$\frac{\partial}{\partial t} \int_{\Omega} \rho \mathbf{U} d\Omega + \int_S \rho \mathbf{U} \mathbf{U} \cdot \mathbf{n} dS = \int_S \Gamma \nabla \mathbf{U} \cdot \mathbf{n} dS + \int_{\Omega} P d\Omega \quad (3.3)$$

Where P is the source term. The equation also includes a diffusive term on the right hand side. On the left hand side there is a rate of change-term and a convective term.

The diffusive term can be written as:

$$-\left(p + \frac{2}{3}\mu \nabla \cdot \mathbf{U}\right) \mathbf{I} + 2\mu \mathbf{D} \quad (3.4)$$

where

$$\mathbf{D} = \frac{1}{2}(\nabla \mathbf{U} + (\nabla \mathbf{U})^T) \quad (3.5)$$

Since $\nabla \cdot \mathbf{U} = 0$ for incompressible flow, equation 3.4 can be written as:

$$\Gamma \nabla \mathbf{U} = -p \mathbf{I} + \mu(\nabla \mathbf{U} + (\nabla \mathbf{U})^T) \quad (3.6)$$

This expression for $\Gamma \nabla \cdot \mathbf{U}$ can now be put into equation 3.3. By also dividing the equation by ρ we get:

$$\frac{\partial}{\partial t} \int_{\Omega} \mathbf{U} d\Omega + \int_S \mathbf{U} \mathbf{U} \cdot \mathbf{n} dS = - \int_S \tilde{p} \mathbf{n} dS + \nu \int_S (\nabla \mathbf{U} + (\nabla \mathbf{U})^T) \cdot \mathbf{n} dS + \int_{\Omega} P d\Omega \quad (3.7)$$

\tilde{p} is the kinematic pressure: $\tilde{p} = \frac{p}{\rho}$. This equation can be recognized as an integral version of equation 2.9.

These integral forms of equations are used by OpenFOAM and are integrated over the elements and discretized.

3.2 The Finite Volume Method

The finite volume method is a discretization technique used in OpenFOAM. The basis for this method is the mesh of the computational domain. The mesh consists of many cells. In this project hexahedronal elements are used. These consists of eight nodes, one in each corner. Lines are drawn between each node and four lines makes up one face. Figure 3.1 shows to neighbor hexahedronal cells with some parameters that are defined in the finite volume method.

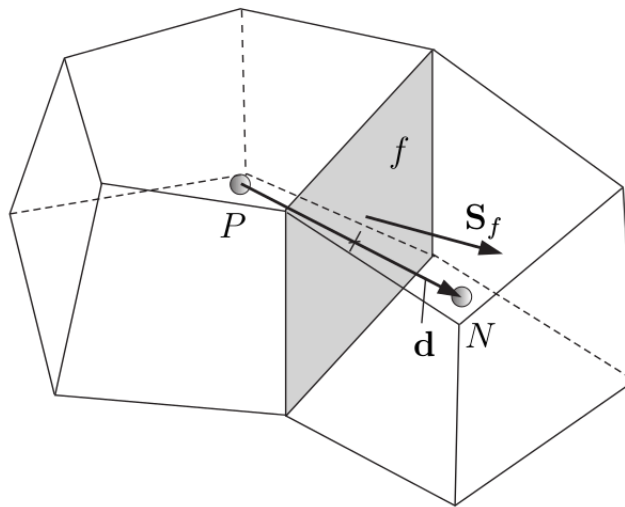


Figure 3.1: Neighbour cells with parameters used in the finite volume method. Figure taken from OpenFOAM Programmer's guide, (Foundation, 2013)

In this figure, P and N define the cell centers, d is the distance between the centers, f is the label for a surface and S_f is the surface normal vector.

Equation 3.7 is convection-diffusion equations including a source term. The pressure and velocities are coupled. These values thus have to be solved simultaneously.

The steady convection and diffusion problem of a property ϕ with a source can be written as:

$$\int_S \rho \phi \mathbf{u} \cdot \mathbf{n} dS = \int_S \Gamma \nabla \phi \cdot \mathbf{n} dS + \int_{\Omega} S_{\phi} dV \quad (3.8)$$

If a 1D-problem is considered, integration over an element will look like this:

$$(\rho u S \phi)_e - (\rho u S \phi)_w = \left(\Gamma S \frac{\partial \phi}{\partial x} \right)_e - \left(\Gamma S \frac{\partial \phi}{\partial x} \right)_w + \bar{S} V_R \quad (3.9)$$

Here, subscript w defines the left element border, subscript e is the right element border, Γ is a diffusion coefficient, $\bar{S} V_R$ is the mean value of the source term over the element and V_R is the volume of the element.

To get the discretized equations for the problem, the terms in equation 3.9 must be approximated. Two variables, F and D, which represent the convective flux per unit area and diffusion conductance respectively, are defined as:

$$F = \rho u \quad (3.10)$$

$$D = \frac{\Gamma}{\Delta x} \quad (3.11)$$

The integrated equation 3.9 can now be written as:

$$F_e \phi_e - F_w \phi_w = D_e (\phi_E - \phi_R) - D_w (\phi_R - \phi_W) + S_u + S_r \phi_R \quad (3.12)$$

And from the continuity equation it follows that:

$$F_e - F_w = 0 \quad (3.13)$$

The velocity is assumed to be known. To solve the equation ϕ needs to be discretized at the cell faces.

OpenFOAM solves all the flow variables at the cell center value. We thus have one value per cell and this value represents the average of the values in this cell. This could lead to problems when the pressure and velocity terms are coupled. For example if the pressure values in every second cell is the same (the checker board pressure field), the pressure gradient approximated by linear interpolation in the center of one cell would be zero. To account for this, the volume fields have a boundary field. This is a new variable that saves the velocity values at the faces.

Between the cell centers the value of the parameters can be found in many different ways. OpenFOAM has a wide range of schemes that can be used. As mentioned it will be too extensive to go into all these different schemes, but the one that is used in the analyses done in this work will be presented. This is the Gauss linear scheme. Here, linear interpolation is used to find the values between two elements.

3.3 Linear interpolation

This type of interpolation method uses the values in two cell centers to find the value at the surface between them.

$$\phi_e = \frac{1}{2}(\phi_R + \phi_E) \quad (3.14)$$

$$\phi_w = \frac{1}{2}(\phi_W + \phi_R) \quad (3.15)$$

Substituting this into 3.12 for a uniform grid gives:

$$[(D_w + \frac{F_w}{2}) + (D_e - \frac{F_e}{2}) + (F_e - F_w) - S_r]\phi_R = (D_w + \frac{F_w}{2})\phi_W + (D_e - \frac{F_e}{2})\phi_E + S_u \quad (3.16)$$

or

$$a_R\phi_R = a_W\phi_W + a_E\phi_E \quad (3.17)$$

3.4 Solution algorithm PISO for pressure-velocity coupling

As mentioned earlier, it was assumed that the velocity field was known in the convection of the variable ϕ . In general this is not the case. The velocity field is found as a part of the solution process. As we know, the Navier-Stokes equation has non-linear terms and all the parameters are coupled. The hardest parameter to find is the pressure. It appears in both momentum equations but there are no equation describing the pressure.

The problems with the equations are normally solved by an iterative solution method. There are different methods for finding the entire flow field. In the simulations done in this work, the PISO (Pressure Implicit with Splitting of Operators) solver has been used.

The PISO algorithm is a pressure-velocity calculation procedure. It involves one predictor step and two corrector steps.

In the predictor step, the pressure field is guessed as p^* . This pressure fields give velocity components u^* and v^* . But unless p^* is correct, the velocity fields u^* and v^* will not satisfy the continuity equation.

The first corrector step then gives new velocity fields (u^{**} and v^{**}) which satisfy the discretized continuity equation. The equations for the corrected values of u and v will not be given here, but they are substituted into the discretized continuity equation which yields the pressure correction (p') equation. This is then used to find the velocity components u^{**} and v^{**} .

In the second corrector step, a twice-corrected velocity field is found by solving the momentum equations again. A new pressure correction equation is defined such that

$$p^{***} = p^{**} + p'' = p^* + p' + p'' \quad (3.18)$$

where p'' is the second pressure correction. The twice-corrected velocity field is substituted into the discretized continuity equation and this results in the pressure correction equation. This equation is solved to find p'' and then the twice-corrected pressure, p^{***} .

This process is done iterative, such that it is repeated until convergence.

3.5 Turbulence modeling and LES

A turbulent flow is characterized by randomness of transport variables with respect to time and space, mixing and a wide range of length- and time scales. The basic entities of a turbulent flow are rotating masses called eddies. The eddies are of different sizes. The largest eddies extract kinetic energy from the mean flow due to the instabilities in the flow. The energy will transfer from the large eddies to the smaller eddies where it is mopped up due to viscous dissipation. There is a large range of eddy sizes and the difference between the largest and the smallest eddies is quite large. Based on the Kolmogorov length scale, the ratio between the largest and the smallest eddies are related to the Reynolds number in the following way:

$$\frac{\eta}{l} \sim Re^{-\frac{3}{4}} \quad (3.19)$$

η is the length of the smallest eddies and l is the length of the largest eddies. Thus, as the Reynolds number gets bigger, the difference in sizes gets bigger. All of the length scales needs to be captured while modeling the turbulent flow to get the entire physics of the flow. This is very challenging in numerical simulation. There is a randomness in turbulent flow and the instantaneous velocity of the flow can be described as $u = \bar{u} + u'$ where \bar{u} is the mean component of the velocity and u' is the fluctuating component. Modeling the turbulence can be done in different ways.

At this time, Reynolds Averaged Navier-Stokes (RANS) is the most commonly used turbulence model in numerical simulation. In RANS modeling, the flow variables are split into a mean (time averaged) part and a turbulence (fluctuating) part. The fluctuating part of the variable is modeled with a turbulence model. An example of a turbulence model is the $k - \epsilon$ model. If the turbulent part is very large, RANS is not a suitable model to use. Examples of flows where this is the case are wake flows and flows with large separation, such as flow around bluff bodies. The RANS-model will not be further discussed in this work.

A turbulence model more suitable for bluff-body flow is the Large Eddy Simulation (LES) model. In LES, the large scale eddies are solved by the discretized equations, while the smaller eddies are modeled. In turbulent flows at high Reynolds number, the smaller eddies are nearly isotropic and behave in a general way. The larger eddies, which extract kinetic energy from the flow, are anisotropic and their behavior is dependent on boundary conditions, geometry of the domain and body forces. It is the large eddies that makes turbulence modeling tricky, and this problem is avoided in LES. The drawback of using LES is that it requires that the mesh close to surfaces is very fine. This results in a very small time step and thus very long computational time and the requirement of large computer memory and power.

To separate the large eddies from the smaller ones, LES uses a spatial filtering operation. A cutoff length is chosen and the eddies that are longer than this cutoff length will be resolved in the flow computation. In CFD computations with the finite volume method, only one value of each flow parameter is retained in each grid cell. The cutoff length is thus chosen to be the same as the grid length because finer details are lost anyways due to them not being captured by the grid. The eddies smaller than the cutoff length are filtered out together with the effect these will have on the larger eddies. This effect needs to be accounted for and this is done by a subgrid scale model.

On the filtered form, the incompressible continuity and momentum equations (3.2 and 2.9) becomes (Versteeg and Malalasekera, 1995):

$$\frac{\partial \bar{u}_i}{\partial x_i} = 0 \quad (3.20)$$

$$\frac{\partial \bar{u}_i}{\partial t} + \frac{\partial \bar{u}_i \bar{u}_j}{\partial x_j} = -\frac{1}{\rho} \frac{\partial \bar{p}}{\partial x_i} + \mu \frac{\partial^2 \bar{u}_i}{\partial x_j^2} - \frac{\partial \tau_{ij}}{\partial x_j} \quad (3.21)$$

The overbar indicates a filtered flow variable which is space-filtered and not a time averaged parameter as it does in the RANS method. $i, j = 1, 2, 3$ and refers to the velocity component in the streamwise (x), crossflow (y) and spanwise (z) flow direction and x_i represents the respective directions. The last term, τ_{ij} , is a set of stresses caused by the filtering operation and is given as (Versteeg and Malalasekera, 1995):

$$\tau_{ij} = \overline{u_i u_j} - \bar{u}_i \bar{u}_j \quad (3.22)$$

Since a big portion of these terms accounts for the convective momentum transport due to interactions between the unresolved subgrid scale eddies, they are often called subgrid scale stresses. The subgrid scale stresses must be modeled. There are several subgrid scale models, but the one used in this work is the Smagorinsky model. This model, (Prsic et al., 2014), assumes that the turbulent stresses behave in the same way as the large scale strain rate tensor, S_{ij} :

$$\tau_{ij} - \frac{1}{3} \delta_{ij} \tau_{kk} = -2\nu_t \bar{S}_{ij} \quad (3.23)$$

ν_t is the subgrid-scale eddy viscosity and δ_{ij} is the Kronecker delta. In the resolved field, the strain rate tensor can be written as:

$$\bar{S}_{ij} = \frac{1}{2} \left(\frac{\partial \bar{u}_i}{\partial x_j} + \frac{\partial \bar{u}_j}{\partial x_i} \right) \quad (3.24)$$

ν_t is a function of the strain rate tensor and the subgrid-scale length, l :

$$\nu_t = l^2 |\bar{S}_{ij}| \quad (3.25)$$

$$|\bar{S}_{ij}| = \sqrt{2 \bar{S}_{ij} \bar{S}_{ij}} \quad (3.26)$$

The subgrid-scale length is given as:

$$l = C_s \bar{\Delta} \quad (3.27)$$

where Δ is the cutoff length. C_s is the Smagorinsky constant and in this work it has a constant value of 0.2.

Chapter 4

Numerical setup

All CFD codes contain three elements, or stages. These main elements are the pre-processor, the solver and the post-processor, (Versteeg and Malalasekera, 1995). These elements can also be considered as stages in the simulation process. In the pre-processing stage, the geometry of the computational domain is defined and a mesh is generated. The correct governing equations are chosen to solve the physical problem and appropriate boundary conditions are specified. The pre-processing stage is crucial for the entire computation. The user has to have enough knowledge to make the right decisions in this stage. The solver stage is done entirely by the software. The user has to specify which kind of solver method is going to be used. The post-processing stage is where results are taken out and presented in various ways.

In the previous chapter some numerical methods and governing equations in OpenFOAM were presented. In this chapter the schemes used in this work will be further specified and described. The chapter is organized as follows: In section 4.1 the computational domain and grid are presented followed by a description of the boundary conditions in section 4.2. A verification of the computational grid is conducted in section 4.3. The specifications of the solver method is presented in section 4.4 and in section 4.5 some tools used for visualization will be described such that it is clear how the results are obtained and thus easier to compare results to other work in a correct way.

Since this work is inspired by the previous work by [Abrahamsen-Prsic \(2015\)](#) and [Prsic et al. \(2014\)](#), the boundary conditions and mesh used in the simulations are the same as used in the mentioned work. The aspects of the mesh, boundary conditions and post-processing tools will still be described here, with references to the above mentioned research.

4.1 Computational domain and grid

This section describes the geometry of the computational domain and how it is represented by a grid. The choice of domain size is an essential part of the analysis. It is important that the domain is large enough to capture all the effects of the flow around the cylinders. If it is too small, the boundaries could have an unwanted effect on the flow parameters in the domain. The grid generation is a widely discussed aspect. It is not yet a standard for generating satisfying meshes and whole books are written on the topic. The grid has to be small enough

to capture the flow variations in the entire domain. Close to the cylinders and other places in the domain that could be subjected to large and detailed variations in the flow, the grid has to be very fine. It is easy to think that if the entire domain is divided into infinitely many fine cells, the solution would be perfect. But to this day the computer capacity is not large enough to make this possible. A compromise must be made by distributing the cells in a way that lets the most important locations in the domain have a finer mesh.

4.1.1 Domain

A 2D, non-scaled version of the computational domain used in this work is shown in figure 4.2. In reality the domain is a 3D rectangular shape. The domain extends from $10D$ in front of the upstream cylinder center to $27D$ behind the downstream cylinder. The cylinders both have diameters of $D = 1$ meter. The height of the domain in the y -direction is $20D$ where the top and bottom of the domain are boundaries that shall represent an infinite fluid domain. The inflow at the left boundary (flow is from left to right) is a uniform flow in x -direction of magnitude U that represent a Reynolds number of 13100. The length of the domain in the spanwise z -direction is $4D$, which is sufficient to capture the 3D effects of the flow. The spacing between the cylinder centers is $5D$. The domain dimensions were based on the research on flow around tandem cylinders in the vicinity of a wall with incoming flow of Reynolds number 13100 by [Abrahamsen-Prsic \(2015\)](#) which again was based on the experience from the research by [Prsic et al. \(2014\)](#). It was concluded that the domain was big enough since other research had obtained satisfying results with smaller domains with higher Reynolds number.

The spanwise length of the domain was proven to be sufficient to capture the three-dimensionality of the flow by [Prsic et al. \(2014\)](#) that simulated a single cylinder in an incoming flow with the same Reynolds number.

By using the same dimensions as [Abrahamsen-Prsic \(2015\)](#), comparison of the results with this research will be independent of effects of domain size.

4.1.2 Grid

The domain is discretized in a structured multiblock grid with of a body fitted O-mesh around the cylinders and H-mesh in the outer parts of the domain. The mesh consists of hexahedral elements. The O-mesh is divided into different zones such that is possible to easily control the element size throughout the domain. The mesh closest to the cylinder and in the gap should be very fine while the outer parts of the domain should have a coarser mesh.

When applying a structured grid care has to be taken to obtain elements that are not highly skewed or distorted. These are problems that are avoided in an unstructured grid, but for simple geometries like circular cylinders, structured meshes with hexahedral cells is normally used. In this mesh, attention is paid to the transition of cell size between the zones. It is important to have a gradual transition of the size to avoid numerical instabilities.

Figure 4.1 shows some aspects of the grid. Figure 4.1 (a) shows the entire discretized domain with its different blocks. The grid consists of 14.3 million cells. Closest to the cylinders there is a small O-mesh of width $0.2D$ that provides good control of the cell size closest to the

cylinders. A second elliptic O-mesh of height $5D$ is extended around both cylinders. This region represent a transition from the very fine mesh in the closest vicinity of the cylinder to the coarser mesh in the outer parts of the domain. In the gap between the cylinders another O-mesh is used with a very fine resolution to capture the details of the complex flow in this region. The other parts of the domain, respectively the top, bottom and front of the domain and the far wake region, is discretized with relatively coarse H-grids. The most critical parts of the domain are the gap region and close to the cylinder surfaces. These areas have to be represented by a fine mesh to capture all the changes in the flow. The mesh is highly graded at the inner O-mesh and slightly graded in the outer bocks. Figure 4.1 (b) shows details of the mesh in the region close to one of the cylinders and the gap. The cells closest to the cylidner surface is 0.1733% of the cylinder diameter and there are 254 elements distributed along the cylinder circumference. The meshes around the two cylinders are identical. The number of elements in the spanwise z -direction is 95. The origin of the domain is placed in $x = y = z = 0$, which is in the center of the upstream cylinder.

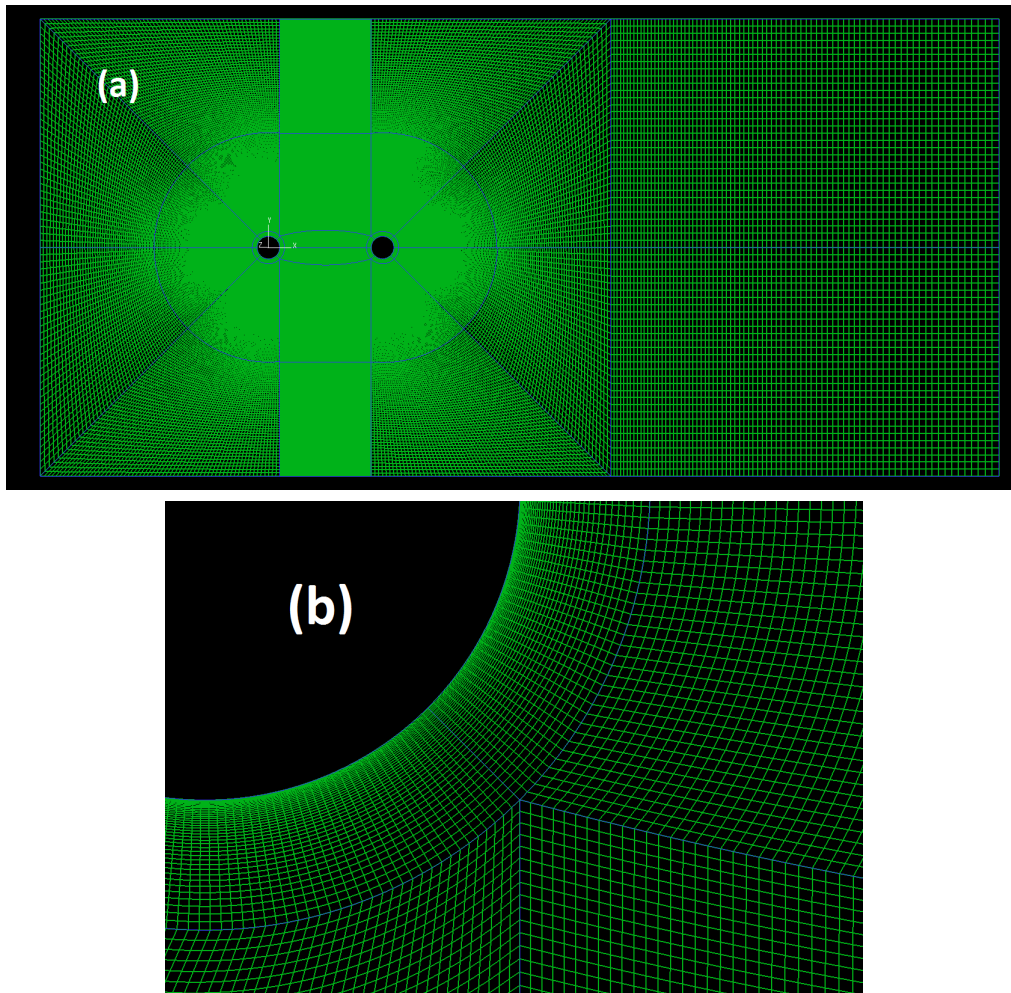


Figure 4.1: (a): 2D slice of the mesh in the x - y -plane showing blocks and element refinement. (b): close-up showing mesh details in the O-grid around the cylinders.

4.2 Boundary and initial conditions

Theoretically, it is desired that the computational domain is infinitely large such that no effect of the boundaries on the solution of the flow parameters. This is not possible in practice. To make the simulations as cheap and efficient as possible it is need for a small domain with few elements. The boundary conditions implied on the boundaries are thus essential for the solution. The boundaries must be defined such that they in a best possible way will represent an infinite domain.

Figure 4.2 shows a 2D slice of the computational domain with its boundary conditions and parameters. The velocity is given as a vector, $U = (u, v, w)$. At the inlet, the velocity vector is given a fixed value of $U = (1.31, 0, 0)$. Physically this means that there is only flow in the x-direction. The pressure is a scalar and it has no specific direction. At the inlet the pressure is set as zero gradient. This means that the pressure does not change value in any direction. This means that there is no change in the pressure magnitude close to the inlet. This coincides with the requirement that there should be no drastic changes close to the inlet (or any other boundaries) such that the boundary will affect the flow parameters considerably.

At the outlet the pressure is set to a fixed value of 0, and the velocity vector has a zero gradient. The physical meaning of the fixed value zero of the pressure is that at the outlet pressure is equal to the pressure of the undisturbed fluid. This is a somewhat tricky boundary condition since the wake flow behind a bluff body is affected by vortices a very long distance from the body. The vortices dissipate and die out to some extent, but there is still irregularities in the flow. The assumption is thus that the outlet is so far away from the body that this boundary condition will have no effect on the flow parameters at the body. The boundary conditions are also listed in table 4.1 for readability.

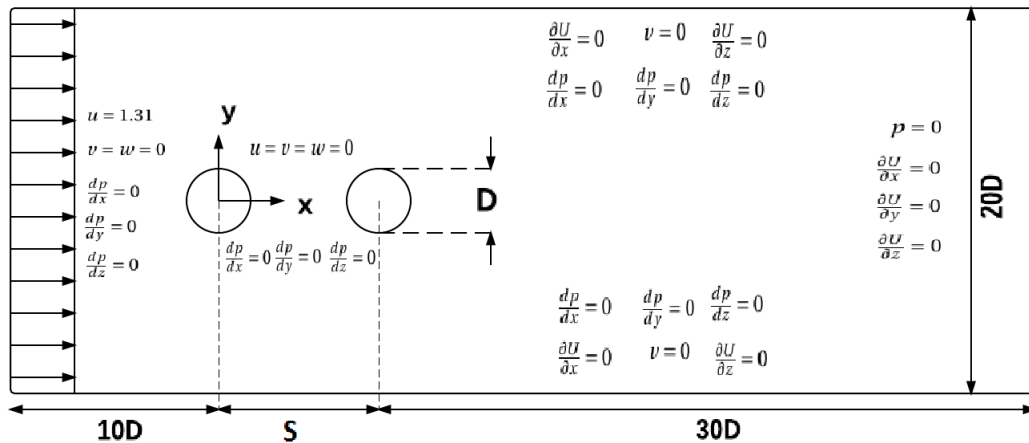


Figure 4.2: 2D slice of computational domain showing parameters and boundary conditions

The cylinders have a no-slip boundary condition. This means that all the velocity components are zero, which coincides with the no-slip phenomena of water particles at solid bodies. The pressure has a zero gradient boundary condition. This boundary condition is widely used in the literature for solid bodies and walls.

The top and bottom of the domain has a slip boundary condition. This boundary condition means that if the parameter is a scalar, it is set to zero gradient. If it is a vector, the

Table 4.1: Overview of boundary conditions for different patches

Patch	Velocity BC	Pressure BC
Top and Bottom	$\frac{\partial U}{\partial z} = 0, \frac{\partial U}{\partial x} = 0, v = 0$	$\frac{\partial p}{\partial x_i} = 0$
Inlet	$v = w = 0, u = 1.31$	$\frac{\partial p}{\partial x_i} = 0$
Outlet	$\frac{\partial U}{\partial x_i} = 0$	$p = 0$
Cylinders	$U = 0$	$\frac{\partial p}{\partial x_i} = 0$

normal components has a fixed value of zero while the tangential components have zero gradients. Physically it has the same meaning as the symmetry boundary condition used by [Abrahamsen-Prsic \(2015\)](#) and [Prsic et al. \(2014\)](#) and is the same boundary condition as used by [Sainte-Rose et al.](#) It represents no flow through the top and bottom of the domain by setting $v = 0$ while the x- and z-components of the velocity are free and fluid is thus allowed to flow along the boundaries. It is important that the boundaries are adequately far away from the cylinders such that the induced velocity in the y-direction is negligible.

The side boundaries of the domain, perpendicular to the cylinder axis, have periodic boundary conditions called cyclic. This boundary condition enables two patches to be physically connected. The patches are paired up with the patches on the opposite side of the domain. The cyclic boundary condition causes the flux of a flow parameter out of the patch domain to be equal to the flux into the patch domain. This is mirrored to the paired patch on the opposite side. This boundary condition has been successfully applied in previous work by for example [Kitagawa and Ohta \(2008\)](#), [Sainte-Rose et al.](#) and [Uzun and Hussaini \(2012\)](#).

The simulation was impulsively started, such that the initial condition of the flow was $u = 1.31$, $v = w = 0$ and $p = 0$. It should be mentioned that p in this context is the difference between the pressure at a certain point and the pressure in the infinite fluid, $p = p' - p_\infty$.

4.3 Grid verification

Since a grid convergence study is beyond the scope of this thesis work, an evaluation of the grid used is presented in this section. The grid used is developed by [Abrahamsen-Prsic \(2015\)](#), which again based the grid on the one used in [Prsic et al. \(2014\)](#). Grid convergence studies were performed in these above mentioned articles. The grid in this work was developed from the coarsest grid with 16.5 million cells from [Abrahamsen-Prsic \(2015\)](#) which gave good results.

When performing a grid convergence study, the convergence is often based on the values of C_D , \bar{C}_D , C_L and St. What must be kept in mind is that these are parameters that are derived from the 'raw' data of the computation, namely the pressure, p , and the velocities, u , v , and w . The values of the derived parameters may suffer from manipulation errors. It is thus more interesting in a grid evaluation to look at the primary outputs from the computation.

One of the most crucial areas in a grid is the boundary layer. To get good results the boundary layer needs to be resolved with a lot of elements. There is no default for the number of elements there should be in the boundary layer other than 'enough'. Naturally, as previously mentioned, a LES simulation requires a more refined mesh, especially in the boundary layer,

to capture all the flow aspects here. A way to check whether there are enough elements in the boundary layer is to plot the velocity profile here. It is important to have a smooth profile such that the value of the velocity gradient is as correct as possible. Other parameters, such as vorticity, is calculated using the velocity gradient and it is thus important that the value is correct. In figure 4.3 the instantaneous velocity profiles at three locations on the cylinder is plotted together with the grid points.

The three locations represent velocity profiles of three very different shapes. The upper part of the boundary layer is clearly good enough resolved due to the small changes and tight spacing of grid points. To the right of the full velocity profiles a detailed plot of the inner part of the velocity profile is plotted. This region contains the most critical changes in values from grid point to grid point. In the figures to the right in figure 4.3 the straightness between the grid points can be seen. This is the effect that is unwanted when resolving the boundary layer. However, the form of the velocity profile is in all very smooth and details are preserved. It is thus concluded that the boundary layer mesh is sufficiently refined.

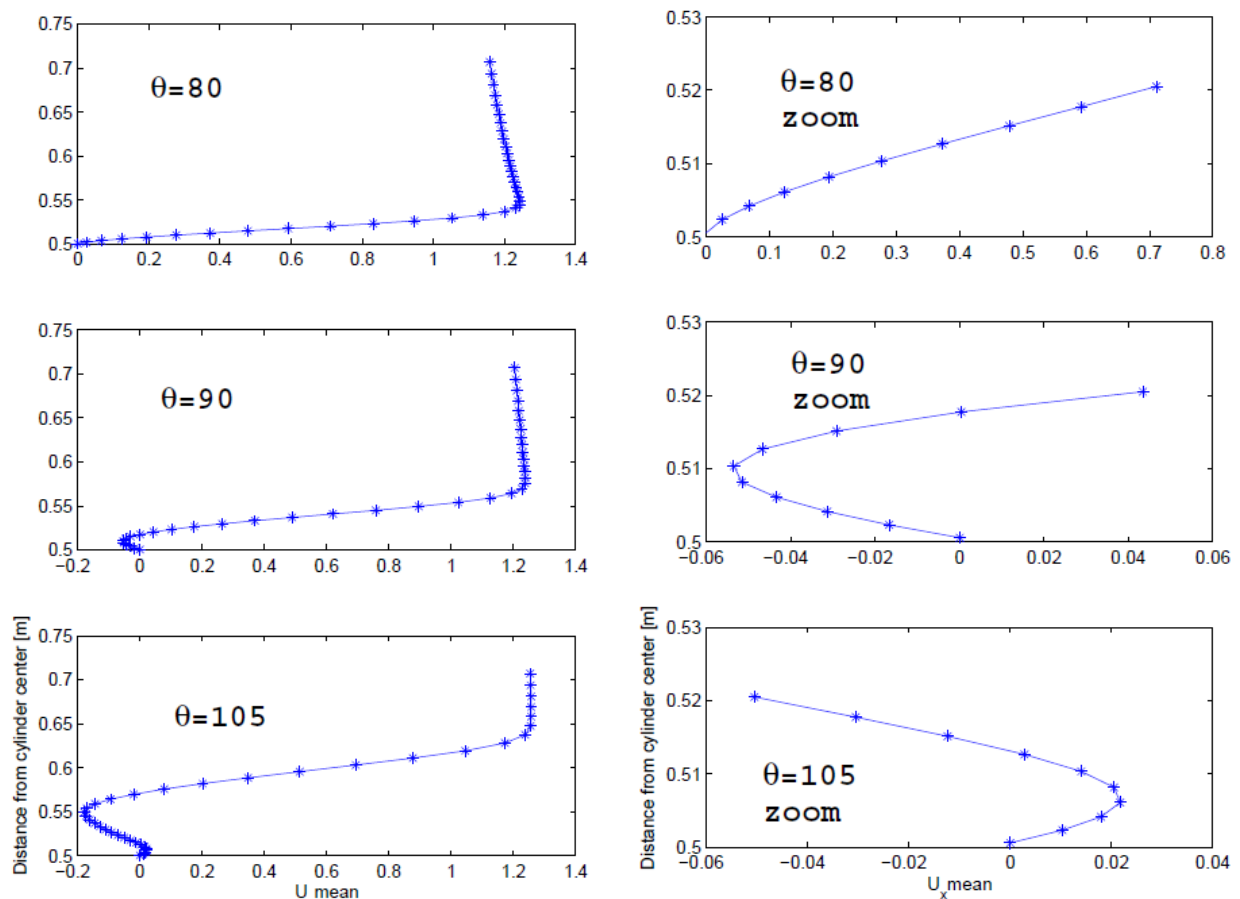


Figure 4.3: Plots of velocity profiles in the boundary layer for different radial locations together with the grid points. Details of the inner part of the velocity profiles are given in the corresponding right figures.

In a conventional grid convergence study numerous simulations are done with different meshing and time steps to be able to choose the grid and time step that gives an acceptable solution, that is when the solution converges. Since this study already have been performed in the mentioned research by [Abrahamsen-Prsic \(2015\)](#), and because it is very time consuming, a similar study have not been performed in this work. However, to in a similar

way confirm that the grid is satisfyingly refined, a simulation with half the amount of elements in x-direction in the gap has been performed. The rest of the grid is kept similar to the original one. Due to the sensitivity of the solution to mesh refinement in the gap region, doing simulations with coarser mesh here will be a good indicator whether the chosen mesh gives results within the converged range. Table 4.2 shows how the results varied with the two meshes.

Table 4.2: Results comparison of lift and drag coefficient of fine and coarse mesh

Case	#Elements [million]	\bar{C}_{D1}	\bar{C}_{D2}	C'_{L1}	C'_{L2}
Fine mesh	14.3	1.2	0.48	0.46	0.98
Coarse mesh	11.3	1.3	0.45	0.56	1.05

The results are quite similar to each other and both meshes gives results within the range that is represented in different research, (see table 5.2). This could show that both the grids gives converged results. [Abrahamsen-Prsic \(2015\)](#) reported that the results varied in a small scale between the finest meshes. Some small variations are thus accepted. This further shows that the fine grid of 11.3 million cells is safe beyond convergence. The averaging has been done over the same amount of vortex shedding periods as for the main simulation which is 30 periods. The similarity of the results indicate that the fine mesh give reliable results. However, the time history of the lift and drag coefficient of the coarse mesh differs in details from the ones of the fine mesh. These time histories can be seen in figure A.5 in appendix A.1. The time histories for the fine mesh are presented in section 5.4. There are thus some effect of the coarser mesh in the gap region.

4.4 Solver settings

The PISO-algorithm is described in chapter 3.4, however there can be many different settings to the solver. The tolerance for the iteration process is set to 10^{-6} for pressure, and 10^{-5} for velocity. This is defined in the fvSolution-script in the system-folder. The different scripts used in this work can be found in appendix B.

Equation discretization is the process of converting the PDEs into a set of algebraic equations that in matrix form can be given in vector form and integrated over the cell volumes and surfaces. There are many different functions available in OpenFOAM to discretise the terms in the PDEs. The chosen methods are given in the fvSchemes-script. In this work the Crank Nicolson method is used for time integration and the gradient terms are solved by Gauss linear and Gauss limited. All these schemes are of second order accuracy, ([Foundation, 2013](#)).

The subgrid scale model used is as presented in 3.5 the Smagorinsky model. [Lysenko et al. \(2012\)](#) did LES-simulations of flow around a smooth circular cylinder using a conventional Smagorinsky subgrid scale model and a dynamic k -equation eddy viscosity subgrid scale model. It was found that the dynamic subgrid scale model agreed best with results from other CFD simulations but both subgrid scale models agreed with experimental results. [Breuer \(1998\)](#) did LES simulations of flow with the same conditions as [Lysenko et al. \(2012\)](#) with subgrid scale models Smagorinsky and dynamic Smagorinsky as well as with no subgrid scale model. It was found that the solution changed little with respect to the subgrid

scale models used, but the results agreed most with experimental results when subgrid scale models were implemented. It is thus believed that a Smagorinsky subgrid scale model gives satisfying and reliable results for flow over a circular cylinder at high Reynolds numbers. It is thus believed that this can be implemented on tandem cylinders as well. The model is also used for simplicity when comparing results to [Abrahamsen-Prsic \(2015\)](#) and [Prsic et al. \(2014\)](#), since it is the same model used in this research.

4.5 Visualization

The visualization of the results is done in the program *ParaFoam* which is the main post-processor implemented in OpenFOAM. It is a wrapper for the third-party product *Paraview*. When using visualization tools, one have to be aware of that the tool itself manipulates the results obtained from the simulation. In ParaFoam, you can choose cell based or point based representation. The cell based representation assumes the value to be constant in the entire cell while the point representation interpolates the values in the points, and a smooth field is seen. It should be noted that ParaFoam gives the parameter values at the cell corners while OpenFOAM stores the value at the cell center. This is likely to cause some interference in the visualization.

This section presents the physics and mathematics behind some parameters that are visualized.

4.5.1 Vortex identification

One aspect of visualization that has been widely discussed and confused is the vortex identification. In their famous paper, [Jeong and Hussain \(1995\)](#) presented definitions that are used to visualize vortices. Two requirements for a vortex were given as (i) There must be a net circulation about the vortex core, and (ii) The geometry of the vortex should be a Galilean invariant, which means that they are in the same reference frame. In this section methods used in OpenFOAM and ParaFoam for vortex identification is briefly explained and visualized.

Vorticity

A way of identifying a vortex that has been used is the vorticity magnitude. Vorticity in 3D is given as, ([Cengel and Cimbala, 2010](#)):

$$\vec{\zeta} = \vec{\nabla} \times \vec{V} = \left(\frac{\partial w}{\partial y} - \frac{\partial v}{\partial z}\right)\vec{i} + \left(\frac{\partial u}{\partial z} - \frac{\partial w}{\partial x}\right)\vec{j} + \left(\frac{\partial v}{\partial x} - \frac{\partial u}{\partial y}\right)\vec{k} \quad (4.1)$$

It is described by a particle that has angular velocity and rotates about a point, the vortex core. The particles closest to the vortex core has the largest vorticity magnitude and it decays outwards. The higher velocity in the vortex core is also associated with a low pressure region.

Vorticity magnitude gives fairly good results in the free stream but causes troubles in shear flow, especially if the shear is comparable to the magnitude of vorticity. Such definition can thus not be used in a boundary layer.

Q-criterion and λ_2 -criterion

The Q-criterion and λ_2 -criterion is based on the velocity gradient tensor, $\nabla\mathbf{u}$, (Jeong and Hussain, 1995). The eigenvalues, σ , of $\nabla\mathbf{u}$ satisfies the equation:

$$\sigma^3 - P\sigma^2 + Q\sigma - R = 0 \quad (4.2)$$

P, Q, and R are three invariants of $\nabla\mathbf{u}$ where $P = 0$ for incompressible flow and

$$Q = \frac{1}{2}(u_{i,i}^2 - u_{i,j}u_{j,i}) = -\frac{1}{2}u_{i,j}u_{j,i} = \frac{1}{2}(\|\mathbf{\Omega}\|^2 - \|\mathbf{S}\|^2) \quad (4.3)$$

$$R = \det(u_{i,j}) \quad (4.4)$$

\mathbf{S} and $\mathbf{\Omega}$ are symmetric and antisymmetric components of $\nabla\mathbf{u}$.

The second invariant, Q, physically represents a balance between shear strain rate and vorticity magnitude at a certain point, (Jeong and Hussain, 1995). Imagine that the strain is what 'kills' a vortex by withholding the rotation. If $Q > 0$ the vorticity magnitude is larger than the shear strain and a vortex can thus appear. This is called the Q-criterion.

Another definition arises from considering the local pressure minimums from the gradient of the Navier-Stokes equations. By taking the symmetric part of this gradient it is given that, (Jeong and Hussain, 1995):

$$\frac{DS_{ij}}{Dt} - \nu S_{ij,kk} + \Omega_{ik}\Omega_{kj} + S_{ik}S_{kj} = \frac{1}{\rho}p_{,ij} \quad (4.5)$$

A local pressure minimum requires two positive eigenvalues of the tensor $p_{,ij}$. The two first terms in equation 4.5 represent unsteady irrotational straining and viscous effects, respectively, and are not considered when finding contributions to the pressure minimum. A vortex core is thus defined as a connected region with two negative eigenvalues of $\mathbf{S}^2 + \mathbf{\Omega}^2$, (Jeong and Hussain, 1995). $\mathbf{S}^2 + \mathbf{\Omega}^2$ is symmetric and has real eigenvalues $\lambda_1 > \lambda_2 > \lambda_3$, so the requirement that $\lambda_2 < 0$ will be the definition of a vortex core. This is known as the λ_2 -criterion.

It is not easy to understand from the definitions of the Q-criterion and λ_2 -criterion what the difference between them is. Jeong and Hussain (1995) claim that the λ_2 -criterion gives the best results of vortex visualization, though it is also concluded that the two criterion tend to be similar for different vortex structures. In reality, all cases are different and the Q-, and λ_2 -criterion it compared in figure A.2 and A.3 in appendix A.

When comparing figure A.2a with A.3a, and figure A.2b with A.3b it is clear that the lower values of λ_2 and Q shows more coherent structures than the higher values due to the lower threshold the vorticity magnitude has to overcome relative to the strain. Also, when comparing the iso-surfaces for λ_2 and Q it can be concluded that the differences between them are

negligible. Only some minor differences can be seen in figure A.2b and A.2a in the separation line. Here, λ_2 iso-surface seem to give a more detailed picture of the vorticity in the region, while the Q iso-surface looks more dense. In figure A.4, however, it is shown that vorticity iso-surface shows a lot more coherent structures for the same values as Q and λ_2 . All iso-surfaces are taken at the same time in the simulation.

4.5.2 Streamlines

Another way of visualizing results that needs to be explained is the streamlines. Cengel and Cimbala (2010) defines a streamline as a curve that is everywhere tangent to the instantaneous local velocity vector, which means that they indicate the fluid flow direction. Streamlines are often used to find separation points, especially on circular cylinders where this point is geometrically fixed. Streamlines are defined mathematically by, (Cengel and Cimbala, 2010):

$$\frac{dr}{V} = \frac{dx}{u} = \frac{dy}{v} = \frac{dz}{w} \quad (4.6)$$

A streamline cannot be seen in real life experiments but are often implemented by visualization programs to indicate flow direction. Streamlines must not be confused with pathlines and streaklines. A pathline draws out the actual path of a fluid particle in the flow and a streakline is the lines seen in experiments when smoke, dye or particles are injected into the flow. From these definitions it follows that the streamline is an instantaneous flow pattern at a given point in time while the other two are drawn up over time. However, if the flow is steady, the streamlines, pathlines and streaklines are identical. This is not the case in unsteady flow, which can change with time. Streamlines must thus be used with care, not trusted blindly. It only gives an instantaneous picture of what happens in the flow field. Streamlines of the mean velocity field is thus utilized as a more accurate use of streamlines.

ParaFoam uses an application called surfaceLIC to visualize streamlines. LIC means line integral convolution and the technique consists of convolving noise with a vector field and then producing a streaking pattern that follows the tangents of the vector field, (Organisation, 2015).

Chapter 5

Results

In this chapter the results obtained from the simulations are presented. As a summary, table 5.1 gives details of the computational grid as well as time step, Δt , of the simulation. The non-instantaneous results are taken over a period of approximately 30 vortex shedding periods. Recently it has been discussed whether this is a too short period to represent a correct sampling of the results. [Lysenko et al. \(2012\)](#) claimed that a simulation duration of 150 vortex shedding periods was satisfying in order to get a fully convergent mean flow field. The available time in this work was not sufficient to do such long simulations. However, the simulation duration in this work is the same as in [Abrahamsen-Prsic \(2015\)](#) and [Prsic et al. \(2014\)](#).

Table 5.1: Details of simulation

# Elements	14.3 million
#Elements on cylinder circumference	254
#Elements in boundary layer	40
Δt	0.0001
S/D	5
Re	13100

The results presented in this chapter comprises the vorticity distribution in section 5.1, showing vortex formation and separation from the upstream cylinder and the impingement on the downstream cylinder, wake flow in section 5.2 presented by velocity distributions in the wake and gap, mean- and RMS pressure distributions in section 5.3, drag-, and lift coefficients in section 5.4, Strouhal number in section 5.5 and separation presented by velocity streamlines in section 5.6.

5.1 Vorticity distribution

Figure 5.1 shows the vorticity distribution visualized by the Q-criterion at the middle of the cylinder axis, $z = 2$. The distribution shows how a vortex (A) shed from the upstream cylinder impinges the downstream cylinder and how a new vortex (B) is created on the downstream cylinder. When vortex A impinges the downstream cylinder, it deforms. This is seen in figure 5.1 b) and c). This makes the flow very unsteady and turbulent, and we get a very chaotic flow

picture around the downstream cylinder. Simultaneous to the impingement a new vortex, B, is formed at the same side on the downstream cylinder. This is most likely due to the "boost" it gets from the impingement. The two vortices merges to some degree and when a new vortex impinges the other side of the downstream cylinder, they are shed together. This is called synchronized vortex shedding. This, as well as the impingement is what causes the large forces on the downstream cylinder. This is further described in section [5.4](#)

The degree of merging of the two vortices depend on the strength of the vortices from the upstream and downstream cylinder and on the impingement angle, ([Kitagawa and Ohta, 2008](#)). In this instantaneous flow, the vortices does not merge fully.

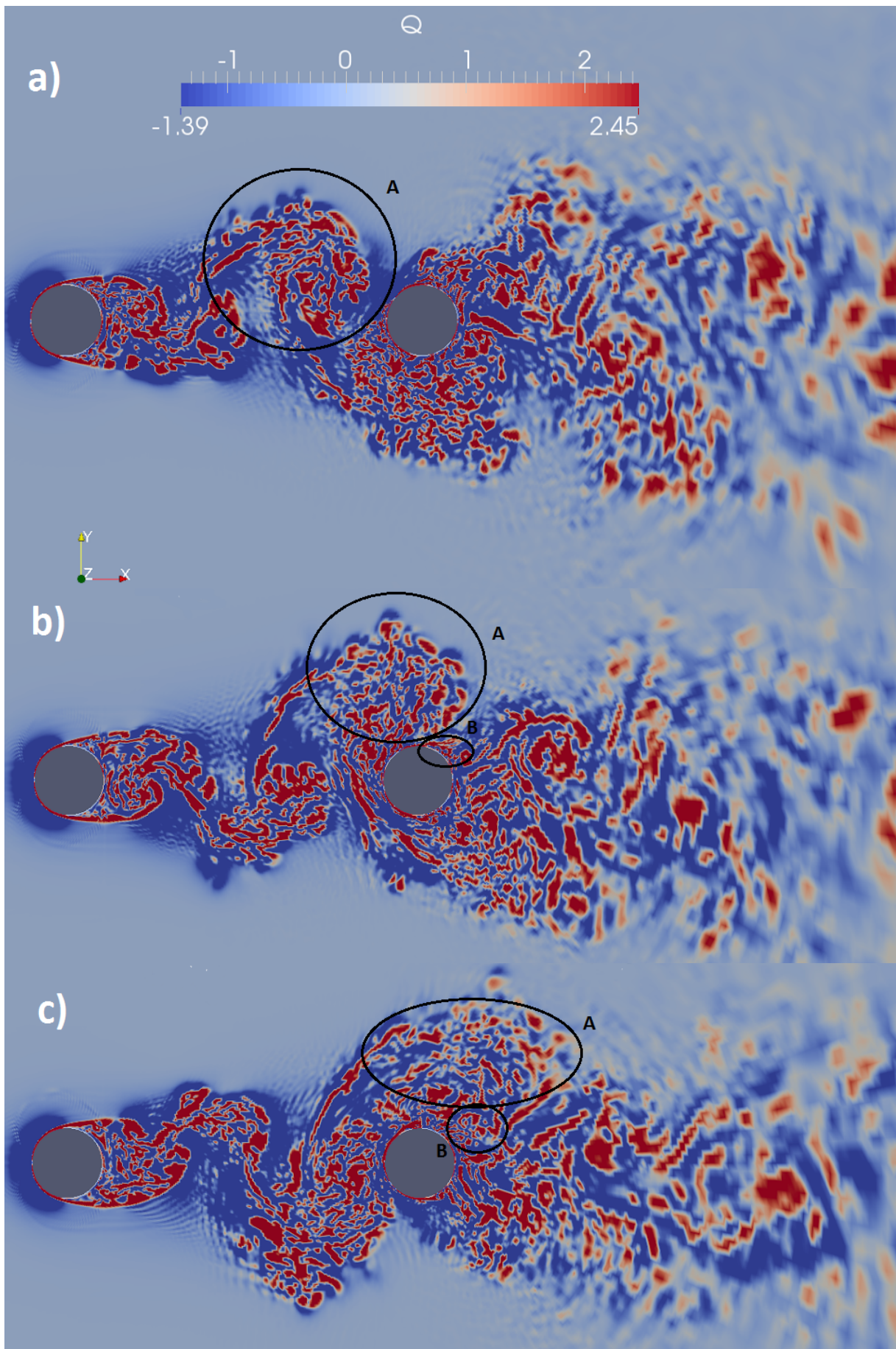


Figure 5.1: Instantaneous vorticity distribution at the mid-span of the cylinders visualized by the Q-criterion. a) vortex A is approaching the downstream cylinder, b) vortex A impinges the downstream cylinder and vortex B is created, c) vortex A is broken up and merges with vortex B

5.2 Wake flow

It is important to get an understanding of what happens in the wake flow behind the cylinders to be able to corroborate the results obtained from the simulation. Some results can be somewhat complicated to interpret, especially if they are based on secondary parameters of the simulation. As previously mentioned, the primary outputs of the Navier-Stokes equations are velocity and pressure. All other variables are computed based on these primary outputs.

Figure 5.2 shows the time-, and space averaged u -velocity profile in the gap behind the upstream cylinder and in the wake behind the downstream cylinder. The results of Prsic et al. (2014) for a single cylinder in uniform flow of the same Reynolds number is plotted together with the two profiles for comparison. The x -axis represents the distance from the respective cylinder center. The value on the y -axis is the normalized velocity u/U_c , where U_c is the free stream velocity of value 1.31. Looking at the upstream cylinder distribution, it is clear that there is a large effect on the u -velocity from the downstream cylinder. The profile follows the one of the single cylinder up to the distance of $2D$ behind the cylinder center. After this point, the velocity profile of the tandem upstream cylinder quickly decreases down to 0 at the point where the downstream cylinder is located (at $x/D = 4.5$) while the profile of the single cylinder increase further and stabilizes at a value of about $u/U_c = 0.7$. The upstream cylinder does not obtain this value of u -velocity. This lower velocity in the gap region is likely lead to discrepancies between results of a single cylinder and the upstream tandem cylinder.

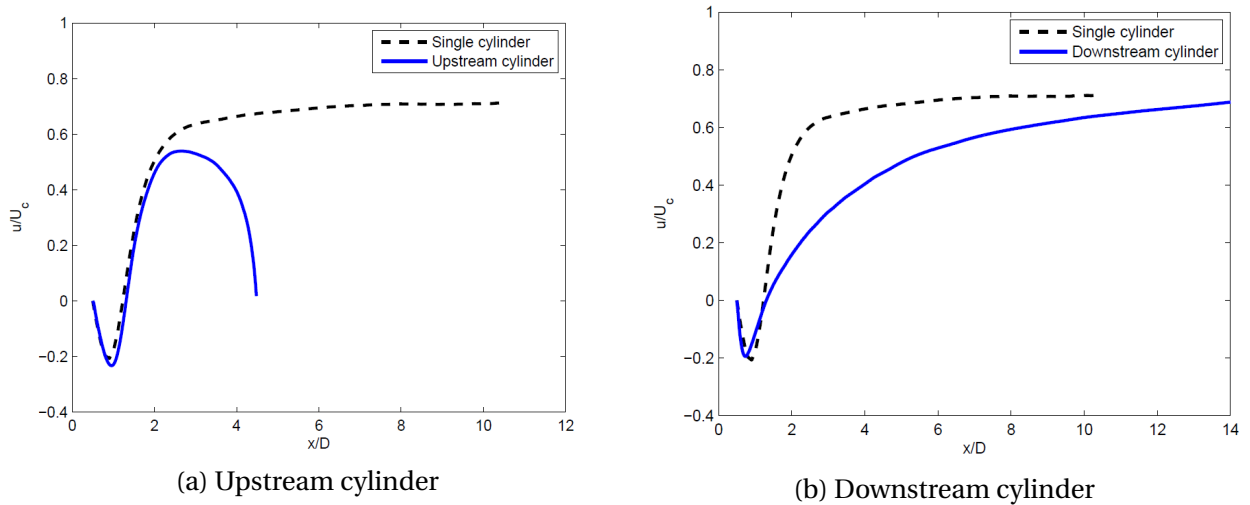


Figure 5.2: Normalized time-, and space averaged u -velocity profile in the wake behind the cylinders along the x -axis, plotted together with the normalized time-, and space averaged u -velocity profile of a single cylinder, single cylinder results from Prsic et al. (2014)

The velocity distribution in the wake behind the downstream is allowed to develop to the level of the single cylinder, but it takes a longer distance behind the cylinder before this level is obtained. The converged level for the single cylinder is obtained after a distance of approximately $3D$, while it takes $14D$ for the downstream tandem cylinder. This is due to the highly turbulent incoming flow onto this cylinder. Naturally, there will also be discrepancies in the results of the downstream cylinder from a single cylinder.

Figure 5.3 shows the velocity profiles of the velocity component u , plotted along the y -axis at a distance $0.6D$ behind the cylinder surface. The distance in the y -direction is shown on the

x-axis of the figures. The y-axis represents the magnitude of the normalized u-velocity. The first thing to note is that the profile behind the downstream cylinder is somewhat different than that of the upstream cylinder, which has a shape that is similar to that of a single cylinder. The decrease in velocity at the sides is not as significant for the downstream cylinder as it is for the upstream. This is due to the more chaotic flow around the downstream cylinder which is spread out over a larger span in the y-direction. Outside of the boundary layer of the upstream cylinder, the velocity decreases quite rapidly towards the free stream velocity, and the flow here can be considered as potential (ref section 2.1). This is not the case for the downstream cylinder. Regarding the magnitude of the velocity, the upstream cylinder experiences a higher peak value than the downstream cylinder. This could be due to the smearing out of the vortices shed from the upstream cylinder. Figure 5.4 is a caption of the mean velocity, \bar{U} taken at the mid span of the cylinders and illustrates this phenomena.

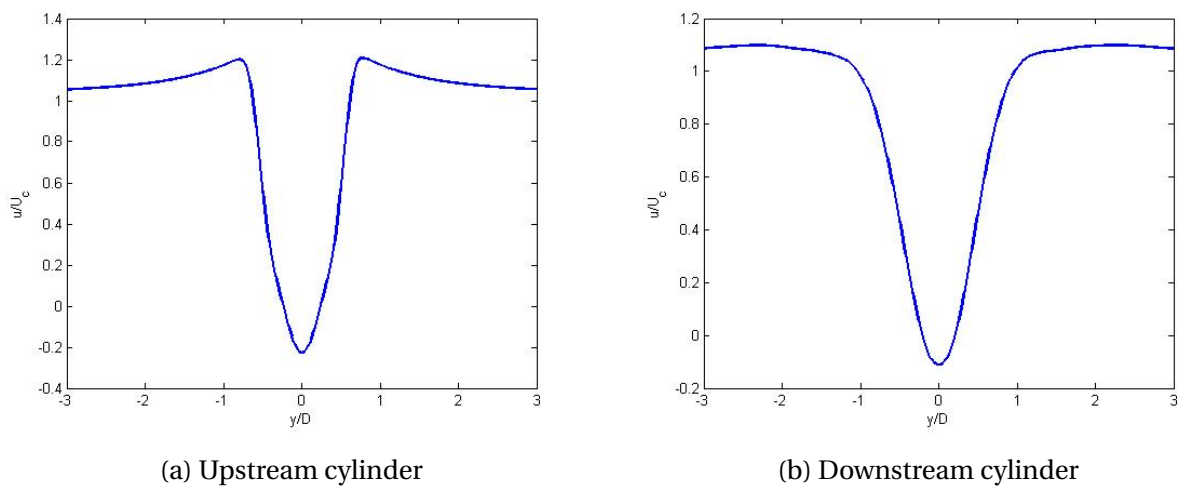


Figure 5.3: Normalized time-, and space averaged u-velocity profile in the wake behind the cylinders along the y-axis

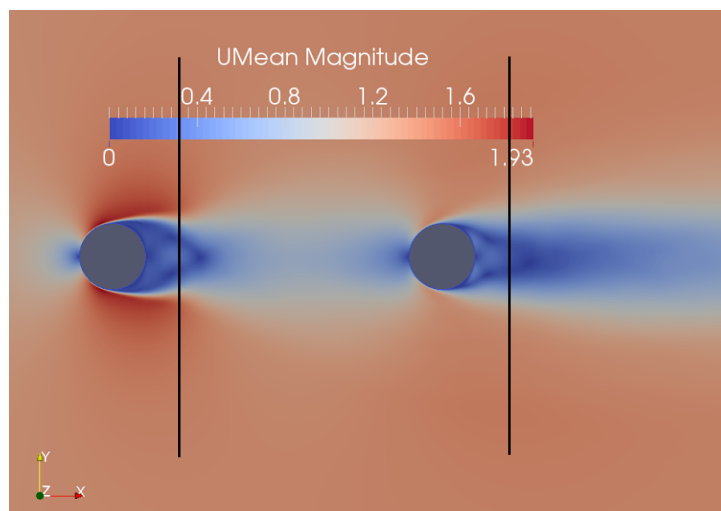


Figure 5.4: Snapshot of the mean velocity taken at the mid span of the cylinders. Vertical lines are drawn where sampling for y cross-section is done

5.3 Mean and RMS pressure distributions

Mean pressure

Figure 5.5 shows the pressure distribution over the upper half of the cylinder surfaces for the upstream and downstream cylinder. The coefficient is plotted at the spanwise location $z = 2$ which is at the middle of the cylinder span. In the figures there are also plotted results from previous work. For detailed plots of the results in this work only, see figure A.1 in appendix A. θ on the x-axis of the figures denotes the angle starting from the upstream side of the cylinder such that $\theta = 0$ is in the front stagnation point of the cylinder.

The upstream cylinder mean pressure distribution resembles that of a single cylinder. This is because the spacing between the two cylinders is greater than the critical spacing for the current Reynolds number, (see figure 2.7). Vortices are allowed to be formed behind the upstream cylinder and separated from it. This flow picture is called jump flow (flow picture F of Igarashi (1981), ref. section 2.2.2). We can see that separation occurs at about $\theta = 90 - 100$ due to the flattening of the pressure curve (ref. section 2.1.2). The minimum value of the mean pressure coefficient of approximately $\bar{C}_p = -1.3$ is located at $\theta = 70$. This agrees relatively well with the experimental results of Ljungkrona and Sundén (1993) and Igarashi (1981). In Ljungkrona and Sundén (1993), whose conditions are nearest to the ones on this work, the minimum value for Reynolds number $Re = 1.2 \cdot 10^4$ and spacing $S/D = 4$ was $\bar{C}_p = -1.2$. Considering the slight differences in Reynolds number and spacing, this is an acceptable difference. The results of Prsic et al. (2014) also agree very well, only that the minimum value is slightly lower. This could be due to the presence of the downstream cylinder in this work whereas Prsic et al. (2014) describes a single cylinder, (ref. section 5.2). The results also agree well with the numerical results of Kitagawa and Ohta (2008).

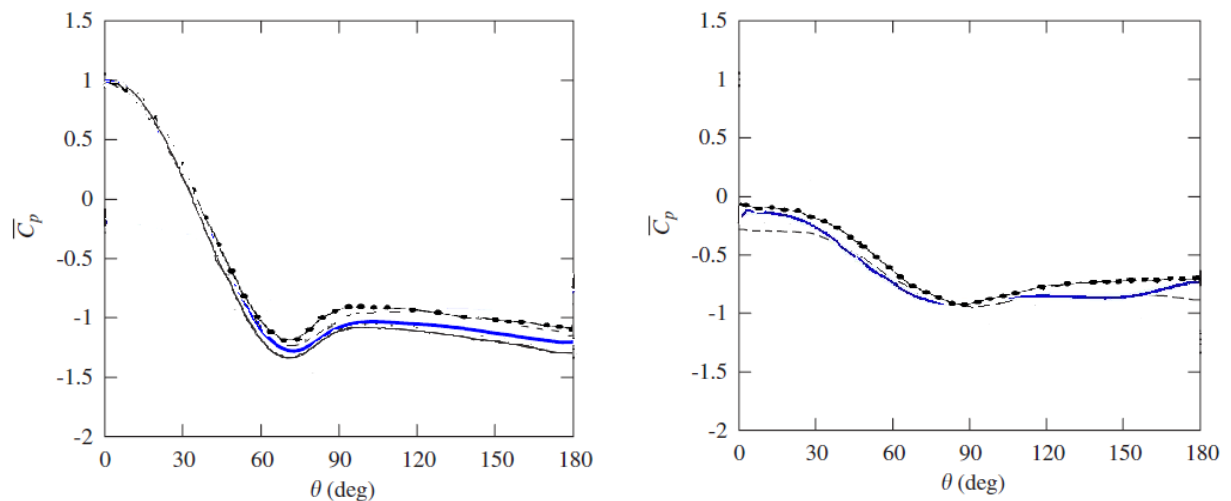
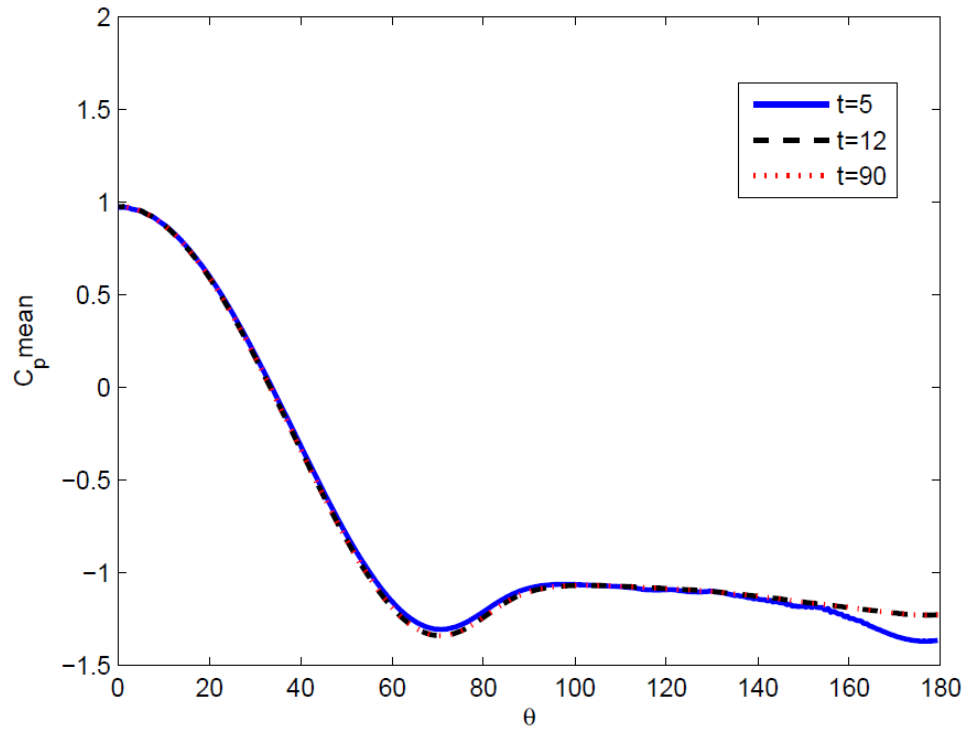


Figure 5.5: Mean pressure distribution over the cylinder surface. top: upstream cylinder, bottom: downstream cylinder. Blue line: current work, •: Ljungkrona et al. (1991), $Re = 12 \cdot 10^3$ $S/D = 4$, dashed line: Kitagawa and Ohta (2008) $Re = 2.2 \cdot 10^4$ $S/D = 4$, solid line: Prsic et al. (2014) $Re = 1.31 \cdot 10^4$ Single cylinder

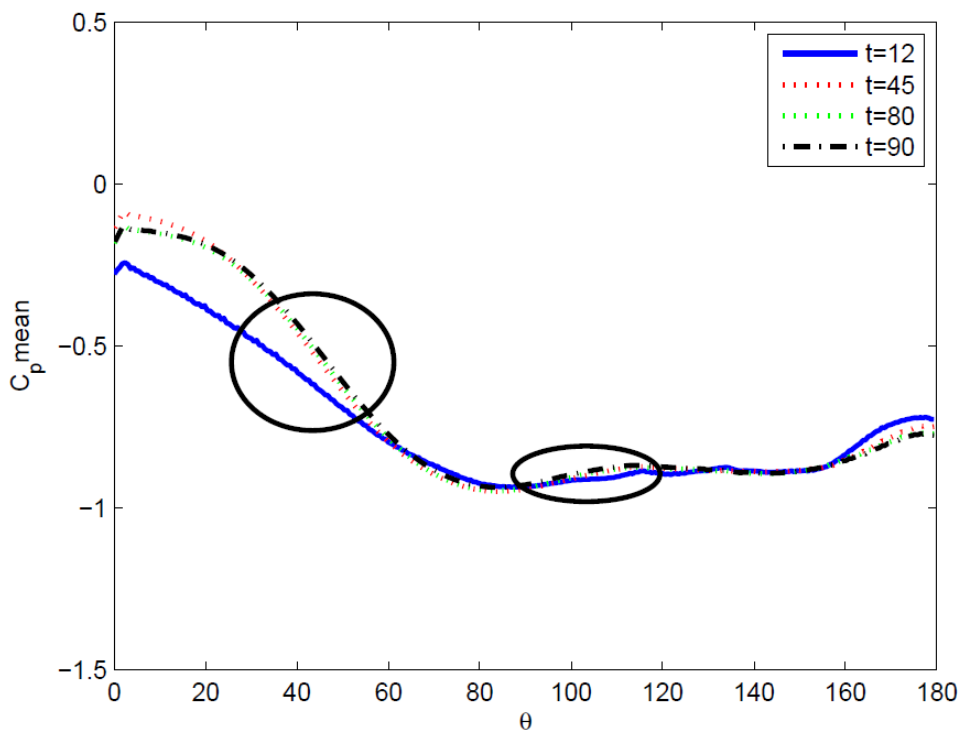
The downstream cylinder mean pressure distribution in figure 5.5 also resembles the one of a single cylinder but has a more irregular shape than the ones of the above mentioned pre-

vious work. Due to the vortices that roll up in front of the downstream cylinders, the inflow onto this cylinder is more turbulent and chaotic than that of the upstream cylinder and this is reflected in the pressure distribution. In the interval $0 < \theta < 110$ the results resembles the ones of [Ljungkrona and Sundén \(1993\)](#) and [Kitagawa and Ohta \(2008\)](#) with the minimum located at slightly to the left of the others. The minimum value of $\bar{C}_p = -0.95$ is similar to all three cases. One has to keep in mind that the Reynolds number and spacings are not identical in these cases. For $\theta > 110$, \bar{C}_p decreases into a new local minimum and then increases again. The increase in pressure in the tail, that is at the downstream stagnation point of the downstream cylinder, indicates that the vortices that rolls up behind this cylinder touches back onto the cylinder after separation. This tendency is not seen in the above mentioned work, where \bar{C}_p tends to increase steadily and settle at a certain value. This discrepancy in the shape of the mean pressure coefficient could be due to the averaging process. [Kitagawa and Ohta \(2008\)](#) averaged over approximately 50 vortex shedding periods which most likely gives a more reasonable averaged profile.

To illustrate this, figure 5.6 shows the mean pressure coefficient distribution of the upstream and downstream cylinder plotted for different averaging periods. The upstream cylinder in the top figure has a fast converging distribution. The distribution converges after only 12 seconds of averaging. The downstream cylinder distribution in the bottom picture shows a lot more varying distribution for different averaging periods, and there are also small differences between the two last averaging periods of 80 and 90 seconds. These are marked by a black circle in the figure. One can thus argue that the shape may change if the solution is averaged over an even longer period of time. The figure also shows that the second minimum becomes less prominent for the longer averaging periods.



(a) Upstream cylinder



(b) Downstream cylinder

Figure 5.6: Convergence of mean pressure coefficient distribution for upstream and downstream cylinder.

RMS pressure

The RMS, or fluctuating, pressure distribution, gives an indication of where on the cylinder surface the separation and possibly reattachment happens. The fluctuation magnitude also

indicates the force magnitude. Figure 5.7 shows the time averaged RMS pressure distribution over the two cylinder surfaces. The distribution is plotted over the cylinder surfaces at the mid-span of the cylinders, at $z = 2$. The distributions is plotted together with the results of Igarashi (1981) for comparison. Note that in the right figure, the distributions of the current case and for spacing $S/D = 3.82$ are scaled after the right axis.

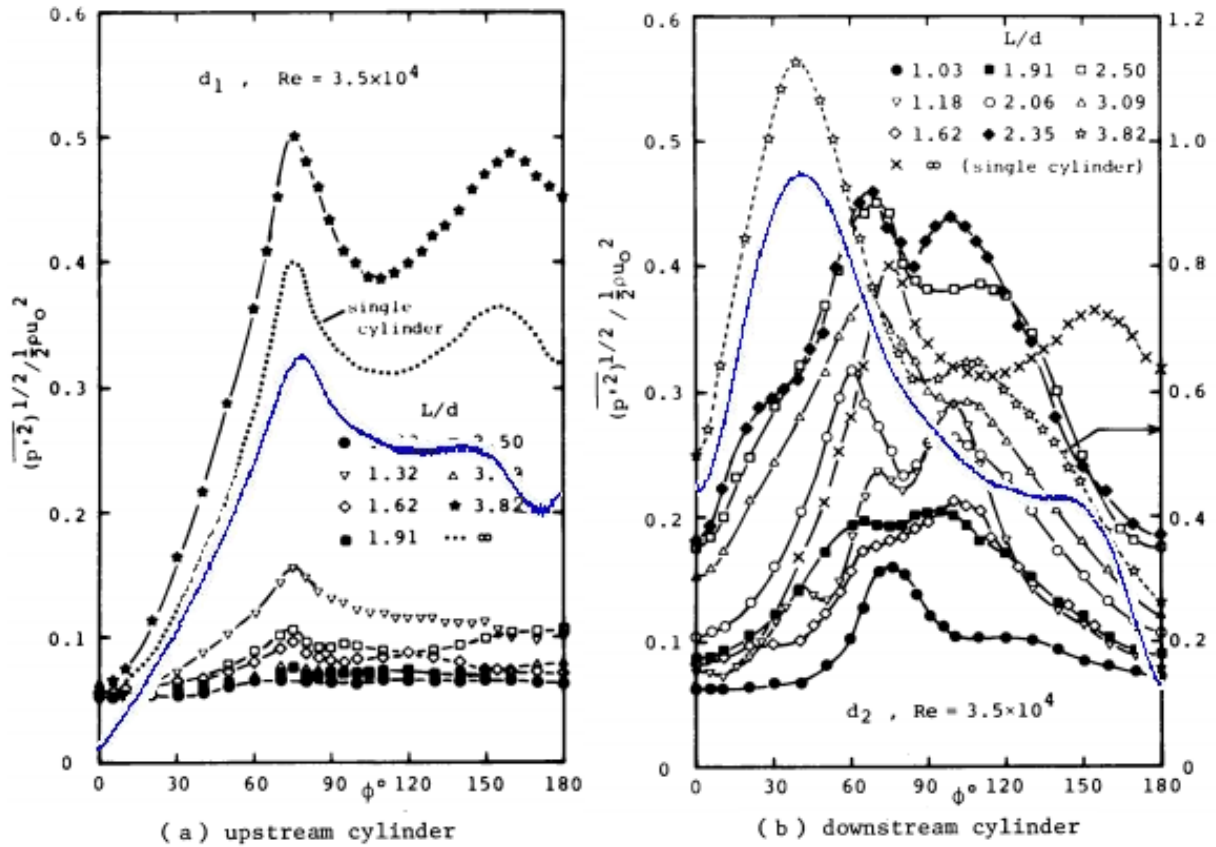


Figure 5.7: Distribution of RMS pressure fluctuation around two tandem cylinder surfaces. Figure based on Igarashi (1981). Blue line: current work, dotted line in (a): single cylinder, \star or \star : $S/D = 3.82$.

There are clearly some discrepancies between the results of Igarashi (1981) and this work. Keeping in mind that Igarashi (1981) had a Reynolds number of $Re = 3.5 \cdot 10^4$, which is higher than that of this work. Looking at the upstream cylinder distribution, the distribution of this work follows the shape of the compared distributions of the single cylinder and the cylinders of spacing $S/D = 3.82$ in the interval $0 < \theta < 90$, but the values are shifted down. The starting values of Igarashi (1981) is 0.05 while it is approximately 0 in the current results. Shifting the profile to match the start value of the Igarashi (1981) profiles, the distribution would follow more accurately the one of a single cylinder. The first peak in the distribution is due to separation and it is located near the separation point. The second peak, which is not as prominent in the current results as it is for Igarashi (1981), is due to the separated flow rolling up into a vortex and the reverse flow reattaching onto the cylinder. It separates again at the second peak.

Compared to the upstream cylinder, the pressure fluctuations on the downstream cylinder are very large. Also here, there are two peaks in the profile. The first and largest peak is due

to the impingement of the vortices shed from the upstream cylinder onto the downstream cylinder. This happens at $\theta = 40$. It is not certain that the impingement location is constant for every vortex, remembering that this is a time-averaged distribution. The first peak is smaller in this work than that of Igarashi (1981). The second peak is according to Igarashi (1981) due to the separation of vortices from the downstream cylinder. In this work the peak is located at approximately $\theta = 150$ while Igarashi (1981) found it to be at $\theta = 110$. It is not likely, looking at figure 5.8, that this peak is due to separation. The two points, $\theta = 110$ in red and $\theta = 150$ in yellow, are marked in the figure. The streamlines shows U. It is clear that $\theta = 110$ is closer to where the separation occurs. The second peak of the current work distribution could however be due to the reattachment of the reverse flow back onto the cylinder, as for the upstream cylinder. The number of peaks on the downstream RMS pressure distribution has been subjected to discrepancies for other research as well. Kitagawa and Ohta (2008) found that the downstream cylinder only had one peak in the RMS pressure distribution for a spacing of $S/D = 4$, while Ljungkrona et al. (1991) presented a distribution with two peaks. There seems to be a discrepancy between numerical and experimental results. The absence of the second peak could be a result of the turbulence model not being able to pick up the details of the chaotic flow around the downstream cylinder. Kitagawa and Ohta (2008) used the same LES turbulence model with the Smagorinsky subgrid scale as in the present work. The discrepancies between the present results and Igarashi (1981) could also have something to do with the different spacings. Igarashi's largest spacing was 3.82 while it is 5 in this work. One can discuss whether the RMS profile of the downstream cylinder in this work looks more like that of the upstream cylinder. The first peak is larger due to the vortex impingement, but the second peak is located at approximately the same position and the profiles are somewhat similar. The large spacing could make the downstream cylinder less affected by the upstream cylinder and rather cause it to act as a single cylinder in a highly unsteady turbulent incoming flow.

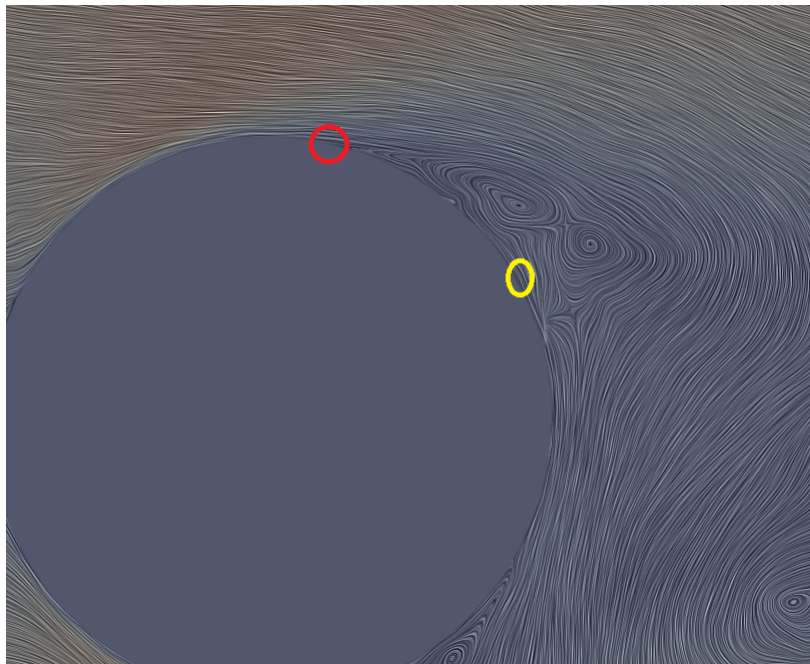


Figure 5.8: SurfaceLIC streamlines of U on downstream cylinder at $z = 2$ with points marked in yellow at $\theta = 110$ and red at $\theta = 150$.

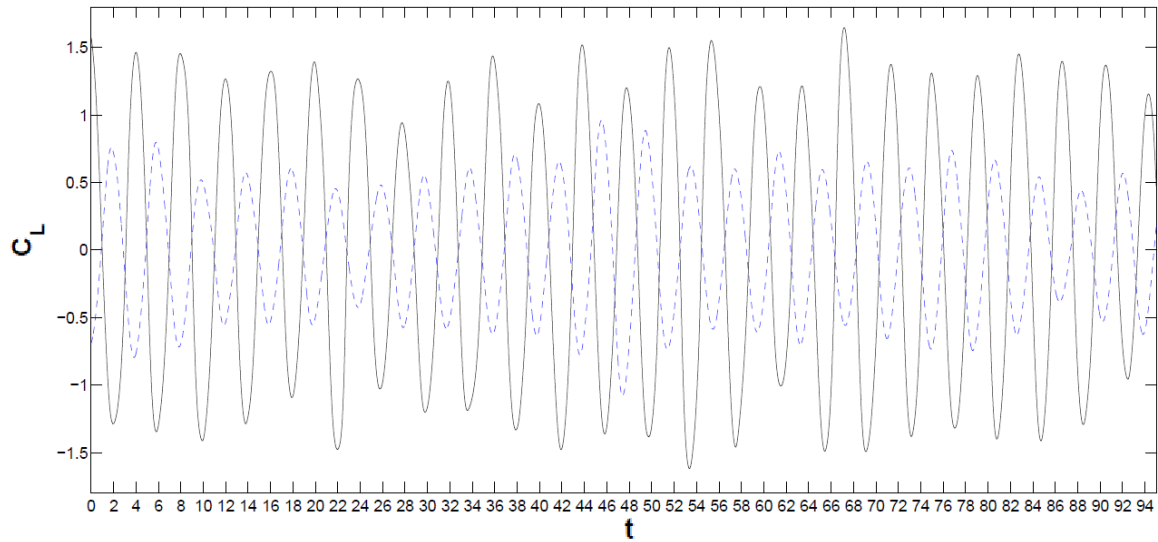
Compared to the distributions of cylinders with spacings smaller than the critical spacing,

the RMS pressure is much larger for the cylinders with spacing above the critical spacing. The shear layer is allowed to roll up behind the upstream cylinder and form vortices that are shed from the upstream cylinder. This causes large pressure fluctuations at the separation points. This peak is also seen on the upstream cylinder for the arrangement below the critical spacing, but it has a much smaller magnitude. The peak of the reverse flow reattaching onto the cylinder is not seen for these arrangements. This is due to the flow that separates from the upstream cylinder reattaches onto the downstream cylinder. There is not much flow in the gap between the cylinders. This is reflected in the very low RMS value at the tail of the upstream cylinder. For the downstream cylinder, the difference between over and under critical spacing is that the cylinders under critical spacings has a reattachment peak and a separation peak, while the cylinders above critical spacing does not have the reattachment peak. Instead they have the impingement peak of much higher magnitude.

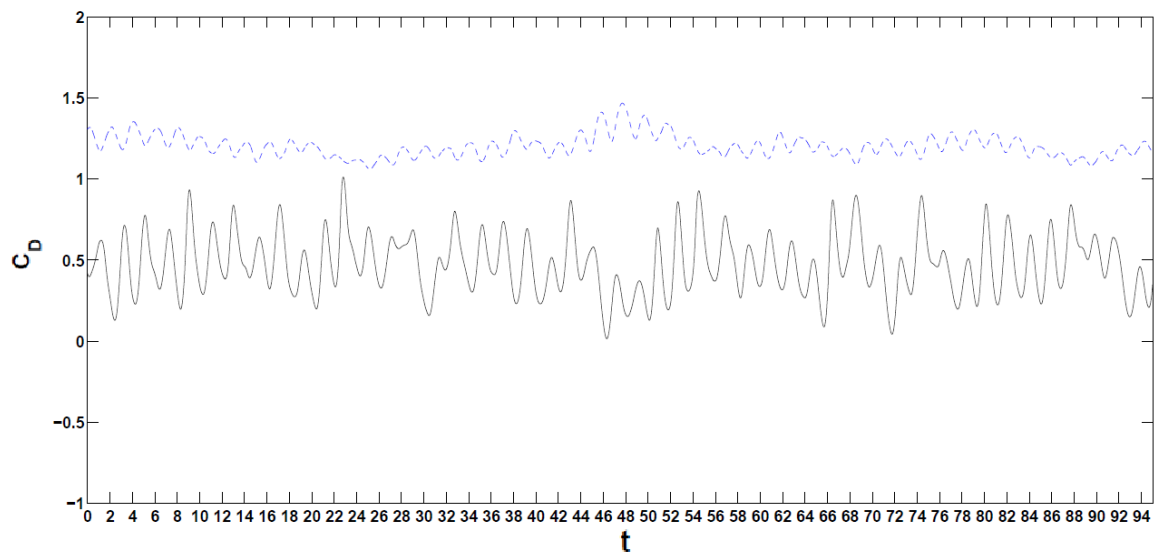
5.4 Drag and lift coefficients

Figure 5.9 shows the time history for the lift-, and drag coefficients for the tandem cylinders. The horizontal axis shows the time span. The dashed line in the figures represents the downstream cylinder and the solid line represents the upstream cylinder. For the lift coefficient there are clearly variations in time of the value. This thus supports the theory of time averaging over a long period of time as mentioned in the introduction to this chapter. When looking at the time- and space averaged results it is important to keep in mind these large variations in time and that the details of these variations are faded out when time averaging is performed.

Comparing the lift coefficient time series to the one of [Abrahamsen-Prsic \(2015\)](#) we see that the values at the free side of the cylinder, that is the side with no wall proximity, are quite similar to the ones obtained in this work. The maximum value lies around 1.5 for the downstream cylinder, which is also the case for the minimum values in this work. The symmetry is because there is no wall proximity in the case in this work. The values for the upstream cylinder lift coefficient is somewhat lower than that of [Abrahamsen-Prsic \(2015\)](#). One thing to note is that the lift force on the downstream cylinder is large compared to that of the upstream cylinder. This could be due to two things: the impingement of the vortex shed from the upstream cylinder on the downstream cylinder and the formation of a vortex on the downstream cylinder. Both of these induce a lift force on the cylinder. The force is large due to the synchronization of the impingement and the vortex formation, ([Kitagawa and Ohta, 2008](#)), (ref. section 5.1). The vortex separation and impingement shown in figure 5.1 corresponds to the last vortex shedding period shown in the drag and lift time histories shown in figure 5.9. This vortex is of the weak ones, seen from the lower peak values of the lift coefficient for the upstream and downstream cylinder. This is most likely the reason for the relatively non-merged vortices shown in figure 5.1.



(a) Time history of the lift coefficient for upstream and downstream cylinder.



(b) Time history of the drag coefficient for upstream and downstream cylinder.

Figure 5.9: History of lift and drag coefficients for upstream and downstream cylinder. Top picture: lift coefficient, bottom picture: drag coefficient. Dashed line: upstream cylinder, solid line: downstream cylinder.

Regarding the phase of the lift coefficients for the upstream and downstream cylinder, the peaks of the downstream lift is shifted somewhat to the right of the peaks of the upstream lift. An impingement of a vortex shed from the underside of the upstream cylinder onto the downstream cylinder leads to a vortex shed from the upside of this cylinder. It is thus somewhat complicated to see the correlation between the two curves. Figure 5.10 shows a more detailed version of figure 5.9. It zooms in on the last vortex shedding period shown in figure 5.9. The figure shows that it takes about 4 seconds for the vortex shed from the upstream cylinder to move over the gap and impinge the downstream cylinder. Every tick on the x-axis represent 0.2 seconds.

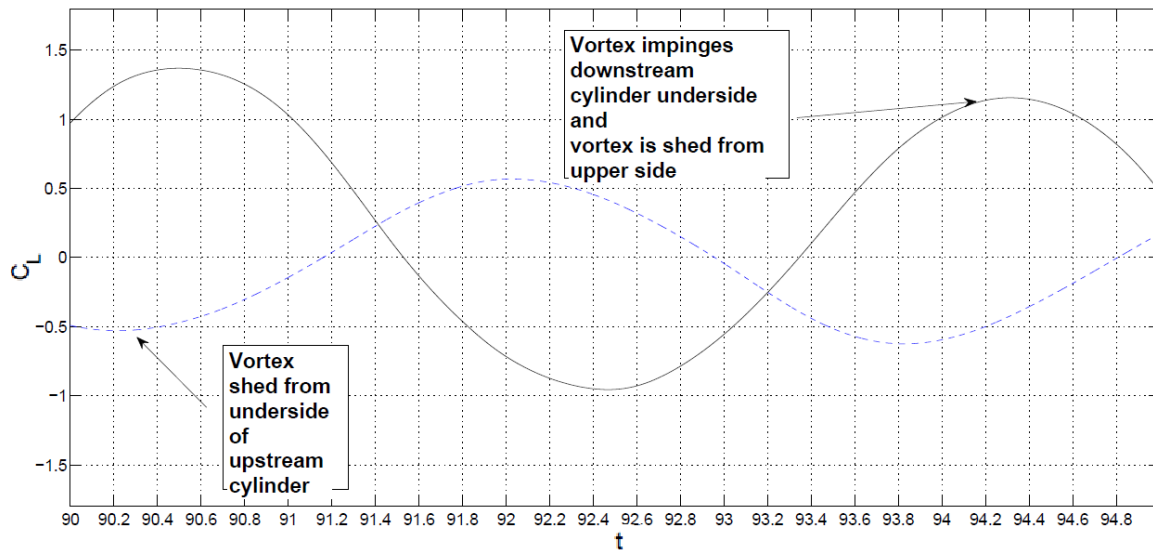


Figure 5.10: Lift coefficient time series of 1 vortex shedding period. Dashed line: upstream cylinder, solid line: downstream cylinder.

The time history of the drag coefficient shown in figure 5.9b is characterized by non-stationary fluctuations. Note should again be taken to that these non-predictable fluctuations will have a large effect on the averaging process. A large deviation could possibly had happened directly after this simulation was ended, and would contribute to a different averaging result. The reason for these irregularities in the drag coefficient is the different strength of the vortices shed from the upstream cylinder and the variable impingement position on the downstream cylinder, (Kitagawa and Ohta, 2008).

The mean drag coefficient and the lift coefficient RMS for the upstream and downstream cylinder are given and compared to referred work in table 5.2. The results of this study mostly agree with the compared results. Naturally the results of Abrahamsen-Prsic (2015) have some deviations which are probably due to the wall proximity. The drag is higher for both cylinders which would be expected when there is a blockage of the flow such as a wall. The rather small discrepancies from the other cases are possibly related to the difference in Reynolds number. Such a span of results is often seen in numerical investigations, and especially when compared to experimental results. Experiments follow completely different premises than a numerical simulation. Results tend to change for different experiments done with the same conditions. Some discrepancies in results are thus expected and accepted.

5.5 Strouhal number

To find the Strouhal number behind the upstream and the downstream cylinder, a fast fourier transform is used on the signal of velocity component v in the wake behind the two cylinders. The probes are located at coordinates (1, 0.3, 2) and (8, 0.3, 2). These points are shown in figure 5.11.

Table 5.2: Mean drag and lift RMS for different cases

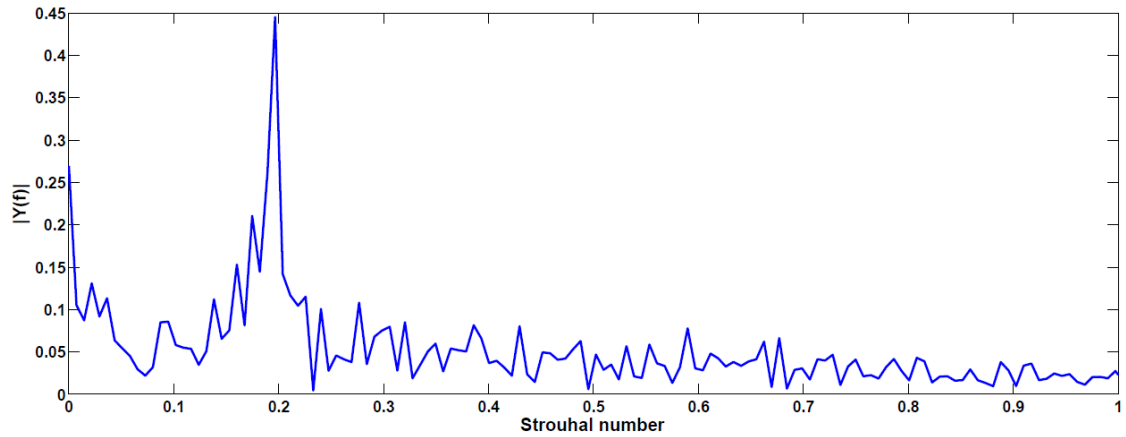
Case	$Re \cdot 10^4$	\bar{C}_{D1}	\bar{C}_{D2}	C'_{L1}	C'_{L2}
Present work	1.31	1.1615	0.48	0.49	0.98
Igarashi (1981)	3.55	1.3	0.45		
Prsic et al. (2014)	1.31	1.3132		0.5454	
Abrahamsen-Prsic (2015), L5 t2	1.31	1.32	0.64	0.53	0.92
Kitagawa and Ohta (2008)	2.2	1.13	0.5	0.2	1
Ljungkrona et al. (1991)	2	1.25	0.45		

Figure 5.11: Probe locations marked in the computational domain with coloring of velocity U

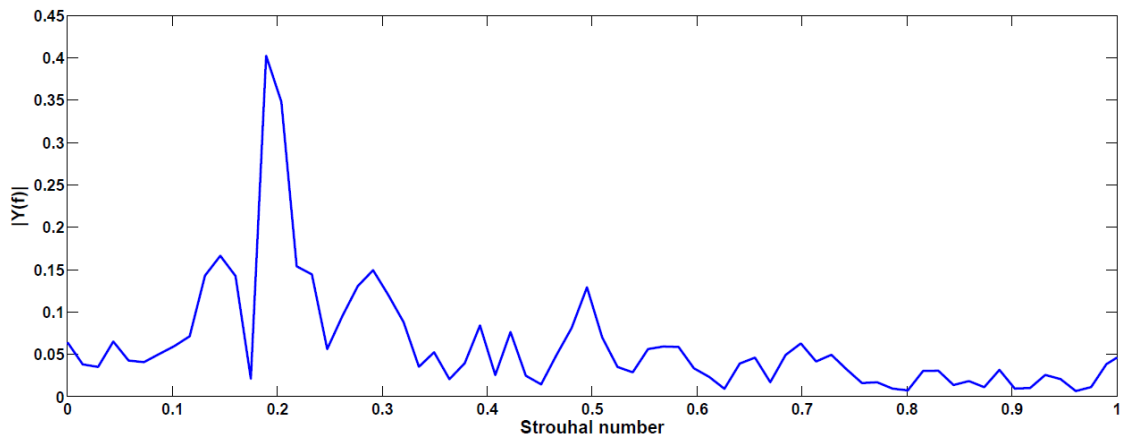
Figure 5.12 shows the fast fourier transform spectra of the Strouhal frequency at the two probe locations. Clear peaks are seen at Strouhal number of about 0.2, which is expected. This supports the theory of the co-shedding flow regime, or synchronized vortex shedding. The exact value for the peak Strouhal numbers are 0.1966 for probe 1 and 0.1893 for probe 2. These results agree well with Kitagawa and Ohta (2008) and Igarashi (1981), only that Igarashi (1981) observed a slightly higher Strouhal number of 0.2. There is also a good agreement with the results from Xu and Zhou (2004) for $Re = 2.9 \cdot 10^3$, (ref. figure 2.12). The small discrepancy between the probe 1 and probe 2 Strouhal number could be the location of probe two. Ideally, the probe should be positioned closer to the downstream cylinder. At its present location, errors could occur due to the some dissipation of the vortices. This could also be some of the reason for the numerous other smaller peaks in the probe 2 specter, though this is also expected in a more turbulent and thus more fluctuating flow.

When compared to the lift coefficient fluctuations, the frequency of the fluctuations in the v -component of the velocity corresponds to the frequency of the lift coefficient. The Strouhal number could thus be read from the lift-coefficient curves. This is done in many cases, but there are some uncertainties in this. It is always better to read the frequency from the primary

outputs from the computations, like the velocity. The Strouhal number of the lift-coefficient for the upstream and downstream cylinders are 0.195 and 0.1928, respectively.



(a) fast fourier transform specter of Strouhal frequency magnitude for probe 1 behind upstream cylinder



(b) fast fourier transform specter of Strouhal frequency magnitude for probe 2 behind downstream cylinder

Figure 5.12: Strouhal frequency spectra for probes behind upstream and downstream cylinder

5.6 Separation

To visualize the separation angle along the span of the cylinders, the application wall bounded streamlines in OpenFOAM is used. This function is used to visualize near wall flows, and streamlines are made very close to the surface. The script for this application is located in the system-folder. In appendix B.2 you can find the script used in this work. Figure 5.13 and 5.14 shows the streamlines for the instantaneous velocity and mean velocity, respectively.

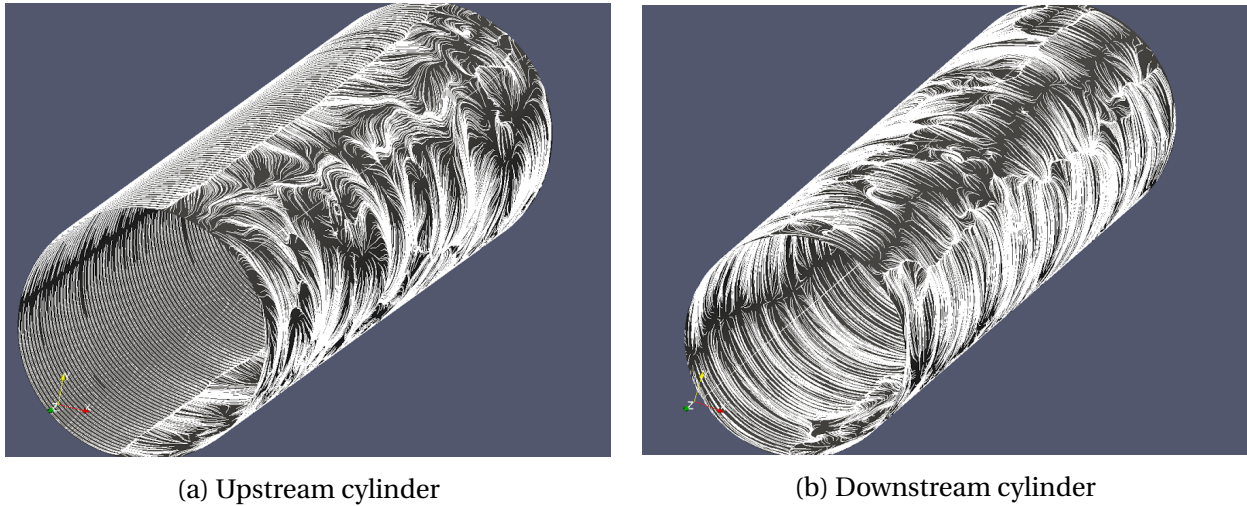


Figure 5.13: Surface streamlines for the instantaneous velocity U_c at the cylinder surfaces

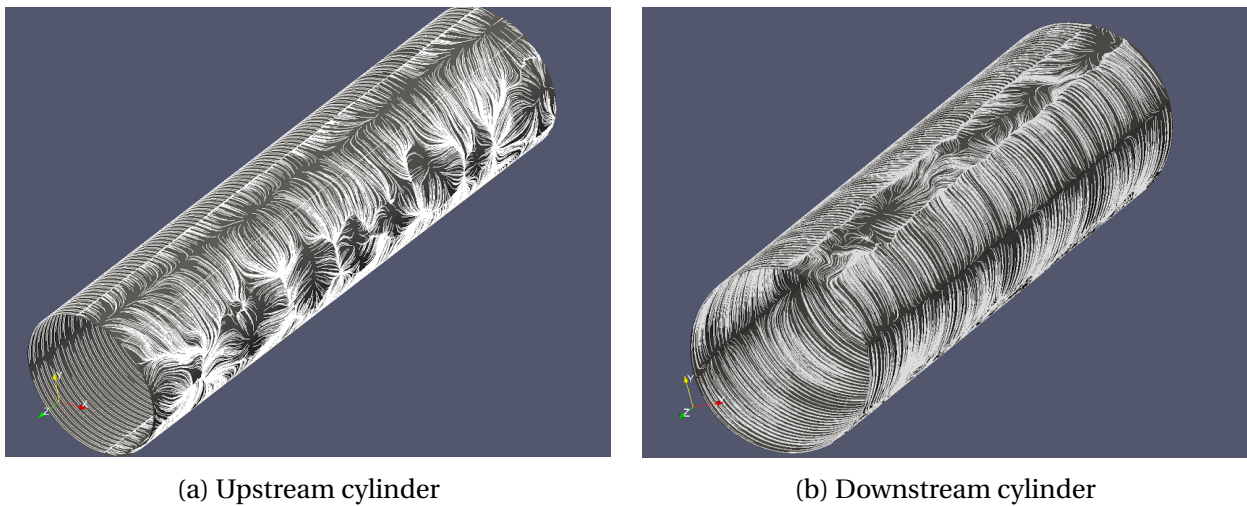
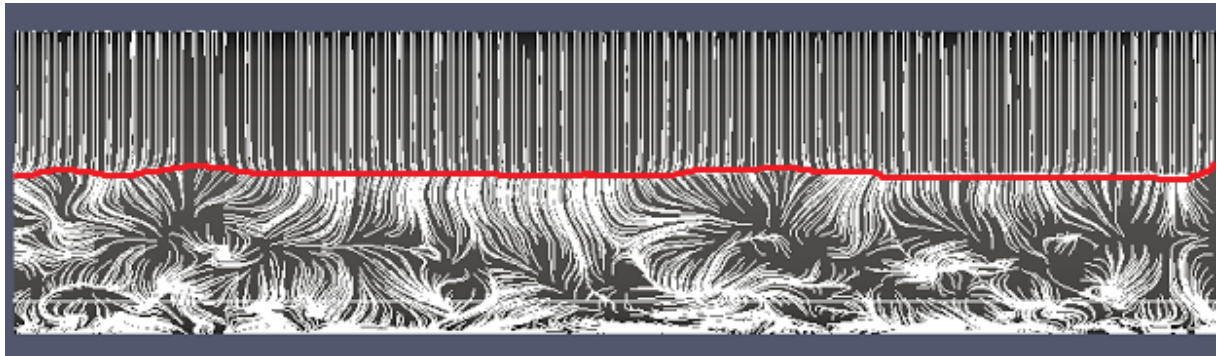


Figure 5.14: Surface streamlines for the mean velocity U_c at the cylinder surfaces

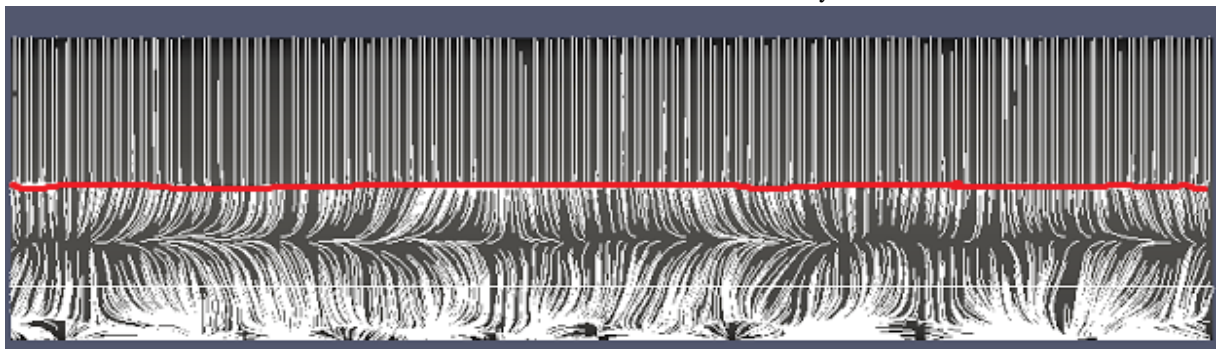
Figure 5.13a shows the instantaneous velocity streamlines for the upstream cylinder. When compared to figure 5.13b, which shows the downstream cylinder, it is clear that the flow over the upstream cylinder is more regular. This has also been the conclusion of the previously given results in this chapter, but this figure visualizes it very well. Another thing that should be noted is the difference in the averaged velocity streamlines between the gap side of the upstream cylinder and the wake side of the downstream cylinder, at $\theta = 180$ for both cylinders. Behind the upstream cylinder it looks like the flow is curled up and gathered at certain points along the span, while the flow is more even behind the downstream cylinder. This could be some effect of the presence of the downstream cylinder on the upstream cylinder. The separation lines are shown in figure 5.15, where a red line is drawn along the line. The screen shots are taken from above the cylinders (looking down on the x - z plane), with the flow coming from the top and moving downwards.



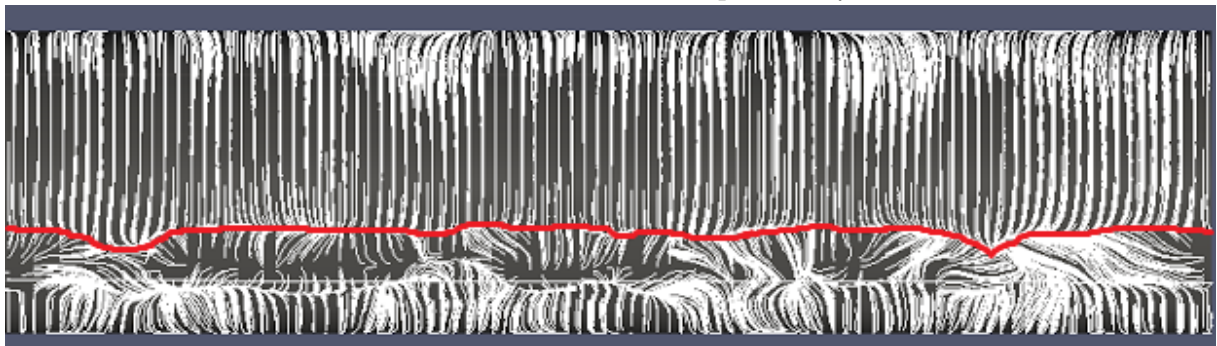
(a) Streamlines of U on the upstream cylinder



(b) Streamlines of U on the downstream cylinder



(c) Streamlines of U mean on the upstream cylinder



(d) Streamlines of U mean on the downstream cylinder

Figure 5.15: Separation lines of the upstream and downstream cylinder for U and U mean

Figure 5.15a shows the separation line of U for the upstream cylinder. The line is quite even along the entire cylinder span at about $\theta = 90^\circ$. However, there are small irregularities over the span. This is expected due to the 3D effects discussed in chapter 2.2.5. There are

correlation lengths over the cylinder span which have the same vortex shedding phase and the separation also seems to happen at the same angle. Towards the ends of the cylinder span, there are larger irregularities that stand out from the rest of the span. These could be due to the some effect of the boundary condition at the domain ends perpendicular to the cylinder axis.

The downstream cylinder in figure 5.15b is characterized by a more chaotic flow than the upstream cylinder. There is no even separation line and the flow separates over a wider range of degrees, $100 < \theta < 110$. Looking at figure 5.13b, there seems to be a second flow line at about $\theta = 150$. This could be due to some backflow reattaching back onto the cylinder and could also have something to do with the second peak in the RMS pressure distribution for the downstream cylinder discussed in section 5.3.

The separation lines of the averaged velocity streamlines are shown in figure 5.15c and 5.15d and are much more even than those of the instantaneous velocity streamlines. The upstream cylinder has a separation line at about $\theta = 90$, which was also the case for the instantaneous separation line. This supports the theory of the shorter averaging period needed for the upstream cylinder results before convergence. As seen in figure 5.15d this is not the case for the downstream cylinder at about $\theta = 100$. The separation thus occur a bit further along the cylinder surface than for the upstream cylinder. The separation line is more even than it is for the instantaneous velocity, but it is still not completely even. This could again mean that the flow should be averaged over a longer time before the results of the downstream cylinder could be trusted to represent completely converged results. It should be noted that the mean velocity streamlines are taken for the latest time step.

Chapter 6

Conclusion

6.1 Conclusion

Numerical simulations of a turbulent 3D flow of Reynolds number $Re = 1.31 \cdot 10^4$ over two circular cylinders in tandem. The center to center spacing between the cylinders was $S/D = 5$. A LES turbulence model with a Smagorinsky subgrid scale model was used to model the turbulence. The following conclusion can be drawn by reviewing the results of this work.

- **Agreement with previous research.** The author has not found any previous research done with the exact same flow parameters and geometries as this study. However, many studies have been performed with other Reynolds numbers and spacings, both numerically and experimental. Comparison with results from such research will give an indication on the credibility of the results. In general the results agree well with the previous studies of [Igarashi \(1981\)](#), [Kitagawa and Ohta \(2008\)](#) and [Ljungkrona and Sundén \(1993\)](#). Some discrepancies were found to the experimental studies of [Ljungkrona and Sundén \(1993\)](#) and [Igarashi \(1981\)](#), especially in the RMS pressure distribution.
- **Flow picture.** For the spacing $S/D = 5$ and Reynolds number $Re = 1.31 \cdot 10^4$, the free shear layer roll up behind the upstream cylinder and form vortices that are shed from the cylinder. This was visualized with a vortex identification scheme. The formation length of the vortices are smaller than the spacing between the cylinders at this Reynolds number and vortices are thus allowed to form behind the upstream cylinder. The vortices move backwards over the gap region between the cylinders and impinge the downstream cylinder. This flow picture is called jump flow. The incoming flow onto the downstream cylinder was characterized by large turbulence.
- **Vortex shedding and oscillatory forces.** Due to the impingement of the vortices shed from the upstream cylinder onto the downstream cylinder, large oscillatory forces are subjected onto the downstream cylinder. The lift on the downstream cylinder has a magnitude that is about double of the lift on the upstream cylinder. The large lift force is due to the synchronizing between the impingement of vortices shed from the upstream cylinder onto the downstream cylinder and formation of a new vortex on the downstream cylinder. This is called synchronized vortex shedding. This was reflected in that the Strouhal number for both the cylinders being similar.

- **Velocity distributions in the wake.** The downstream cylinder had a noticeable effect on the u -velocity component distribution along the axis parallel to the flow. The distribution did not follow the distribution profile of a single cylinder wake. Neither did the distribution behind the downstream cylinder due to the chaotic flow picture. The velocity distribution along the axis normal to the flow was for the upstream cylinder similar to the one of a single cylinder, while the downstream cylinder distribution was characterized by the chaotic flow.
- **Pressure distributions.** The mean pressure distribution of the upstream cylinder resembles the one of a single cylinder. Some discrepancies from the case of [Prsic et al. \(2014\)](#) was found, most likely due to the downstream cylinder presence. The downstream cylinder distribution resembled one of a single cylinder with turbulent separation due to the turbulent inflow.
- **Separation.** Instantaneous and averaged surface velocity streamlines show that the downstream cylinder sees a much more chaotic flow than the upstream one, and the separation line is very irregular. The averaged streamlines show that the separation happens at about $\theta = 90$ for the upstream cylinder and $\theta = 100$ for the downstream cylinder. They also show that the separation line for the downstream cylinder is still not completely even, which could mean that the results should be averaged over a longer time period to get fully converged results.
- **Turbulence model.** The LES turbulence model with the Smagorinsky subgrid scale model gave satisfying results that agreed well with previous research. There are some flow details on the downstream cylinder that does not seem to be captured by the LES turbulence modeling. The absence of a second peak in the RMS pressure distribution for the downstream cylinder indicates this.

6.2 Practical relevance

As mentioned in chapter 1, circular cylinders are frequently encountered in the marine offshore industry among numerous other. Two circular cylinders in the vicinity of each other are utilized in many applications. It is thus important to understand how the flow around tandem cylinders affect each cylinder. For the spacing used in this work, the flow picture is jump flow. Vortices roll up behind the upstream cylinder and impinges the downstream cylinder, which lead to large fluctuating pressure on the downstream cylinder. The downstream cylinder will thus experience large movements and needs must be taken to protect this cylinder from fatigue and damage.

The Reynolds number used in this work is 13100, which is in the subcritical flow regime. With the kinematic viscosity of about $\nu = 1.4 - 1.6 \cdot 10^{-6} m^2/s$ and with current- and wave induced velocities, the Reynolds number for cylinders with diameter in the size range of 1 meter could be somewhat higher than in this work. But the subcritical flow regime will show the turbulence effect of the flow. Since the flow picture, drag- and lift coefficients, Strouhal number, etc. is dependent on Reynolds number there could be some differences in the results when the Reynolds number is increased. However, the largest changes are normally seen when the flow changes from laminar to turbulent. Simulations of a turbulent flow thus give a realistic impression of what will happen to the cylinders in a real environment.

6.3 Recommendations for further work

Free stream flow over tandem cylinders is a basis for numerous other investigations. The arrangement is the simplest when it comes to flow around multiple cylinders, with two equal sized smooth cylinders in incoming flow hitting perfectly straight on. Though it is a very good basis for understanding flow around tandem cylinders, the reality is not always as simple. With this in mind, here are some suggestions to other investigations that can be done with this work as a basis;

- **Do the same simulation with another turbulence model.** It is interesting to see how much influence the turbulence model has on the results. Ideally, we would like the turbulence model to model the turbulence perfectly. This is very often not the case. One model that work perfectly for one case could give errors for another. It is thus interesting to compare two different turbulence models for one case.
- **Different arrangements.** Instead of the cylinders being completely in line with each other, they could be arranged in a staggered configuration. That would have the same effect as the flow coming in with an angle to the x-axis of the present arrangement. It would be interesting to see the what different disturbances that would occur.
- **New spacing.** One could also do the same simulation with another spacing. A smaller spacing would be most relative to further work since one probably would capture other flow pictures. Spacings close to the critical spacing is relevant for further work, since very complex flows occur here, like bistable flow.
- **Different cylinder diameters.** In stead of two equal diameter cylinders, one cylinder could be of a different size, like it often is in reality. The cylinders would then see very different Reynolds numbers, which is interesting to see the effect of.
- **VIV suppressions on one or both cylinders.** To avoid the chaotic incoming flow onto the downstream cylinder and thus large forces, simulations with VIV suppression can be done. This is already a hot topic and some simulations has been carried out.
- **Allowing the cylinders to move.** In this work the cylinders have been restrained from movement to simplify the simulations. In reality the cylinders would vibrate due to the vortex separation and impingement. A simulation with a coupled CFD and finite element analysis (FEA) solvers could in the future be implemented to see the fluid effect on the construction and the response of the structure which again has an influence on the fluid behaviour.

List of Figures

2.1	Boundary layer aspects on a circular cylinder. Figure taken from Pettersen (2007).	9
2.2	Pressure distributions for real fluid and potential fluid plotted over the cylinder surface. Results for real fluid is taken from simulations done in the master project, fall 2014.	11
2.3	Velocity profiles at 3 different locations along the cylinder surface for $Re=100$	11
2.4	Plot of magnitude of vorticity for Reynolds number 100 that shows vortex shedding from a single cylinder. Figures are taken from master project fall 2014.	13
2.5	Regimes of flow around a circular cylinder in a steady current. Figure taken from Sumer and Fredsøe (1997).	15
2.6	Regions of interference around a circular cylinder. Figure taken from Zdravkovich (2003).	16
2.7	Critical spacing between two tandem cylinders and vortex formation length for a single cylinder as a function of Reynolds number. Figure taken from Ljungkrona and Sundén (1993).	17
2.8	Classification of flow patterns for different spacings and Reynolds numbers. Figure taken from Igarashi (1981).	18
2.9	Different flow patterns for tandem cylinders. Figure taken from Igarashi (1981).	18
2.10	Pressure distribution around tandem cylinders. Figures taken from Igarashi (1981).	21
2.11	Pressure fluctuations around tandem cylinders. Figures taken from Igarashi (1981).	22
2.12	Strouhal number data for two tandem circular cylinders in cross-flow as a function of the spacing: ∇ , $Re = 1.2 \cdot 10^3$ (Xu and Zhou, 2004); \boxtimes , $Re = 2.9 \cdot 10^3$ (Xu and Zhou, 2004); \circ , $Re = 7 \cdot 10^3$ (Xu and Zhou, 2004); \blacksquare , $Re = 4.2 \cdot 10^4$ (Xu and Zhou, 2004); solid line, $Re = 2.2 \cdot 10^4$ (Igarashi, 1981). Figure taken from Xu and Zhou (2004).	23
2.13	Correlation length for a circular cylinder with respect to Reynolds number. Figure taken from Greco (2013).	24
3.1	Neighbour cells with parameters used in the finite volume method. Figure taken from OpenFOAM Programmer's guide, (Foundation, 2013)	29
4.1	(a): 2D slice of the mesh in the x-y-plane showing blocks and element refinement. (b): close-up showing mesh details in the O-grid around the cylinders.	37
4.2	2D slice of computational domain showing parameters and boundary conditions	38

4.3	Plots of velocity profiles in the boundary layer for different radial locations together with the grid points. Details of the inner part of the velocity profiles are given in the corresponding right figures.	40
5.1	Instantaneous vorticity distribution at the mid-span of the cylinders visualized by the Q-criterion. a) vortex A is approaching the downstream cylinder, b) vortex A impinges the downstream cylinder and vortex B is created, c) vortex A is broken up and merges with vortex B	47
5.2	Normalized time-, and space averaged u-velocity profile in the wake behind the cylinders along the x-axis, plotted together with the normalized time-, and space averaged u-velocity profile of a single cylinder, single cylinder results from Prsic et al. (2014)	48
5.3	Normalized time-, and space averaged u-velocity profile in the wake behind the cylinders along the y-axis	49
5.4	Snapshot of the mean velocity taken at the mid span of the cylinders. Vertical lines are drawn where sampling for y cross-section is done	49
5.5	Mean pressure distribution over the cylinder surface. top: upstream cylinder, bottom: downstream cylinder. Blue line: current work, •: Ljungkrona et al. (1991), $Re = 12 \cdot 10^3$ $S/D = 4$, dashed line: Kitagawa and Ohta (2008) $Re = 2.2 \cdot 10^4$ $S/D = 4$, solid line: Prsic et al. (2014) $Re = 1.31 \cdot 10^4$ Single cylinder	50
5.6	Convergence of mean pressure coefficient distribution for upstream and downstream cylinder.	52
5.7	Distribution of RMS pressure fluctuation around two tandem cylinder surfaces. Figure based on Igarashi (1981). Blue line: current work, dotted line in (a): single cylinder, ★ or ☆: $S/D = 3.82$	53
5.8	SurfaceLIC streamlines of U on downstream cylinder at $z = 2$ with points marked in yellow at $\theta = 110$ and red at $\theta = 150$	54
5.9	History of lift and drag coefficients for upstream and downstream cylinder. Top picture: lift coefficient, bottom picture: drag coefficient. Dashed line: upstream cylinder, solid line: downstream cylinder.	56
5.10	Lift coefficient time series of 1 vortex shedding period. Dashed line: upstream cylinder, solid line: downstream cylinder.	57
5.11	Probe locations marked in the computational domain with coloring of velocity U	58
5.12	Strouhal frequency spectra for probes behind upstream and downstream cylinder	59
5.13	Surface streamlines for the instantaneous velocity U_c at the cylinder surfaces	60
5.14	Surface streamlines for the mean velocity U_c at the cylinder surfaces	60
5.15	Separation lines of the upstream and downstream cylinder for U and U mean	61
A.1	Mean pressure distribution over the cylinder surface. top: upstream cylinder, bottom: downstream cylinder.	II
A.2	Iso-surface for λ_2 and Q of value 10 taken from simulations with $Re = 13100$	III
A.3	Iso-surface for λ_2 and Q of value 29 taken from simulations with $Re = 13100$	IV
A.4	Instantaneous vorticity magnitude=10 iso-surface from simulations with $Re = 13100$	V
A.5	Drag- and lift coefficient time histories for the coarse mesh	VI

List of Tables

- 4.1 Overview of boundary conditions for different patches 39
- 4.2 Results comparison of lift and drag coefficient of fine and coarse mesh 41

- 5.1 Details of simulation 45
- 5.2 Mean drag and lift RMS for different cases 58

Bibliography

- Abrahamsen-Prsic, Mia; Ong, M. C. P. B. M. D. (2015). Les of flow around tandem cylinders close to a horizontal wall. accepted for publishing in international journal of offshore and polar engineering ijope.
- Afgan, I., Kahil, Y., Benhamadouche, S., and Sagaut, P. (2011). Large eddy simulation of the flow around single and two side-by-side cylinders at subcritical reynolds numbers. *Physics of Fluids (1994-present)*, 23(7):075101.
- Alam, M. M. (2014). The aerodynamics of a cylinder submerged in the wake of another. *Journal of Fluids and Structures*, 51:393–400.
- Alam, M. M., Moriya, M., Takai, K., and Sakamoto, H. (2003). Fluctuating fluid forces acting on two circular cylinders in a tandem arrangement at a subcritical reynolds number. *Journal of Wind Engineering and Industrial Aerodynamics*, 91(1):139–154.
- Assi, G. R. and Bearman, P. W. Viv and wiv suppression with parallel control plates on a pair of circular cylinders in tandem. In *ASME 2009 28th International Conference on Ocean, Offshore and Arctic Engineering*, pages 263–268. American Society of Mechanical Engineers.
- Bearman, P. W. (1984). Vortex shedding from oscillating bluff bodies. *Annual Review of Fluid Mechanics*, 16:195–222.
- Berger, E. and Wille, R. (1972). Periodic flow phenomena. *Annual Review of Fluid Mechanics*, 4:313–340.
- Biermann, D. and Herrnstein Jr, W. H. (1933). The interference between struts in various combinations. Report, DTIC Document.
- Breuer, M. (1998). Numerical and modeling influences on large eddy simulations for the flow past a circular cylinder. *International Journal of Heat and Fluid Flow*, 19(5):512–521.
- Cengel, Y. A. and Cimbala, J. M. (2010). *Fluid Mechanics - Fundamentals and Applications*. McGraw-Hill, 2 edition.
- Eça, L., Vaz, G., Rosetti, G., and Pereira, F. On the numerical prediction of the flow around smooth circular cylinders. In *ASME 2014 33rd International Conference on Ocean, Offshore and Arctic Engineering*, pages V002T08A013–V002T08A013. American Society of Mechanical Engineers.
- Eymard, R., Herbin, and Gallouët, T. (2010). Finite volume method. *Scholarpedia*, 5.
- Faltinsen, O. M. (1990). *Sea Loads on Ships and Offshore Structures*. Cambridge ocean technology series. Cambridge university press, Cambridge.

Ferziger, J. H. and Peric, M. (2002). *Computational Methods for Fluid Dynamics*. Springer, 3 edition.

Foundation, O. (2013). Openfoam programmer's guide version 2.2.0.

Gabbai, R. D. and Benaroya, H. (2005). An overview of modeling and experiments of vortex-induced vibration of circular cylinders. *Journal of Sound and Vibration*, 282(3–5):575–616. overview of experiments done and numerical models.

Greco, M. (2013). Correlation length of vortex shedding, lecture 10 notes, [powerpoint]. retrieved from <https://ntnu.itslearning.com/contentarea/contentarea.aspx?locationid=54163&locationtype>

Hori, E. (1959). Experiments on flow around a pair of parallel circular cylinders. *Proc. 9th Japan Nat. Congress Appl. Mech.*, pages 231–4.

Igarashi, T. (1981). Characteristics of the flow around two circular cylinders arranged in tandem: 1st report. *Bulletin of JSME*, 24(188):323–331.

Jeong, J. and Hussain, F. (1995). On the identification of a vortex. *Journal of fluid mechanics*, 285:69–94.

Kitagawa, T. and Ohta, H. (2008). Numerical investigation on flow around circular cylinders in tandem arrangement at a subcritical reynolds number. *Journal of Fluids and Structures*, 24(5):680–699.

Lin, J.-C., Yang, Y., and Rockwell, D. (2002). Flow past two cylinders in tandem: instantaneous and averaged flow structure. *Journal of Fluids and Structures*, 16(8):1059–1071.

Ljungkrona, L., Norberg, C., and Sundén, B. (1991). Free-stream turbulence and tube spacing effects on surface pressure fluctuations for two tubes in an in-line arrangement. *Journal of Fluids and Structures*, 5(6):701–727.

Ljungkrona, L. and Sundén, B. (1993). Flow visualization and surface pressure measurement on two tubes in an inline arrangement. *Experimental thermal and fluid science*, 6(1):15–27.

Lysenko, D. A., Ertesvåg, I. S., and Rian, K. E. (2012). Large-eddy simulation of the flow over a circular cylinder at reynolds number 3900 using the openfoam toolbox. *Flow, turbulence and combustion*, 89(4):491–518.

Meneghini, J., Saltara, F., Siqueira, C., and Ferrari, J. (2001). Numerical simulation of flow interference between two circular cylinders in tandem and side-by-side arrangements. *Journal of fluids and structures*, 15(2):327–350.

Organisation, P. (2015). Paraview/line integral convolution.

Pannell, J., Griffiths, E., and Coales, J. (1915). Experiments on the interference between pairs of aeroplane wires of circular and lenticular cross section. *British Advisory Committee for Aeronautics, Reports and memoranda*, (208):1915–1916.

Papaioannou, G. V., Yue, D. K., Triantafyllou, M. S., and Karniadakis, G. E. (2006). Three-dimensionality effects in flow around two tandem cylinders. *Journal of Fluid Mechanics*, 558:387–413.

Pettersen, B. (2007). *Marin Teknisk 3 - Hydrodynamikk*. NTNU, Trondheim, Norway.

- Prandtl, L. (1904). Über flüssigkeitsbewegung bei sehr kleiner reibung. *Intern. Math. Kongr., Heidelberg*, 3:484–491.
- Prsic, M. A., Ong, M. C., Pettersen, B., and Myrhaug, D. (2014). Large eddy simulations of flow around a smooth circular cylinder in a uniform current in the subcritical flow regime. *Ocean Engineering*, 77:61–73.
- Sainte-Rose, B., Allain, O., Leca, C., and Dervieux, A. A study of les models for the simulation of a turbulent flow around supercritical tandem cylinders. In *ASME 2014 33rd International Conference on Ocean, Offshore and Arctic Engineering*, pages V002T08A058–V002T08A058. American Society of Mechanical Engineers.
- Sarpkaya, T. (2004). A critical review of the intrinsic nature of vortex-induced vibrations. *Journal of Fluids and Structures*, 19(4):389–447.
- Schlichting, H. and Gersten, K. (2000). *Boundary Layer Theory*. Springer-Verlag, Germany, 8 edition.
- Springer, M., Jaiman, R. K., Cosgrove, S., and Constantinides, Y. Numerical modeling of vortex-induced vibrations of two flexible risers. In *ASME 2009 28th International Conference on Ocean, Offshore and Arctic Engineering*, pages 749–756. American Society of Mechanical Engineers.
- Sumer, B. M. and Fredsøe, J. (1997). *Hydrodynamics around circular cylinders*, volume 12. World Scientific Publishing Co. Pte. Ltd.
- Sumner, D. (2010). Two circular cylinders in cross-flow: A review. *Journal of Fluids and Structures*, 26(6):849–899.
- Uzun, A. and Hussaini, M. Y. (2012). An application of delayed detached eddy simulation to tandem cylinder flow field prediction. *Computers & Fluids*, 60:71–85.
- Versteeg, H. K. and Malalasekera, W. (1995). *An introduction to computational fluid dynamics: the finite volume method*. Longman Group Ltd, England.
- Wu, J., Welch, L. W., Welsh, M. C., Sheridan, J., and Walker, G. J. (1994). Spanwise wake structures of a circular cylinder and two circular cylinders in tandem. *Experimental Thermal and Fluid Science*, 9(3):299–308.
- Xu, G. and Zhou, Y. (2004). Strouhal numbers in the wake of two inline cylinders. *Experiments in Fluids*, 37(2):248–256.
- Zdravkovich, M. and Pridden, D. (1977). Interference between two circular cylinders; series of unexpected discontinuities. *Journal of wind engineering and industrial aerodynamics*, 2(3):255–270.
- Zdravkovich, M. M. (1997). *Flow around circular cylinders: fundamentals*, volume 1. Oxford University Press, United States.
- Zdravkovich, M. M. (2003). *Flow around circular cylinders: Applications*, volume 2. Oxford university press, New York.
- Zdravkovich, M. M. and Stanhope, D. (1972). Flow pattern in the gap between two cylinders in tandem. *University of Salford Internal Report*.

Appendix A

Visualization and results

Mean pressure coefficient for upstream and downstream cylinder:

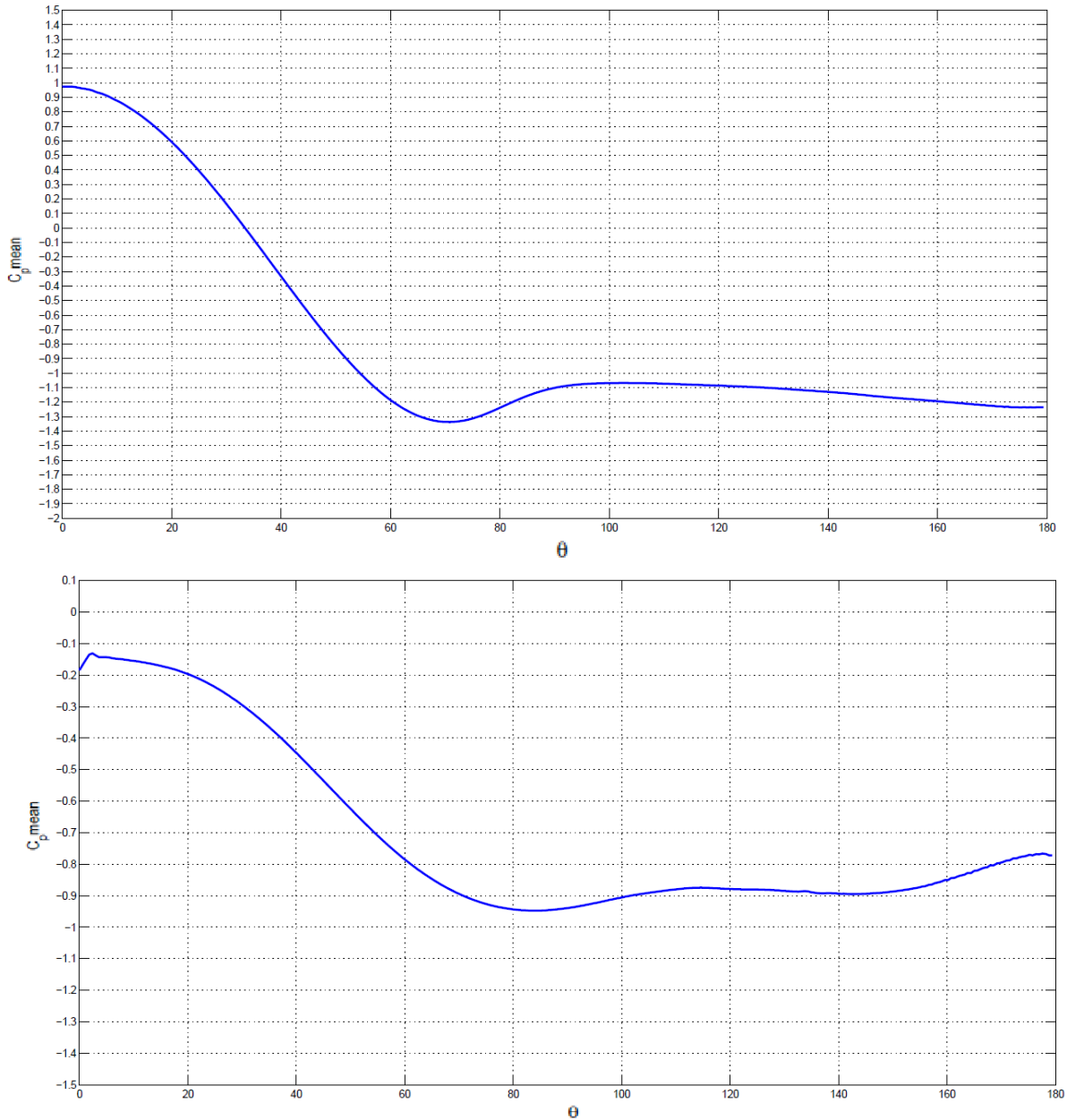
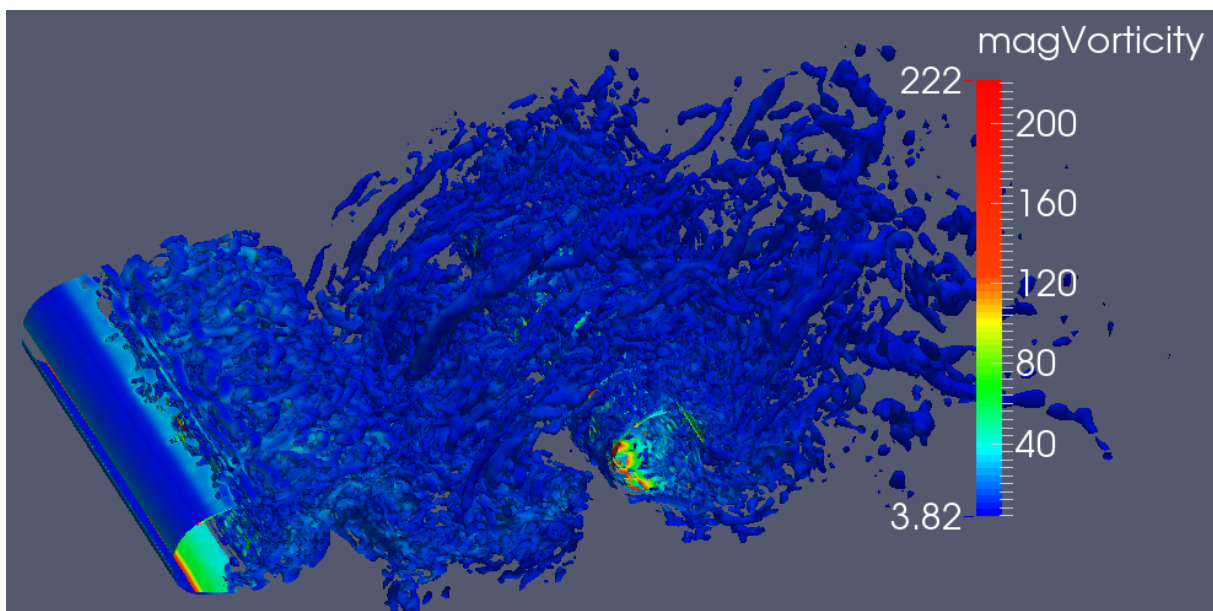
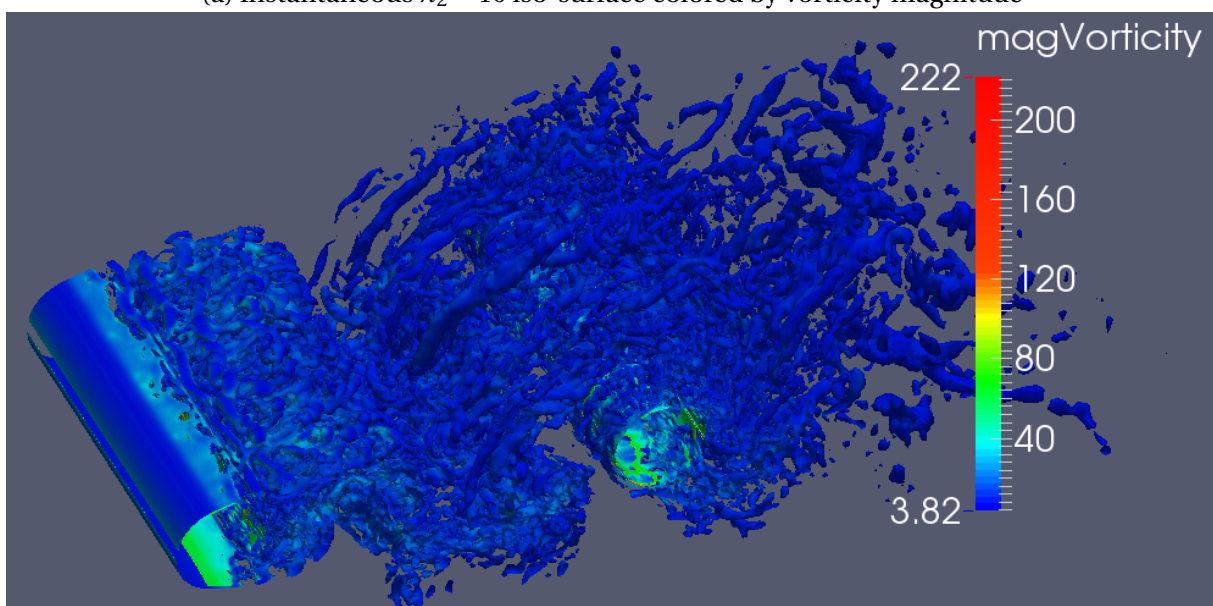


Figure A.1: Mean pressure distribution over the cylinder surface. top: upstream cylinder, bottom: downstream cylinder.

Iso-surfaces for the Q-, and λ_2 -criterion for different values:

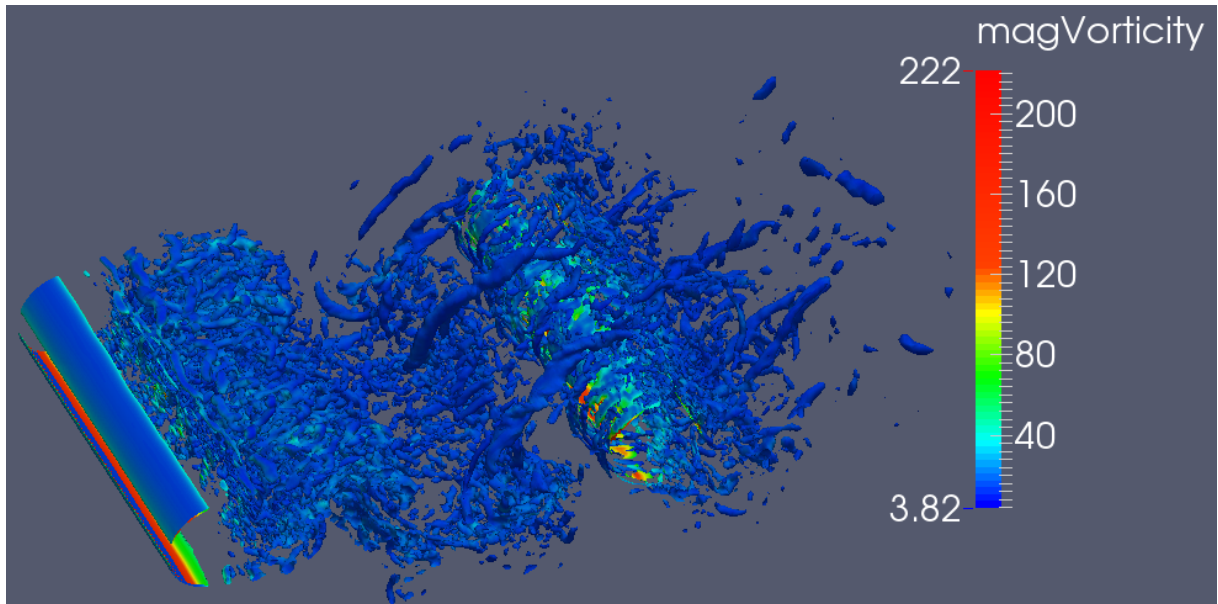


(a) Instantaneous $\lambda_2 = 10$ iso-surface colored by vorticity magnitude

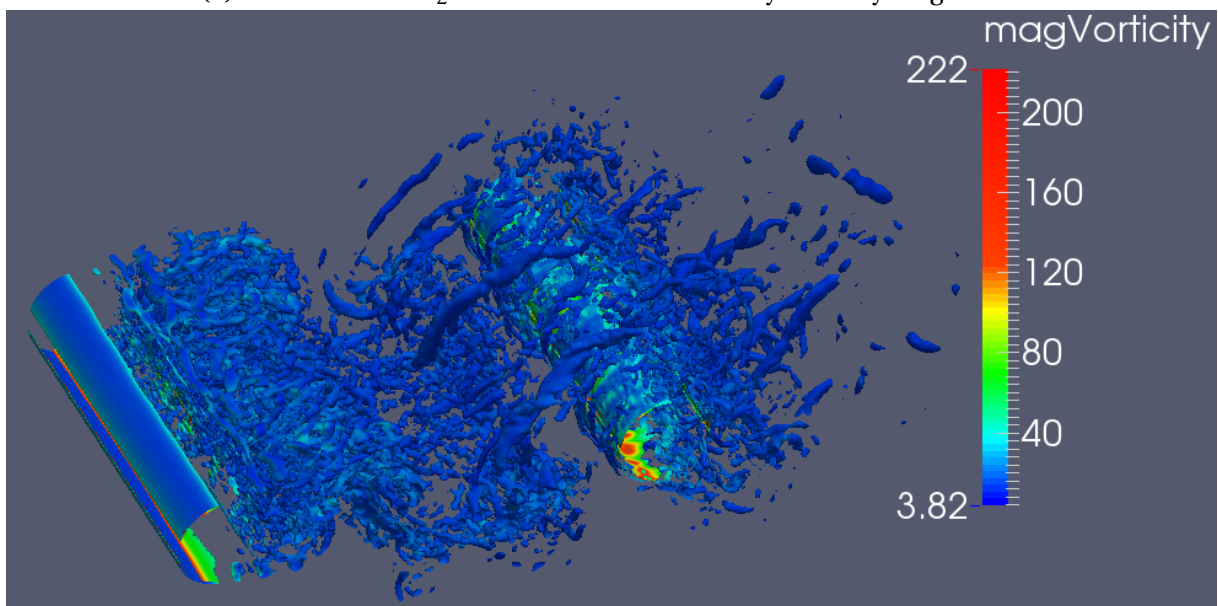


(b) Instantaneous $Q = 10$ iso-surface colored by vorticity magnitude

Figure A.2: Iso-surface for λ_2 and Q of value 10 taken from simulations with $Re = 13100$.



(a) Instantaneous $\lambda_2 = 29$ iso-surface colored by vorticity magnitude



(b) Instantaneous $Q = 29$ iso-surface colored by vorticity magnitude

Figure A.3: Iso-surface for λ_2 and Q of value 29 taken from simulations with $Re = 13100$.

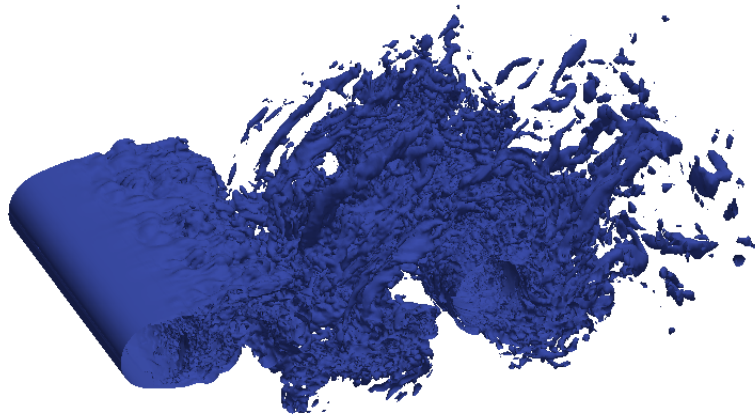
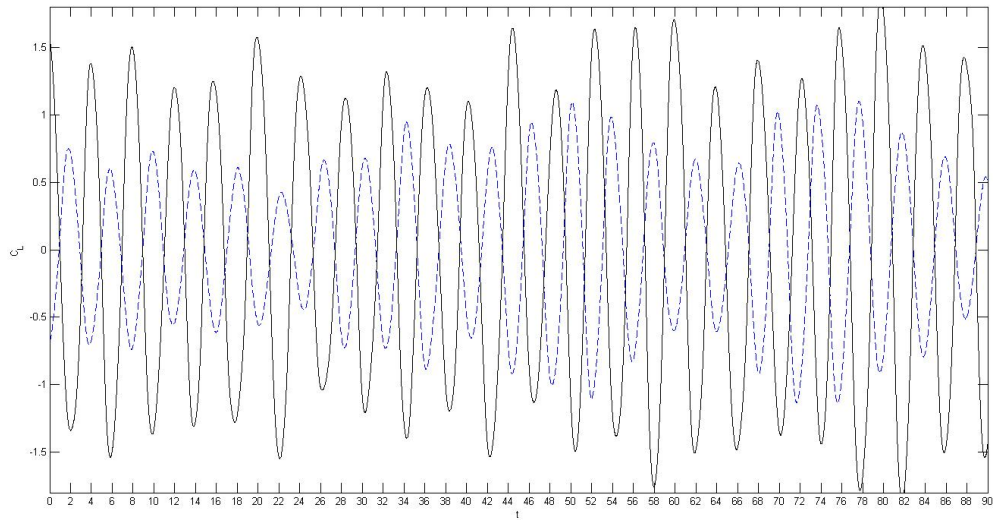


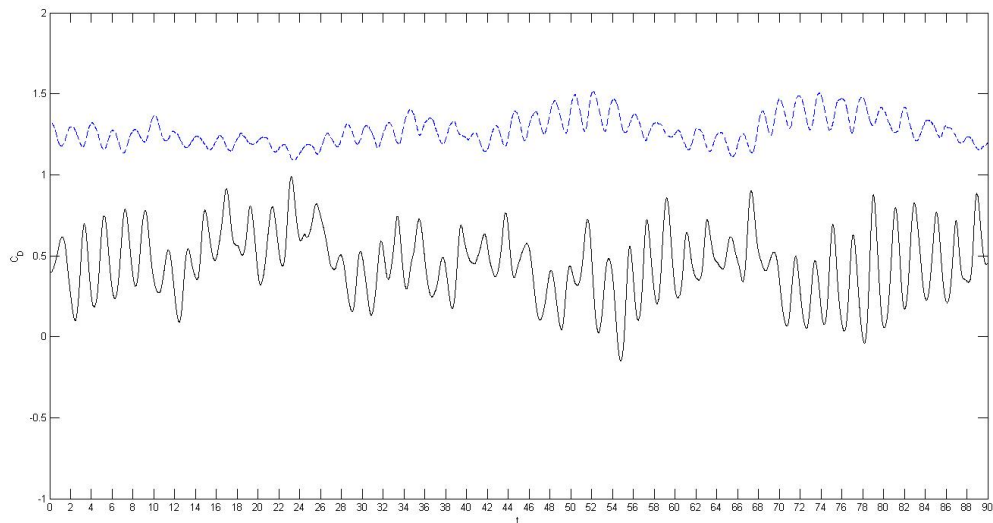
Figure A.4: Instantaneous vorticity magnitude=10 iso-surface from simulations with $Re = 13100$.

A.1 Drag- and lift time history of coarse mesh

Time history of the drag- and lift coefficient of the coarse mesh.



(a) Time history of the lift coefficient



(b) Time history of the drag coefficient

Figure A.5: Drag- and lift coefficient time histories for the coarse mesh


```

37 writeControl    timeStep;
38
39 writeInterval   1;
40
41 purgeWrite      0;
42
43 writeFormat     ascii;
44
45 writePrecision  6;
46
47 writeCompression uncompressed;
48
49 timeFormat      general;
50
51 timePrecision   6;
52
53 runTimeModifiable no;
54
55 functions
56 {
57
58     /*forces1
59     {
60     type          forces;
61     functionObjectLibs ("libforces.so");
62     patches       (cyl1);
63     pName         p;
64     UName         U;
65     rhoName       rhoInf;
66     rhoInf        1;
67     log           false;
68     CofR          (0 0 0);
69     outputControl timeStep;
70     outputInterval 1;
71     }
72
73     forceCoeffs1
74     {
75     type          forceCoeffs;          //coeffs Cd, Cl
76     functionObjectLibs ("libforces.so");
77     patches       (cyl1);
78     pName         p;
79     UName         U;
80     rhoName       rhoInf;
81     rhoInf        1;
82     log           false;
83     CofR          (0 0 0);
84     liftDir       (0 1 0);
85     dragDir       (1 0 0);              //direction of drag - x
86     pitchAxis     (0 0 0);              //pitch axis 0 ???
87     magUInf       1.31;
88     lRef          4;                    //referent lenght (1 or for 3D calc change)
89     Aref          4;                    //referent projection of impact area (D*1)
90     outputControl timeStep;
91     outputInterval 1;
92     }
93
94

```



```

95     forces2
96     {
97     type          forces;
98     functionObjectLibs ("libforces.so");
99     patches       (cyl2);
100    pName          p;
101    UName          U;
102    rhoName        rhoInf;
103    rhoInf         1;
104    log            false;
105    CofR           (5 0 0);
106    outputControl   timeStep;
107    outputInterval 1;
108    }
109
110    forceCoeffs2
111    {
112    type          forceCoeffs;          //coeffs Cd, Cl
113    functionObjectLibs ("libforces.so");
114    patches       (cyl2);
115    pName          p;
116    UName          U;
117    rhoName        rhoInf;
118    rhoInf         1;
119    log            false;
120    CofR           (5 0 0);
121    liftDir        (0 1 0);
122    dragDir         (1 0 0);          //direction of drag - x
123    pitchAxis       (0 0 0);          //pitch axis 0 ???
124    magUInf         1.31;
125    lRef            4;                //referent lenght (1 or for 3D calc change)
126    Aref            4;                //referent projection of impact area (D*1)
127    outputControl   timeStep;
128    outputInterval 1;
129    }
130
131
132
133
134
135
136
137    probes
138    {
139        type          probes;
140        functionObjectLibs ("libsampling.so");
141        enabled        true;
142        outputControl   timeStep;
143        outputInterval 1;
144        probeLocations
145        (
146        (1 0.3 2)
147        (-8 0 2)
148        (4.6 0.35 2)
149        (8 0.3 2)
150        );
151
152        fields

```

```

153     (
154     p U
155     );
156 }
157 */
158 fieldAverage1
159 {
160     type                fieldAverage;
161     functionObjectLibs ("libfieldFunctionObjects.so");
162     enabled              true;
163     outputControl        outputTime;
164     fields
165     (
166         U
167         {
168             mean          on;
169             prime2Mean    on;
170             base           time;
171         }
172
173         p
174         {
175             mean          on;
176             prime2Mean    on;
177             base           time;
178         }
179     );
180 }
181 #include "wallBoundedStreamLines"
182
183 }
184
185
186 // ***** //

```

B.2 wallBoundedStreamLines

```

1 /*-----*-- C++ --*-----*\
2 | ===== |
3 | \\      / F i e l d | OpenFOAM: The Open Source CFD Toolbox |
4 | \\      / O p e r a t i o n | Version: 2.3.0 |
5 | \\      / A n d | Web: www.OpenFOAM.org |
6 |  \\//      M a n i p u l a t i o n | |
7 \*-----*//
8
9 // Interpolate U to create near-wall UNear
10 near
11 {
12     // Where to load it from
13     functionObjectLibs ("libfieldFunctionObjects.so");
14
15     type nearWallFields;
16
17     // Output every
18     outputControl    outputTime;

```

```

19
20 // Fields to be sampled. Per field original name and mapped field to
21 // create.
22 // Note: fields only get updated when writing!
23 fields
24 (
25     (U UNear)
26     (UMean UMeanNear)
27     (p pNear)
28     (pMean pMeanNear)
29 );
30
31 // Patches/groups to sample (regular expressions)
32 patches (cyl1 cyl2);
33
34 // Distance to sample
35 distance 0.005;
36 }
37
38 // Use UNear to track along wall
39 wallBoundedStreamLines
40 {
41     // Where to load it from (if not already in solver)
42     functionObjectLibs ("libfieldFunctionObjects.so");
43     type                wallBoundedStreamLine;
44
45     // Output every
46     outputControl      outputTime;
47
48     setFormat          vtk; //gnuplot; //xmgr; //raw; //jplot;
49
50     // Velocity field to use for tracking.
51     UName UNear;
52
53     // Interpolation method. Default is cellPoint. See sampleDict.
54     //interpolationScheme pointMVC;
55
56     // Tracked forwards (+U) or backwards (-U)
57     trackForward      true;
58
59     interpolationScheme cellPoint;
60
61     // Names of fields to sample. Should contain above velocity field!
62     fields (p U UNear);
63
64     // Steps particles can travel before being removed
65     lifeTime          100;
66
67     // Cloud name to use
68     cloudName          wallBoundedParticleTracks;
69
70     // Seeding method. See the sampleSets in sampleDict.
71     seedSampleSet      patchSeed; //cloud;//triSurfaceMeshPointSet;
72
73     uniformCoeffs
74     {
75         type            uniform;
76         axis             x; //distance;

```

```

77
78     start      (0.0035 0.0999 0.0001);
79     end        (0.0035 0.0999 0.0099);
80     nPoints    20;
81 }
82 cloudCoeffs
83 {
84     type        cloud;
85     axis        x; //distance;
86     points      ((0.351516548679288 -0.0116085375585099 2));
87 }
88 patchSeedCoeffs
89 {
90     type        patchSeed;
91     patches      (cyl1 cyl2);
92     axis        x; //distance;
93     maxPoints    20000;
94 }
95 }
96
97
98 // ***** //

```

B.3 fvSchemes

```

1 /*-----*-- C++ -*-----*\
2 | ===== | |
3 | \ \ / F i e l d | OpenFOAM: The Open Source CFD Toolbox |
4 | \ \ / O p e r a t i o n | Version: 1.6 |
5 | \ \ / A n d | Web: www.OpenFOAM.org |
6 | \ \ / M a n i p u l a t i o n | |
7 /*-----*--*/
8 FoamFile
9 {
10     version      2.0;
11     format        ascii;
12     class         dictionary;
13     location      "system";
14     object        fvSchemes;
15 }
16 // ***** //
17
18 ddtSchemes
19 {
20     default      CrankNicolson 0.5;
21 }
22
23 gradSchemes
24 {
25     default      Gauss linear;
26     grad(p)      Gauss linear;
27     grad(U)      Gauss linear;
28 }
29
30 divSchemes

```

```

31 {
32     default          none;
33     div(phi,U)       Gauss linear;
34     div(phi,k)       Gauss limitedLinear 1;
35     div(phi,B)       Gauss limitedLinear 1;
36     div(phi,nuTilda) Gauss limitedLinear 1;
37     div(B)           Gauss linear;
38     div((nuEff*dev(T(grad(U)))) Gauss linear;
39 }
40
41 laplacianSchemes
42 {
43     default          none;
44     laplacian(nuEff,U) Gauss linear corrected;
45     laplacian((1|A(U)),p) Gauss linear corrected;
46     laplacian(DkEff,k) Gauss linear corrected;
47     laplacian(DBEff,B) Gauss linear corrected;
48     laplacian(DnuTildaEff,nuTilda) Gauss linear corrected;
49 }
50
51 interpolationSchemes
52 {
53     default          linear;
54     interpolate(U)   linear;
55 }
56
57 snGradSchemes
58 {
59     default          corrected;
60 }
61
62 fluxRequired
63 {
64     default          no;
65     p                 ;
66 }
67
68
69 // ***** //

```

B.4 fvSolution

```

1 /*-----*-- C++ -*-----*\
2 | ===== |
3 | \\      / F ield      | OpenFOAM: The Open Source CFD Toolbox|
4 | \\      / O peration  | Version: 1.6 |
5 | \\      / A nd        | Web:      www.OpenFOAM.org |
6 | \\      / M anipulation | |
7 \*-----*--*/
8 FoamFile
9 {
10     version      2.0;
11     format       ascii;
12     class        dictionary;
13     location     "system";

```

```
14     object      fvSolution;
15 }
16 // * * * * *
17
18 solvers
19 {
20     p
21     {
22         solver      PCG;
23         preconditioner DIC;
24         tolerance    1e-06;
25         relTol       0.05;
26     }
27
28     pFinal
29     {
30         solver      PCG;
31         preconditioner DIC;
32         tolerance    1e-06;
33         relTol       0;
34     }
35
36     U
37     {
38         solver      PBiCG;
39         preconditioner DILU;
40         tolerance    1e-05;
41         relTol       0;
42     }
43
44     k
45     {
46         solver      PBiCG;
47         preconditioner DILU;
48         tolerance    1e-05;
49         relTol       0;
50     }
51
52     B
53     {
54         solver      PBiCG;
55         preconditioner DILU;
56         tolerance    1e-05;
57         relTol       0;
58     }
59
60     nuTilda
61     {
62         solver      PBiCG;
63         preconditioner DILU;
64         tolerance    1e-05;
65         relTol       0;
66     }
67 }
68
69 PISO
70 {
71     nCorrectors      2;
```

```

72     nNonOrthogonalCorrectors 0;
73 }
74
75
76 // *****//

```

B.5 LESProperties

```

1 /*-----* C++ *-----*\
2 | ===== |
3 | \\ / F i e l d | OpenFOAM: The Open Source CFD Toolbox |
4 | \\ / O p e r a t i o n | Version: 1.6 |
5 | \\ / A n d | Web: www.OpenFOAM.org |
6 | \\ / M a n i p u l a t i o n |
7 /*-----*\
8 FoamFile
9 {
10     version      2.0;
11     format       ascii;
12     class        dictionary;
13     location     "constant";
14     object       LESProperties;
15 }
16 // *****//
17
18 LESModel      Smagorinsky;
19
20 delta         cubeRootVol;
21
22 printCoeffs  on;
23
24 cubeRootVolCoeffs
25 {
26     deltaCoeff      1;
27 }
28
29 PrandtlCoeffs
30 {
31     delta           cubeRootVol;
32     cubeRootVolCoeffs
33     {
34         deltaCoeff      1;
35     }
36
37     smoothCoeffs
38     {
39         delta           cubeRootVol;
40         cubeRootVolCoeffs
41         {
42             deltaCoeff      1;
43         }
44
45         maxDeltaRatio  1.1;
46     }
47

```

```
48     Cdelta          0.158;
49 }
50
51 vanDriestCoeffs
52 {
53     delta            cubeRootVol;
54     cubeRootVolCoeffs
55     {
56         deltaCoeff    1;
57     }
58
59     smoothCoeffs
60     {
61         delta            cubeRootVol;
62         cubeRootVolCoeffs
63         {
64             deltaCoeff    1;
65         }
66
67         maxDeltaRatio    1.1;
68     }
69
70     Aplus            26;
71     Cdelta          0.158;
72 }
73
74 smoothCoeffs
75 {
76     delta            cubeRootVol;
77     cubeRootVolCoeffs
78     {
79         deltaCoeff    1;
80     }
81
82     maxDeltaRatio    1.1;
83 }
84
85
86 // ***** //
```